Strojniški vestnik
Journal of Mechanical Engineering

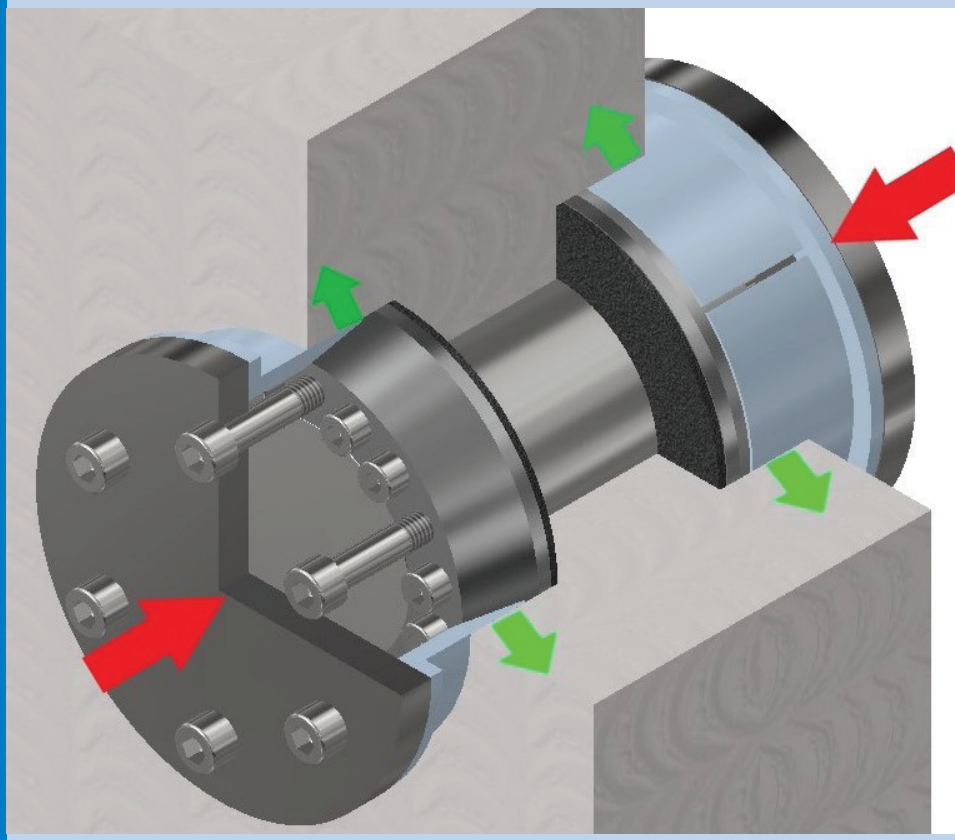

no. 12
year 2021
volume 67

Strojniški vestnik – Journal of Mechanical Engineering (SV-JME)

Aim and Scope

The international journal publishes original and (mini)review articles covering the concepts of materials science, mechanics, kinematics, thermodynamics, energy and environment, mechatronics and robotics, fluid mechanics, tribology, cybernetics, industrial engineering and structural analysis.

The journal follows new trends and progress proven practice in the mechanical engineering and also in the closely related sciences as are electrical, civil and process engineering, medicine, microbiology, ecology, agriculture, transport systems, aviation, and others, thus creating a unique forum for interdisciplinary or multidisciplinary dialogue.

The international conferences selected papers are welcome for publishing as a special issue of SV-JME with invited co-editor(s).

Editorial Office

University of Ljubljana, Faculty of Mechanical Engineering
SV-JME, Aškerčeva 6, SI-1000 Ljubljana, Slovenia
Phone: 386 (0)1 4771 137
Fax: 386 (0)1 2518 567
info@sv-jme.eu, http://www.sv-jme.eu

Print: Demat d.o.o., printed in 250 copies

Founders and Publishers

University of Ljubljana, Faculty of Mechanical Engineering, Slovenia
University of Maribor, Faculty of Mechanical Engineering, Slovenia
Association of Mechanical Engineers of Slovenia
Chamber of Commerce and Industry of Slovenia, Metal Processing Industry Association

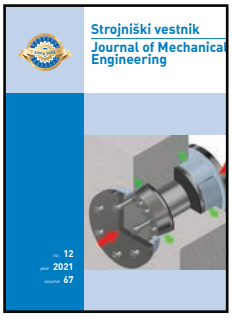

Cover:
The image shows an invention of Bondura Technology that combines a preloaded bolt and an expanding shear pin functionality. The invention is intended to be used in flanged joints or in other situations where it is important to prevent any relative movements between the surfaces, and maintain a high contact pressure over time. The expanding properties ensure a wedge lock between the pin and the support or flange bores, which prevent any unwanted and damaging movements.

Image Courtesy: M.M. Akhtar & Ø. Karlsen
Department of Mechanical and Structural Engineering and Materials Science, University of Stavanger and Bondura Technology AS, Norway

General information

Strojniški vestnik – Journal of Mechanical Engineering is published in 11 issues per year (July and August is a double issue).

Institutional prices include print & online access: institutional subscription price and foreign subscription €100,00 (the price of a single issue is €10,00); general public subscription and student subscription €50,00 (the price of a single issue is €5,00). Prices are exclusive of tax. Delivery is included in the price. The recipient is responsible for paying any import duties or taxes. Legal title passes to the customer on dispatch by our distributor. Single issues from current and recent volumes are available at the current single-issue price. To order the journal, please complete the form on our website. For submissions, subscriptions and all other information please visit: *http://www.sv-jme.eu*.

You can advertise on the inner and outer side of the back cover of the journal. The authors of the published papers are invited to send photos or pictures with short explanation for cover content.

We would like to thank the reviewers who have taken part in the peer-review process.

ISSN 0039-2480, ISSN 2536-2948 (online)

The journal is subsidized by Slovenian Research Agency.

Strojniški vestnik - Journal of Mechanical Engineering is available on *https://www.sv-jme.eu*.

Contents

Strojniški vestnik - Journal of Mechanical Engineering
volume 67, (2021), number 12
Ljubljana, December 2021
ISSN 0039-2480

Published monthly

Papers

Strojniški vestnik - Journal of Mechanical Engineering 67(2021)12, 625-634

DOI:10.5545/sv-jme.2021.7306 Original Scientific Paper
Received for review: 2021-06-30
Received revised form: 2021-10-11
Accepted for publication: 2021-11-08

Study of Bondura® Expanding PIN System – Combined Axial and Radial Locking System

Muhammad Maaz Akhtar[1] – Øyvind Karlsen[1,2] – Hirpa G. Lemu[1,*]
[1] University of Stavanger, Norway
[2] Bondura Technology AS, Norway

Bolted connections are widely used in parallel plates and flanged joints to axially lock using the preload generated by the tightening torque and to constrain radial movements of the flanges by the surface friction between mating surfaces. The surface friction depends on the micro-asperities of mating surfaces; under the influence of vibrations and other external radial loads, these asperities tend to deform over time, resulting in the failure of the connection. The Bondura expanding pin system presented in this article is an innovative axial and radial locking system, in which the failure of bolted connections due to radial movements is eliminated by relying on the mechanical strength of the pin system along with the surface friction. The present study describes an experimental design to verify the maximum possible preload on the axial-radial pin at different levels of applied torque. The article also provides a realistic comparison of the pin system with standard bolts in terms of handling axial and radial loads. With some alterations in the axial-radial pin system's design, the joint's capability to resist failure improved appreciably compared with the original design and standard bolts with higher preload. As a result, the estimated capability improvement of the joint against the connection failure due to the external radial load by the axial-radial pin is observed to be more than 200 % compared to standard bolts. Considering the pros and cons of both fasteners, i.e., axial-radial pin and standard bolts, a practical solution can be chosen in which both fasteners are used in a connection, and an optimized situation can be developed based on the working conditions.

Keywords: axial locking, expanding pin system, bolt preload, contact asperities, flanged connection, radial locking, shear resistance, shrink fit

Highlights
- *The expanding pin technology that provides an innovative axial-radial locking system is described.*
- *The advantages of the innovative combined radial and axial locking system to eliminate the radial movement of bolted connections in flanges and pipes are studied.*
- *Experimental tests are conducted to verify the maximum possible preload that the axial-radial pin can generate at different applied torques.*
- *The shear capacity of a parallel plate joint using the axial-radial pin is compared with the capability of standard bolts of the same size.*

0 INTRODUCTION

The flange connection is one of the most widely used pipe joints [1]; it involves bolts with nuts under pre-tension or preload. The preload in the bolts is generated by torquing the nuts that force the two flanges towards each other or by hydraulic tensioning of the shank and careful tightening of the nuts and realizing the hydraulic tensioning. This prevents axial movement of the flanges relative to each other, whereas the radial movements are prevented by the contact pressure between the mating flange surfaces under this preload [2] and [3].

Studies [4] show a direct relationship between the strength of the flanged joints and the level of the tightness. The drawback of this conventional practice comes from restricting the radial movements only on the shear resistance of the mating surfaces of flanges. The existence of minor radial movements can lead to total failure of the connection [5]. Further, in pressurized big diameter pipe systems, leakage could occur because there always exist small vibrations in flange connections caused by the exposure to heavy loads and external vibrations caused by the flow of fluid [6]. These vibrations and radial movements reduce the surface friction between the bolt heads, nuts, and flanges by deforming the surfaces' micro-asperities and, eventually, it could cause a reduction in the preload, which could lead to failure of the connection [7]. In the presence of cyclic loading, bolted joints are one of the most exposed parts [8], and the fatigue performance of the joint is mostly governed by existing guidelines or standards, such as Eurocode recommendations [9], that are mostly conservative.

In flange-bolted joints, the thread friction and surface friction at the bearing surface of washers or nuts are influenced by the surface roughness, lubrication conditions, and the number of tightening and loosening events that influence the effectiveness of

*Corr. Author's Address: University of Stavanger, N-4036, Stavanger, Norway, Hirpa.g.lemu@uis.no

the joints to transfer the shear resistance. Furthermore, such connections require precise torquing to provide the necessary preload [10]. The tolerance that is kept between the diameter of the bolt and the bolt hole diameter of the flange for easy installation allows radial movements to occur. Theoretically, such a problem can be avoided by eliminating the tolerance by implementing an interference fit solution, such as press-fit or shrink-fit solutions [11] and [12].

Press-fitted solutions in bolted flange connections are challenging because obtaining a perfect match of all adjacent flange bores is quite difficult and often impossible, considering the combination of their sizes and positions. In addition to the installation difficulties, it would be challenging to retrieve the bolts without damaging the flange structure. In addition, applying press or shrink interference fit may be impossible to increase the contact pressure between the two main flanges due to the high friction contact pressure between the pins and flange bores. Tightening of the nut will possibly not overcome, or only partly overcome, the resistance due to contact pressure between the pin and the flange bore. In contrast, a shrink-fit solution could ease the installation compared to the press-fit, but it would suffer the same issues when it comes to tightening and retrieval [13].

Following this introduction section, this article is divided into five main sections. Section 1 describes the combined axial-radial locking system and the objectives of researching this invention. Then the materials and methods used in the study are presented in Section 2, followed by the experimental setup in Section 3. The results of the experimental work are discussed in Section 4, and finally, the conclusions drawn from the investigation are presented in Section 5.

1 SYSTEM DESCRIPTION AND OBJECTIVES

To address the above-discussed problems with flanged joints, Bondura Technology AS has designed a technical solution for this rather complex problem with its "Expanding PIN System – Combined axial-radial locking system", for which the company has received a Norwegian patent (number 344799). This pin system, which is currently in the design phase, has full potential to prevent connection failure due to the radial movements. This is because this pin system is designed to include the mechanical strength of the pin instead of just depending on the surface friction between mating surfaces of flanges.

For the application of the axial radial pin system, the connecting flanges or plates must be adopted accordingly by increasing the pin bore diameter partly through the flange, as shown in Fig. 1. The increased bore diameters are at the opposite flange faces compared to the mating flange faces. The axial radial pin system is symmetrical as illustrated by the three dimensional (3D) view in Fig. 1, which means the central pin is the centre of the pin system, and the

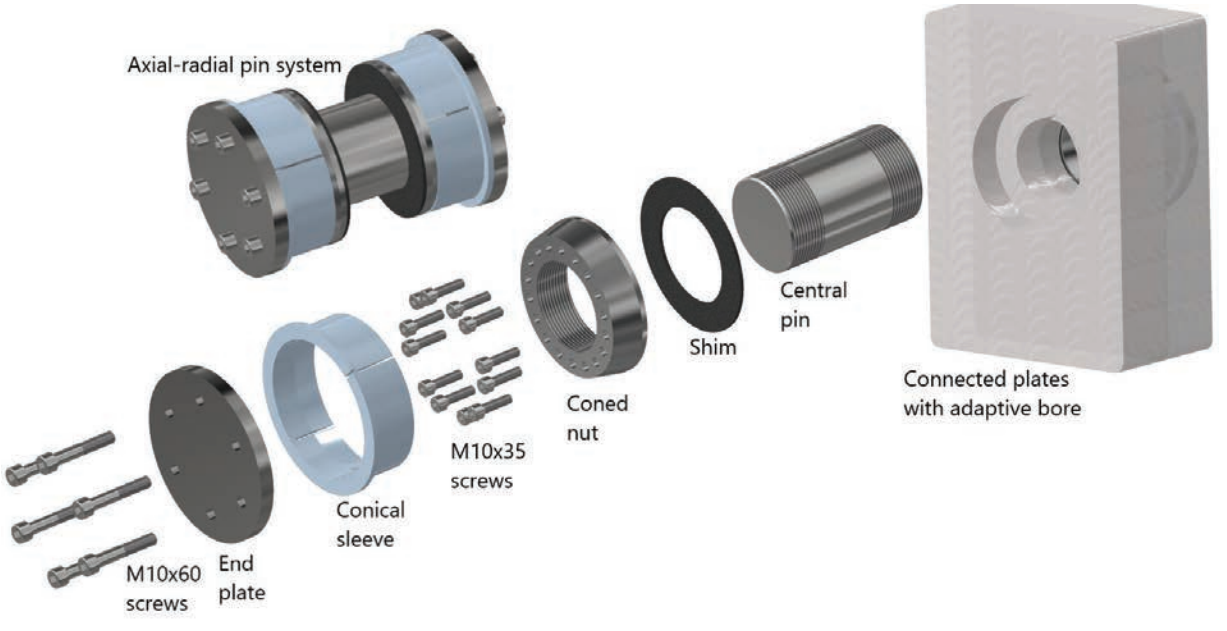

Fig. 1. *Axial-radial pin system with exploded view and adaptive connecting plates*

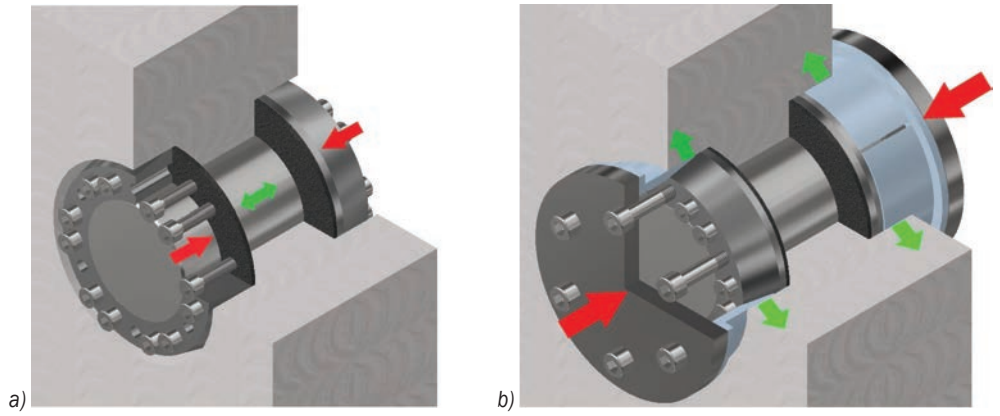

Fig. 2. *Function of screws; a) M10×35, and b) M10×60*

same six components are employed on both sides, as shown by the exploded view from one side.

In assembling, the central pin, which has threads on both ends, goes through the bolt holes of the flanges, and shims are inserted on both sides and placed at the bottom of the increased pin bore. The two coned nuts are then screwed by hand on each side of the central pin until both coned nuts touch shims.

The M10×35 screws are torqued through the coned nuts and create a pushing force on the flange surfaces, as shown by the red arrows in Fig. 2a. In reaction to the pushing force, the central pin, which is screwed by conned nuts on both sides, is tensioned to its final preload, indicated by green arrows in Fig. 2a.

After preloading the pin, the conical sleeves are installed on both sides of the central pin, which function as wedges to eliminate the radial tolerance between the pin system and the flange bore. End plates are used to transfer the force from the tightening of M10×60 screws into the coned nut to the conical sleeves, as illustrated in Fig. 2b.

Fig. 3 illustrates the difference between the design approaches to eliminate the failure of a flange connection by both fastener systems, standard and axial-radial pin systems. For the standard bolt and nut system, the restriction of both the axial and radial movements depends on the bolt's preload. If the preload is not sufficient or reduced over its functional period, the result would be loss of contact pressure, which could lead to the connection's failure.

For the axial-radial pin system, the restriction of the radial movements between the flanges does not entirely depend on the preload in the central pin. The expanded conical sleeve between the pin and flanges transfers the radial load to the central pin; for a failure to occur due to radial movements, the external radial load must have sufficient magnitude to surpass the shear yield strength of the central pin.

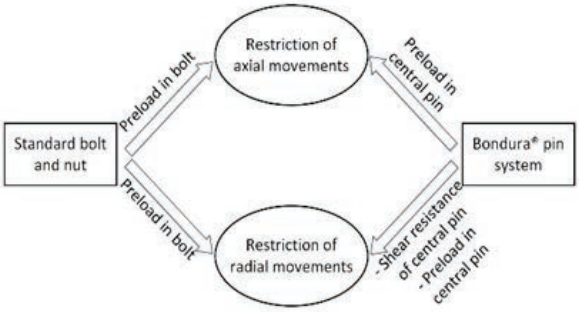

Fig. 3. *Design approaches for axial- radial pin system and standard bolt in terms of restricting axial and radial movements*

The work reported in this article is conducted as a collaboration project between Bondura Technology AS and the University of Stavanger as a part of a master's thesis [14]. As the axial-radial pin system with combined axial and radial locking system is in the testing and verification phase, theoretical, numerical, and experimental analyses are required to finalize and optimize the product. To optimize the product, two main objectives are identified: (1) investigate maximizing the preload in the axial-radial pin system as a function of numbers and sizes of tightening screws and factors that are limiting the maximum preload, and (2) to make a comparative study of axial-radial pin system with the standard conventional bolt system in terms of maximum preload and locking capability against radial and rotational movements.

Therefore, a study on both Ø50 mm and Ø80 mm axial-radial pin systems was conducted. In this regard, the maximum possible preloads for different torque levels were first estimated by using bolted connection theories [2] and [11]. An experimental setup was

designed for both pin systems to verify the calculated results. For the comparative study, two standard bolts, M50 and M80, were selected, and a comparison was made in terms of maximum possible preload and the ability to avoid failure emanating from radial movements. The experimental study is limited to the two sizes of axial-radial pin systems, i.e., Ø50 mm and Ø80 mm, which are provided by the company [15].

2 METHODS AND MATERIALS

Preload in bolted connection is possible by applying torque; to achieve the desired preload, it is important to understand the relationship between torquing level and resulting preload. The common method to define the relationship between maximum applied torque (T) and resulting preload (F_i) is given by the relation,

$$F_i = \frac{T}{Kd}, \tag{1}$$

where K is an experimental factor that is set equal to 0.18 for lubricated surfaces (on bearing surface and on threads) and d is thread diameter of the bolt/screw [2]. To verify the calculated preloads by an axial-radial pin system for different levels of applied torque according to the above equation, an experiment was designed in which different levels of torque are applied on both axial-radial pin systems. The purpose of the experiment was to observe the normal stress in the central pin. Therefore, instead of using a complete flange, a test jig was used, as shown in Fig. 4, which was bolted on the test bench.

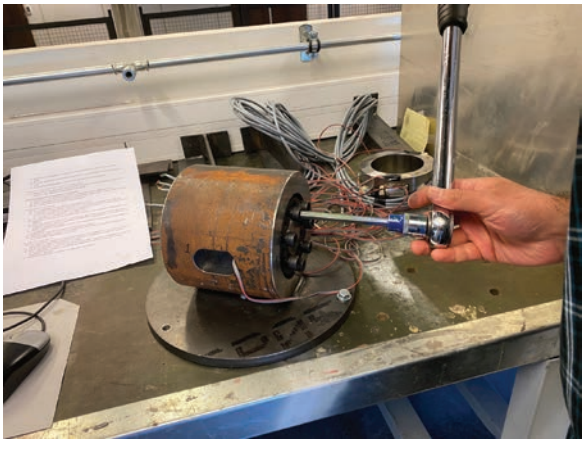

Fig. 4. *Experiment setup and manual application of torque on axial-radial pin system in the test jig*

In this experiment, average normal stress along the central pin's longitudinal axis was measured using two strain gauges of type KLY41 from HBM company [16], which were connected in parallel at an angle of approx. 180° on the pin. The reference temperature for this strain gauge is 23 °C, and the operating range for static analysis was from -70 °C to +200 °C. The strain gauge selected for this experiment has a grid length 3 mm and 200 Ω of grid resistance with a gauge factor of 2. The method employed in this experiment for the application of strain gauges is called the active dummy method [17]. It is a widely implemented method for compensating thermally induced strains. In this experiment, four strain gauges were used on a single pin, two of such strain gauges were applied on the central pin, and the other two were applied as dummy strain gauges on a member, which is made of the same material as of the central pin.

The used data acquisition system (DAQ) module is from HMB company and consists of a measurement electronics gadget known as Spider8 and software called Catman® professional [16]. For the application of controlled load, the torque in this experiment was applied by hand using a torque wrench from USAG company [18], as shown in Fig. 4. This torque wrench works on the turn-of-the-nut method and has an application range of 40 Nm to 200 Nm, which is sufficient for the present experiment because the maximum calculated torque that the M10 screw can sustain is approx. 147 Nm.

In terms of material, the end plate and conical sleeve are made of S355J2 with a minimum ultimate tensile strength of 450 MPa and a minimum yielding strength of 295 MPa, whereas the central pin, shim, and coned nut are made of 34CrNiMo6 material with a minimum ultimate tensile strength of 900 MPa and a minimum yielding strength of 700 MPa.

Furthermore, two sizes of ISO 4762 tightening screws were used in the pin system, (1) M10×35 screws with the property class of 12.9 with further hardening to property class 16.9 and (2) M10×60 screws with the property class of 12.9. Table 1 presents the tested material properties of the components.

3 EXPERIMENTAL SETUP

The test jig was bolted to the test bench with the M8 bolt and nut. Both M10×35 and M10×60 screws were lubricated prior to the testing. The central pin, which has two strain gauges bounded on it with the difference of approximately 180°, see Fig. 5, was inserted in the test jig, and then one of the shims was inserted on each side of the pin. Coned nuts were screwed on both sides of the pin, which were also lubricated for easy installation. By using the recommended

Table 1. *Tested material properties of the components of both axial-radial pin systems*

Component	Ø50 mm pin system		Ø80 mm pin system	
	Tensile strength [MPa]	Yield strength [MPa]	Tensile strength [MPa]	Yield strength [MPa]
Central pin	1083	978	1081	980
Shim	1858	1438	1858	1438
Conned nut	1494	1352	1494	1352
Conical sleeve	540	391	500	379
End plate	547	403	505	379
M10×35	1625	–	1625	–
M10×60	1293	–	1312	–

cross-pattern from ASME PCC-1-2010 [19], M10x35 screws were screwed on both sides consecutively with a torque wrench starting from 40 Nm, as it is the minimum limit of the torque wrench. Then, the torque is increased stepwise by 20 Nm until the first screw breaks. Real-time strain values were measured with the help of the DAQ.

Fig. 5. *Locations of the strain gauges on the central pin*

Table 2. *Measured strains in the central pin for different levels of applied torque*

Torque levels [Nm]	Measured strain [μm/m]	
	Ø50 pin system	Ø80 pin system
0	0	0
40	368	222
60	609	312
80	873	416
100	1104	585
120	1366	676
140	1538	790

These measured strains are shown in Table 2 for both Ø50 mm and Ø80 mm pins for the given range of the applied torque levels. After setting the applied torque to 160 Nm on the torque wrench, the screws broke for both pin systems.

4 DISCUSSION OF RESULTS

For the sake of comparison with experimental results, preload per screw was calculated at different torque levels, which is shown in Table 3. The Ø50 mm pin system contains 7 screws at each pin end, and there are 12 screws in the Ø80 mm pin system. Therefore, multiplication of the number of screws with the "preload per screw" results in the maximum possible preload of pin system, shown in Table 3 for both pin systems.

To validate the theoretical calculations by experimental results, the average normal stress in the central pin is calculated at different levels of torque by using the equation:

$$\sigma = \frac{F_i}{A_t}, \tag{2}$$

where A_t is the tensile stress area of the central pin and can be estimated by using [20],

$$A_t = \frac{\pi}{4} \times \left[d - 0.93815 \times p \right]^2, \tag{3}$$

where p = 3 mm is the pitch and d is the diameter of the central pin. Values of theoretical average normal stresses for both pin systems are shown in Table 3.

Measured strain values from Table 2 are utilized to calculate the average normal stresses by using Young's modulus of E = 210 GPa for the central pin and the relationship between stress and strain. These relations are shown in Table 4 for different levels of the applied torque, along with percentage differences from the theoretical values. A positive difference means the measured value is higher than the theoretical value and vice versa for The negative difference. The average deviation of the experimental values from the theoretical values for Ø50 mm pin

Table 3. *Theoretical values of preload per screw, max. preload, and normal stress for both axial-radial pin systems*

Torque level [Nm]	Preload per screw [kN]	Ø50 mm pin		Ø80 mm pin	
		Max. Preload [kN]	Normal stress [MPa]	Max. Preload [kN]	Normal stress [MPa]
0	0	0	0	0	0
40	22.7	159.1	91.0	272.7	58.3
60	34.1	238.6	136.4	409.0	87.4
80	45.4	318.1	181.9	545.3	116.6
100	56.8	397.6	227.4	681.7	145.7
120	68.2	477.2	272.9	818.0	174.8
140	79.5	556.7	318.4	954.3	204.0
149.2	84.8	593.4	339.3	1017.3	217.4

Table 4. *Calculated values of average normal stress from measured strains, and difference with theoretical stress*

Torque level [N]	Ø50 mm pin		Ø80 mm pin	
	Normal stress from measured strain [MPa]	Difference from theoretical stress [%]	Normal stress from measured strain [MPa]	Difference with theoretical stress [%]
0	0	0	0	0
40	77.4	–14.9	46.5	–20.2
60	127.9	–6.3	65.4	–25.2
80	183.4	+0.8	87.4	–25.0
100	231.8	+1.9	122.8	–15.7
120	286.9	+5.1	142.0	–18.8
140	322.9	+1.4	165.8	–18.7

system is –2.0 % with A standard deviation of 7.4 and for the Ø80 mm pin system is about –20.6 % with a standard deviation of 3.8.

As illustrated in Fig. 6, there is a relatively good correlation between the theoretical values, given in Table 3, and the calculated values based on the strain measurements, Table 4, for both pin systems. However, the Ø80 mm pin reaches clearly a lower maximum pre-tension compared to that of the Ø50 mm pin. The reason is that when the pin diameter increases the number of tightening screws increases approximately linearly, but the cross-section area increases as a square of the pin diameter. The current design of both pin systems can be further optimized to yield higher preloads, which will be investigated later in this section.

For the Ø50 mm pin system, the values of measured strains are used only from strain gauge 1, due to an error incumbent while soldering the wires for strain gauge 2. Possible reasons for the deviation of the experimental values is the fact that, while applying torque, a fixture was used with torque wrench which might have absorbed some part of the torque.

As shown in Table 5, the calculated maximum preloads for the tested axial-radial pin systems are lower than the theoretical preloads for the standard bolts. Therefore, optimization is done regarding the numbers and sizes of tightening screws of the axial-radial pin.

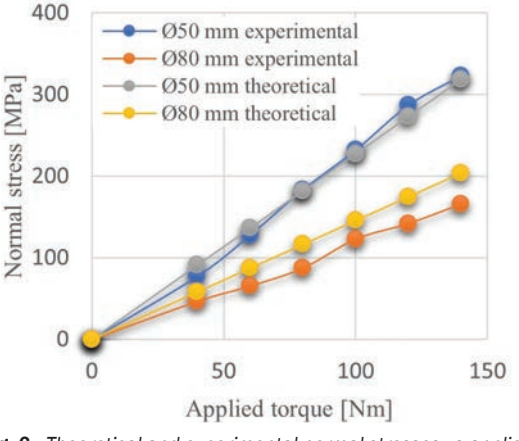

Fig. 6. *Theoretical and experimental normal stresses vs applied torque for both pin systems*

Table 5. *Maximum possible preload for both standard bolts and tested axial-radial pin systems*

Fastner size [mm]	Standard bolt [kN]	Tested pin [kN]	Diff. [%]
50	1067.6	593.4	–44.4
80	2741.1	1017.3	–62.9

The preload in the axial-radial pin systems is contributed by the torque applied to the M10×35

screw; to increase the applied torque, the combination of screw size and number must be optimized. The experiment showed by increasing the torque on the M10 screws results in the breakage of the screw.

The number of M10×60 screws is limited to 4, and the clearance between the two bolt heads is fixed to 1.5 mm. Based on these conditions, a relationship is derived to estimate the maximum number (X) of M10×35 screws in axial-radial pin system as:

$$X = \frac{\pi d_B}{d_H + 1.5} - 4, \tag{4}$$

where d_B is the bolt circle diameter of coned nut and d_H is the bolt head diameter. This relation is used to estimate the number of different sizes of screws for both Ø50 mm and Ø80 mm axial-radial pin systems, as shown in Table 6. There is a geometrical restriction on the number of screws as the bolt head diameter should be less than the difference between the minimum outer diameter and inner diameter of the coned nut.

Considering the described geometrical restriction, the possible screw sizes for the Ø50 mm and Ø80 mm pin systems are M12 and M14, respectively. It was also found important to investigate the possibility of using smaller size screws than M10, when M8 screws were used. Using thread diameters of M8, M10, M12, and M14 according to ISO 4762 and minimum tensile strength of 1600 MPa and the relationship presented in Section 2 as Eq. (1), maximum torque and "preload per screw" was estimated; then the maximum preloads for both pin systems were calculated. All the calculated values are presented in Table 6.

Table 7 compares the preloads for improved axial-radial pin systems as a percentage difference between the standard bolt and the tested axial-radial pin system. The percentage difference is reduced significantly for both axial-radial pin systems as previously (Table 5).

As shown in Fig. 7a, the radial load is being applied on the connected flanges, leading to the relative radial movements, and this connection

Table 6. *Theoretical max. possible preload for both axial-radial pin systems for different screw sizes and numbers*

Size	Thread diameter [mm]	Max. torque [Nm]	Preload per screw [kN]	Ø50 mm pin system		Ø80 mm pin system	
				Max. number of screws [-]	Preload [kN]	Max. number of screws [-]	Preload [kN]
M8	7.78	74.0	52.8	11	581.0	18	950.8
M10	9.78	146.9	83.5	9	751.2	14	1168.6
M12	11.73	253.5	120.1	7	840.5	12	1440.9
M14	13.73	406.6	164.5	–	–	10	1645.1

Table 7. *Comparison of preload for improved axial-radial pin system with standard bolts and tested pin system*

Fastner size [mm]	Preload [kN]			Difference [%]	
	Standard bolt	Tested axial-radial pin	Improved axial-radial pin	Improved axial-radial pin vs std. bolts	Improved axial-radial pin vs tested pin
50	1067.6	593.4	840.5	–21.3	29.4
80	2741.1	1017.3	1645.1	–40.0	38.2

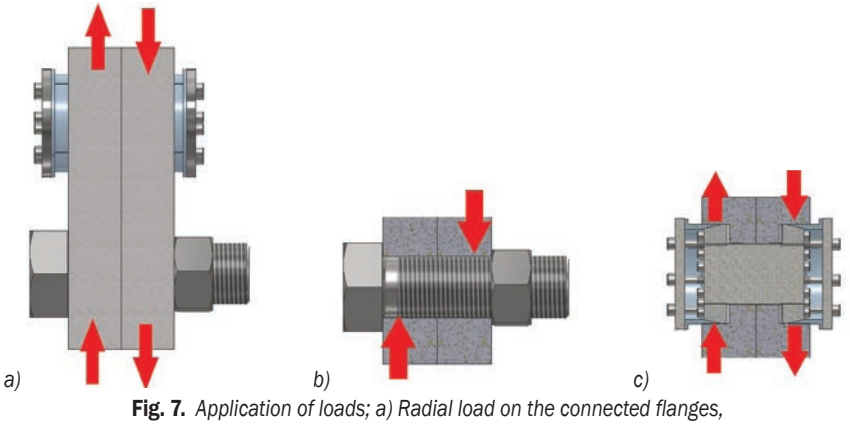

Fig. 7. *Application of loads; a) Radial load on the connected flanges, b) radial load on a standard bolt, c) radial load on the conical sleeve of axial-radial pin system*

contains both axial-radial pin system and standard bolt and nut. There is a surface resistance between mating surfaces of flanges, and it is acting in the opposite direction of the external radial load. This surface resistance is controlled by the permissible shear load or shear capacity and, according to Boris et al. [2], this shear capacity depends on the initial preload (Fi) and the coefficient of the friction (μ) between the mating surfaces of the flanges. This shear capacity is expressed as:

$$Q_p = \frac{F_i \mu}{k}, \tag{5}$$

where k is the factor of safety.

When the external radial load exceeds this shear capacity of a standard bolt, the external radial load starts to act freely on the bolt as shear load, as depicted in Fig. 7b. In contrast, the conical sleeves in the novel pin system are employed to make the connection as rigid as possible and to have a relative movement between connecting flanges. The external radial load applied on the conical sleeve, as shown in Fig. 7c, should be large enough to surpass the minimum shear strength of the central pin. This allows the inclusion of as another factor in the equation of shear capacity, which becomes:

$$Q_p = \frac{F_i \mu + \tau_Y A_t}{k}, \tag{6}$$

where τ_Y is the yield limit for shear strength of the central pin.

Eq. (5) is used to calculate the shear capacity of both standard bolts; the results are presented in Table 8, where the factor of safety is equal to 1. The values in this table do not account for the contribution of shear strength of bolt in the shear capacity of the connection.

Table 8. *Theoretical shear capacity of both M50 and M80 standard bolts*

Standard bolts	Maximum possible preload [kN]	Shear capacity [kN]
M50	1067.6	320.3
M80	2741.1	822.3

Table 9 presents the theoretical shear capacity of both axial-radial pins by using Eq. (6), along with the percentage increment of shear capacity in comparison to standard bolts. This increment illustrates the advantage of the axial-radial pin system over the standard bolt in terms of preventing the connection failure due to radial load. Here, the factor of safety is entirely dependent on the environmental condition of the flange joint, and it must be customized for each individual case, but for the sake of fair comparison, k = 1, μ = 0.3, and τ_Y = 450 MPa.

Table 9. *Theoretical shear capacity of both axial-radial pins and comparison of shear capacity increment*

Pin size [mm]	Max. preload [kN]	Tensile area [mm²]	Shear capacity [kN]	Shear capacity Inc. [%]
Ø50	840.5	1748.7	1043.0	225.7
Ø80	1645.1	4679.1	2599.1	216.1

Figs. 8 and 9 show comparative simulated situations between the axial radial pin system and standard bolt-nut connection, where two parallel plate connections are created by each fastener. In these simulations, an equal pressure load of 50 MPa as a radial load on each plate is applied in opposite directions, as shown in Figs. 8a and 9a, respectively. As expected, both fasteners have created the surface friction between plates, which are shown in Figs. 8b and 9b.

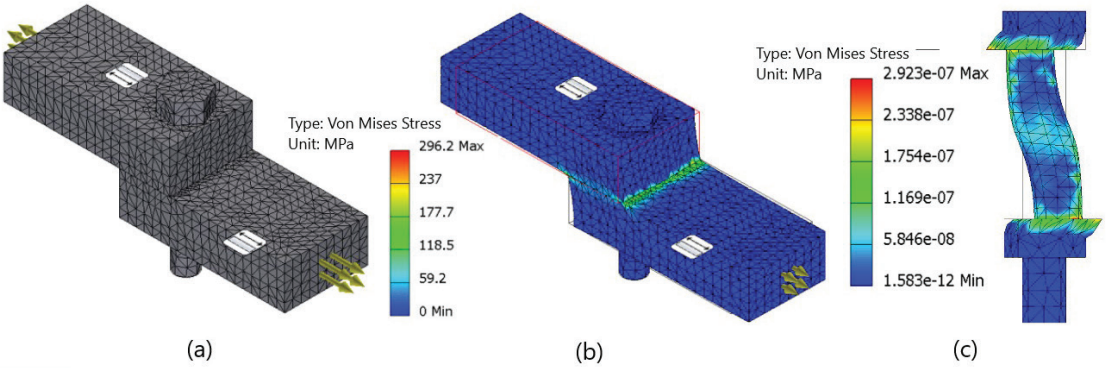

Fig. 8. *a) Mesh view of the parallel plate connection by standard bolt and nut, b) surface friction between two plates, and c) isolated view of the bolt and nut*

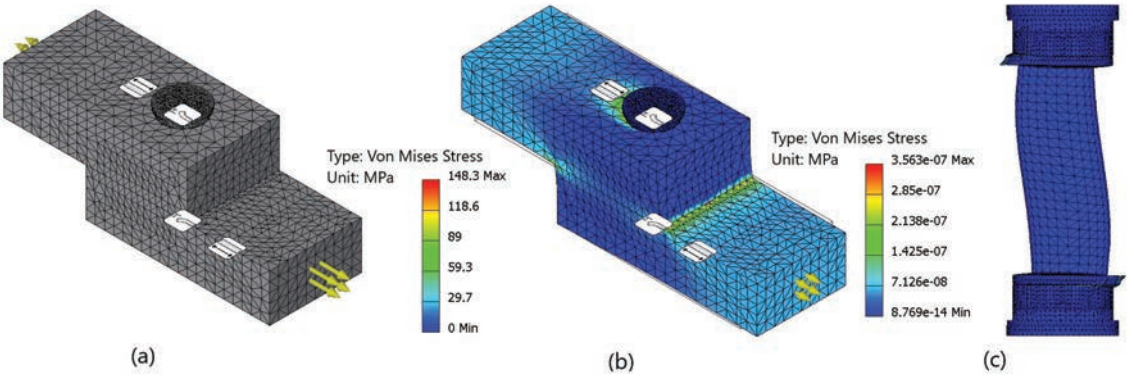

Fig. 9. *a) Mesh view of the parallel plate connection by axial radial pin system, b) surface friction between two plates, and c) isolated view of the pin system*

To understand the behaviour of both fasteners, they were isolated from the assembly and presented in Figs. 8c and 9c. In this case, the effect of the 50 MPa pressure is much disastrous for standard bolt-nut connection as there is major slipping in the high-stress areas (close to the bolt head and nut) as well as higher stress distribution in the centre of the shank, as compared to the axial-radial pin, where the relatively higher stress occurred in the conical sleeve, but the stress level in central pin is within elastic limit.

As shown in Table 10, the level of required torque to reach the maximum preload for each fastener is much higher for the standard bolt connection when compared to the axial-radial pin system connection. This is because torque is applied to several M12 and M14 screws in the axial-radial pin system, compared to high torque on a single M50 and M80 bolt for the standard bolts. Therefore, it is possible to apply torque by a simple torque wrench to the axial-radial pin system connection, whereas the standard bolt connection needs a high torque from a high-capacity torquing tool, typically hydraulic or electrical.

Table 10. *Required torque for axial-radial pin systems and standard bolts to reach maximum possible preload*

	Fastener	Required torque [Nm]
Axial-radial pin system	Ø50 mm /M12	253.5
	Ø80 mm /M14	406.6
Standard bolt	M50	9505.7
	M80	39106.8

Though the axial-radial pin system's improved design can provide a higher preload than the tested design, it is still less than the preload per pin for the standard bolts. The axial-radial pins require more space per pin than the standard bolts, and fewer pins will, therefore, fit on a defined flange system. To maximize the shear resistance for the complete flange system, it is, therefore, possible to apply a combination of standard bolts and axial-radial pins, for optimization purposes. The configuration can be decided by the design parameter responsible for radial movements.

5 CONCLUSION

With some deviation from the theoretical values, experiments confirm the maximum possible preload by both pin systems. In comparison with standard bolts of the same sizes, preload produced by an axial-radial pin system is lower than the standard bolt system, but with the presented changes in the initial design in this study, the difference in maximum preload is reduced significantly, 29 % in Ø50 mm pin system and 38 % in Ø80 mm pin system. The axial-radial pin has a locking mechanism based on the mechanical strength of the central pin. Theoretically, this locking system improves the capability of axial-radial pin connections by more than 200 % to avoid a failure due to radial loading as compared to the standard bolt connection. Along with that, the axial-radial pin requires significantly lower torque applied per screw as compared to standard bolts to obtain the maximum possible preload for a connection. Considering the advantages of the axial-radial pin in terms of capability to reduce or eliminate the failure due to radial loading and the ability of standard bolts to produce higher maximum possible preload, a practical solution is proposed, where a combination of both fasteners can be used to have a safe and secure flange connection. This expanding pin technology, particularly the axial-radial pin solution, is not well

known in the research community. With the results from this study, it is evident that the axial-radial pin solution is worth investigating further to obtain more knowledge about its potential, especially as a function of dimensions, material qualities and torque levels.

6 REFERENCES

[1] Luan, Y., Guan, Z.-Q., Cheng, G.-D., Liu, S. (2012). A simplified nonlinear dynamic model for the analysis of pipe structures with bolted flange joints. *Journal of Sound and Vibration*, vol. 331, no. 2, p. 325-344, **DOI:10.1016/j.jsv.2011.09.002**.

[2] Boris M.K., Barlam, D.M., Nystrom, F.E. (2008). *Machine Elements: Life and Design*. CRC Press, Taylor & Francis Group, Boca Raton.

[3] Abid, M., Nash, D.H. (2003). Comparative study of the behaviour of conventional gasketed and compact non-gasketed flanged pipe joints under bolt up and operating conditions. *International Journal of Pressure Vessels and Pipes*, vol. 80, no. 12, p. 831-841, **DOI:10.1016/j.ijpvp.2003.11.013**.

[4] Urse, G., Durbacá, I., Panait, I.C. (2018). Some research results on the tightness and strength of flange joints. *Journal of Engineering Sciences and Innovation*, vol. 3, no. 2, p. 107-130.

[5] Takaki, T., Satou, K., Yamanaka, Y., Fukuoka, T. (2008). Effects of flange rotation on the sealing performance of pipe flange connections. *Proceedings of the ASME/JSME 2004 Pressure Vessels and Piping Conference*, **DOI:10.1115/PVP2004-2630**.

[6] Ibrahim, R.A. (2010). Overview of mechanics of pipes conveying fluids-Part I: Fundamental studies. *Journal of Pressure Vessel and Technology*, vol. 132, no. 3, art. ID 034001, **DOI:10.1115/1.4001271**.

[7] Bai, Y., Yang, M. (2016). The influence of superimposed ultrasonic vibration on surface asperities deformation. *Journal of Materials Processing Technology*, vol. 229, p. 367-374, **DOI:10.1016/j.jmatprotec.2015.06.006**.

[8] Zhao, Y., Yang, C., Cai, L., Shi, W. Hong, Y. (2016). Stiffness and damping model of bolted joints with uneven surface contact pressure distribution. *Strojniški vestnik - Journal of Mechanical Engineering*, vol. 62, no. 11, p. 665-677, **DOI:10.5545/sv-jme.2016.3410**.

[9] Eurocode 3 (2005). *Design of steel structures - Part 1-9: fatigue*. EN-2005.

[10] Croccolo, D., De Agostnis, M., Vincenzi, N. (2011). Failure analysis of bolted joints: Effect of friction coefficients in torque-preloading relationship. *Engineering Failure Analysis*, vol. 18, no. 1, p. 364-373, **DOI:10.1016/j.engfailanal.2010.09.015**.

[11] Chu, S.J., Jeong, T.K., Jung, E.H. (2016). Effect of radial interference on torque capacity of press- and shrink-fit gears. *International Journal of Automotive Technology*, vol. 17, p. 763-768, **DOI:10.1007/s12239-016-0075-0**.

[12] Karlsen, Ø., Lemu, H.G. (2019). On modelling techniques for mechanical joints: Literature study. *International Workshop of Advanced Manufacturing and Automation*, vol. 634, p. 116-125, Springer, Singapore, **DOI:10.1007/978-981-15-2341-0_15**.

[13] Chakherlou, T.N., Vogwell, J. (2004). A novel method of cold expansion which creates near-uniform compressive tangential residual stress around a fastener hole. *Fatigue & Fracture of Engineering Materials & Structures*, vol. 27, no. 5, p. 3423-351, **DOI:10.1111/j.1460-2695.2004.00727.x**.

[14] Akhtar, M.M. (2020). *Expanding PIN System - Combined Radial and Axial Locking System*, MSc. Thesis, University of Stavanger, Stavanger.

[15] Bondura AS, Bondura Technology. from https://bondura.no/, accessed on: 2021-06-30.

[16] HBM. from: *https://www.hbm.com/en/*, accessed on: 2021-06-30.

[17] Purwasih, N., Kasai, N., Okazaki, S., Kihira, H. (2018). Development of amplifier circuit by active-dummy method for atmospheric corrosion monitoring in steel based on strain measurement. *Metals*, vol. 8, no. 1, art. ID 5, **DOI:10.3390/met8010005**.

[18] USAG company. Torque wrench with reversable ratchet. from: *https://www.usag.it/catalog/en/products/pdf/2309/Torquewrenches%20with%20reversibl%20ratchet.pdf*, accessed on 2021-06-30.

[19] ASME (2010). *Guidelines for Pressure Boundary Bolted Flange Joint Assembly*. USA Patent ASME PCC-1-2010.

[20] Norton, R.L. (2011). *Machine design: An integrated approach*, 4th Ed. Pearson Education Inc., New York.

Strojniški vestnik - Journal of Mechanical Engineering 67(2021)12, 635-648

DOI:10.5545/sv-jme.2021.7327 Original Scientific Paper
Received for review: 2021-07-13
Received revised form: 2021-10-23
Accepted for publication: 2021-11-09

Modelling and Multi-objective Optimization of Elastic Abrasive Cutting of C45 and 42Cr4 Steels

Irina Aleksandrova[1,*] – Anna Stoynova[2] – Anatoliy Aleksandrov[1]
[1]Technical University of Gabrovo, Bulgaria
[2]Technical University of Sofia, Bulgaria

Elastic abrasive cutting is a new high-performance method to produce workpieces made of materials of different hardness, which ensures lower wear of cut-off wheels and higher quality machined surfaces. However, the literature referring to elastic abrasive cutting is scarce; additional studies are thus needed. This paper proposes a new approach for modelling and optimizing the elastic abrasive cutting process, reflecting the specifics of its particular implementation. A generalized utility function has been chosen as an optimization parameter. It appears as a complex indicator characterizing the response variables of the elastic abrasive cutting process. The proposed approach has been applied to determine the optimum conditions of elastic abrasive cutting of C45 and 42Cr4 steels. To solve the optimization problem, a model of the generalized utility function reflecting the complex influence of the elastic abrasive cutting conditions has been developed. It is based on the findings of the complex study and modelling of the response variables of the elastic abrasive cutting process (cut-off wheel wear, time per cut, cut piece temperature, cut off wheel temperature and workpiece temperature) depending on the conditions of its implementation (compression force F exerted by the cut-off wheel on the workpiece, workpiece rotational frequency n_w, cut off wheel diameter d_s). By applying a genetic algorithm, the optimal conditions of elastic abrasive cutting of C45 and 42Cr4 steels: d_s = 120 mm; F = 1 daN; n_w = 63.7 min^{-1} and n_w = 49.9 min^{-1}, respectively for C45 and 42Cr4 steels, have been determined. They provide the best match between the response variables of the elastic abrasive cutting process.

Keywords: elastic abrasive cutting; multi-objective optimization; generalized utility function; C45 and 42Cr4 steels

Highlights

- *A new approach to modelling and multipurpose optimization of elastic abrasive cutting based on a generalized utility function has been performed.*
- *Regression models for the elastic abrasive cutting response variables depending on the cutting conditions have been built.*
- *A model of the generalized utility function as a complex indicator characterizing the response variables of the elastic abrasive cutting process has been developed.*
- *By applying a genetic algorithm, the optimum conditions of elastic abrasive cutting of C45 and 42Cr4 steels, under which the generalized utility function has a maximum, have been determined.*
- *The proposed multipurpose optimization approach ensures the best match between the response variables of the elastic abrasive cutting process.*

0 INTRODUCTION

Abrasive cutting is a high-performance, cost-effective method widely used in present-day manufacturing environments to produce workpieces made of ferrous and non-ferrous metals and alloys, and non-metallic materials of high hardness. This is a complex and varied process performed under different kinematic schema; the cut-off wheel has two motions: main rotation and radial feed **[1]** to **[3]**. The radial feed of the tool is ensured either by the cut-off machine in a kinematic way (hard abrasive cutting) or by maintaining a constant compression force F exerted by the wheel on the workpiece (elastic abrasive cutting) **[4]**. The workpiece is motionless, performs an oscillatory motion or rotates at a constant rotational frequency n_w.

During elastic abrasive cutting (Fig. 1), the contact arc length L and the thickness h of the layer being cut vary, while the instantaneous cross-section area of the layer being cut remains constant. The introduction of rotary motion of the workpiece leads to a decrease in the working stroke of the cut-off wheel, which ensures shorter time per cut and a wear reduction of abrasive wheels. At the same time, the tool lifetime, process production rate, cutting forces, power rate, and temperature depend on the compression force F, workpiece rotational frequency n_w, cut off wheel diameter d_s and the type of material being machined. This makes the schema for elastic abrasive cutting a topical subject of study and optimization.

The abrasive cutting process is a sophisticated multi-parameter and multi-factor subject of study, modelling, and optimization. It is characterized by a number of target parameters, each having a specific meaning yet insufficient for its optimum control. On the one hand, abrasive cutting is distinguished by its high performance, universality and low cost. On

*Corr. Author's Address: Technical University of Gabrovo, 4 H. Dimitar St, Gabrovo, Bulgaria, irina@tugab.bg

the other hand, the process is accompanied by high temperatures (above 1000 °C) in the cutting zone, which, in turn, results in intensive cut-off wheel wear, deterioration of the tool cutting ability, changes in the microstructure of the material being machined and the occurrence of thermal flaws [5] to [7].

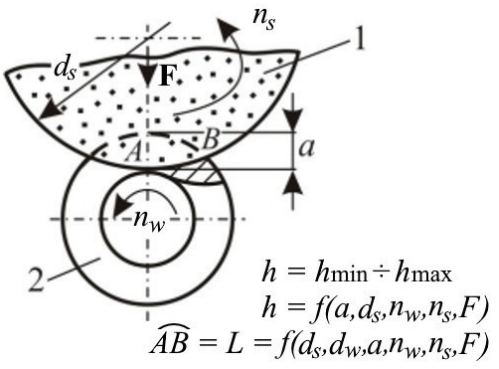

Fig. 1. *Schema of elastic abrasive cutting; 1 cut- off wheel; 2 workpiece*

The response variables of the abrasive cutting process are determined by numerous control factors: the physio-mechanical properties of the materials being machined, cutting mode components, cut-off wheel type and characteristics, type and way of supplying cooling fluids, etc. They are described in several publications.

Lopes et al. [8] studied the abrasive cut-off operation of low and medium carbon steels, using aluminium oxide discs of different feed rates. They monitored the cutting power, disc wear, and process temperature and established that an increase of 130 % in feed rate led to a decrease of approximately 57 % in maximum temperature and 84 % in diametrical wheel wear, thus improving process efficiency, but also to an increase of consumed cutting power by up to 127 %. A simulation model of high accuracy for predicting temperature was proposed that could be applied to predict and prevent thermal damages.

Luo et al. [9] studied the characteristics and wear modes of diamond grits in the cut-off grinding BK7 glass using thin diamond wheels, as well as the grinding forces, the grinding ratio, the width of cut, the straightness of cut and chipping produced during the cut-off grinding. The results showed that at a lower transverse velocity, a freer cutting ability, a better grinding ratio and a better straightness of cut were obtained. An increase of the transverse velocity led to diamond wheel wear accompanied by some macro-breakage and flattening of the tool work surface, thus resulting in unstable grinding forces, a low grinding ratio and poor straightness of cut.

Neugebauer et al. [2] studied the wear of cut-off wheels with different abrasive grains in the abrasive cutting of structural and stainless steels. They established that cubical grits were distinguished by the most extended lifetime compared to splinter-shaped grits due to their higher toughness and adhesion to the bond. By comparing the cutting performance of discs with different compositions in dry cutting of steel bars, Ortega et al. [10] observed that the abrasive type and size and disc binder were the most influential factors. On the basis of the results obtained, they concluded that discs with high grit size and protrusion, high grit retention by bond material, and closer mesh of fibreglass matrix binder were the optimal solution for abrasive cutting of mild steel parts. Riga and Scott [11] established the decisive influence of the type and composition of the cut-off wheel bond on the mechanical properties and nature of abrasive tool wear. The significant impact of the chemical composition and mechanical properties of the material being machined, the type and size of abrasive grains, the hardness of cut-off wheel and the cutting conditions (cut-off wheel speed and feed speed) on cut-off wheel wear was confirmed by the mathematical model developed by Yoshida et al. [12].

Ojolo et al. [13] found that the grinding/wear ratio and cutting time depended on the hardness and chemical composition of the material being machined. The tests were done by hard abrasive cutting of mild steel and stainless-steel rods. The grinding ratio in the elastic abrasive cutting of steel rods was also determined by Kaczmarek [5] and [14], using the results from the investigation of the cut-off wheel temperature. The author noted that the combination of a higher cut off wheel diameter and a higher feed force resulted in generating higher temperatures and obtaining lower values of G-ratio. These results were linked to cut off wheel wear and self-sharpening.

Levchenko and Pokintelitsa [7] analysed the interaction between the cut-off wheel and the cut pipe billet on the basis of heat-deforming analysis and they established the relationship between processing conditions and cutting conditions with the design parameters of the abrasive tool. To obtain lower temperatures and higher grinding ratios, Sahu and Sagar [6] proposed cut-off wheels with radial passages on their surfaces to supply the cutting fluid to the cutting zone. Upon studying four different eco-friendly water-based fluids in cutting medium carbon steel, Ni et al. [15] observed that the water-based fluid with surfactant provided the best results, as it

increased the G-ratio (by 77.6 %) and decreased the cutting tilt (by 14.8 %) and lin span (by 34.5 %) in comparison with dry cutting.

Yamasaka et al. [16] studied the application of abrasive cutting with diamond wheels used for machining the electromechanical parts of brittle materials, such as alumina ceramics. They found that the straightness of the sliced surface strongly correlated with the axial deflection of a thin grinding wheel, which was caused by the side forces acting on the side surfaces of the cut-off wheel. In this regard, they recommended decreasing the side force both by decreasing the depth of cut with retaining a stock removal rate and by improving the flatness on the side surfaces of the cut-off wheel to improve straightness. The results obtained by Braz et al. [17] in relation to the abrasive cutting of titanium showed that wheels with abrasives of silicon carbide and 30 mesh grain size combined with an extremely hard bond material led to the lowest values of depth of the affected zone.

Many studies confirm that by changing the abrasive cutting conditions, the thermal flows and the distribution of temperature in the tool, chips, workpiece and cut piece can be controlled, thus providing possibilities for enhancing tool lifetime, cutting process intensity and quality of machined surfaces.

Wang et al. [18] developed a three-dimensional numerical model to calculate the grinding temperature field distribution. The effect of the workpiece feed velocity, cooling coefficient and the depth of cut on temperature distribution were considered. Eshghy [19] studied the thermal flux in the chip, cut-off wheel and ambience and pointed out that 31 % of the thermal energy was released from the chips, 18 % from the ambience, 50 % from the wheel and only 1 % from the piece. Thermal optimum conditions were defined, and a procedure for selecting optimum down-feed rates was given. Hou and Komanduri [20] developed a heat source model and calculated heat partition in cut-off operations. They established that 60 % to 75 % of the heat was removed by the chip, 20 % to 35 % by the workpiece and 1 % by the cut-off wheel. Therefore, the authors thought that the thermal softening of the bond resulted from the heat released by the flying chips.

By using finite element (FE) analysis, Putz et al. [3] modelled heat distribution inside a steel bar under different cutting conditions. By adapting the cutting parameters and cooling strategy, the critical workpiece maximum temperature was decreased by 48 %. The authors proposed an alternative grinding strategy that combined the benefits of feed rate reduction, swing grinding and increased coolant velocity and ensured a decrease of the cutting power, wheel wear and piece temperature. The FE model for studying and analysing the temperature distribution in the machined bar during grinding is presented in [21], where two basic strategies for decreasing the temperature in the cutting zone are proposed: optimization of the cutting parameters (the feed speed) and application of the cubic boron nitride (CBN)-grinding technology. As a result, thermal damage decreases, and a cutting operation of high quality is ensured.

The analytical methods to calculate grinding temperatures and their effect on thermal damages were developed by Malkin and Guo [22]. According to them, the critical factor by means of which thermal damages in abrasive cutting could be controlled was the energy partition to the workpiece, which was within the range of 60 % to 85 %. This amount was considerably smaller in abrasive cutting with CBN discs with lower feed and slower workspeeds when using appropriate cooling fluids.

By applying the method of infrared thermography and planned experiment, Stoynova et al. [23] and [24] established that the workpiece rotational frequency had the greatest effect on temperature. As it increased (approximately 3 times), the temperatures of the cut piece and cut off wheel decreased (by up to 29 % and 19 %, respectively) whereas the workpiece temperature increased by up to 12 %. Temperature models of the workpiece, chip, piece being machined, and cut-off wheel in abrasive cutting were also built [25].

The analysis of the publications related to abrasive cutting shows that each abrasive cutting process is unique and could be studied from different perspectives: technological, energetic, informational, organizational, etc. Hard abrasive cutting is a well-studied process [3], [8] to [13] and [15] to [21] and the optimum conditions for its implementation are determined, too [26] to [28].

Elastic abrasive cutting is of great interest since it is a new high-performance method ensuring the stabilization of the dynamic and thermal phenomena in the cutting zone, thus reducing cut-off wheel wear and improving the quality of machined surfaces [14], [23], [29] and [30]. However, the literature referring to elastic abrasive cutting is scarce; thus, additional studies are needed. The adjustment of cutting operations is often done on the basis of the experience of the skilled staff or by using data from handbooks. Currently, there are no mathematical models that cover all aspects of elastic abrasive cutting and connect all its parameters with the cutting conditions. To increase

the efficiency and applicability of elastic abrasive cutting, it is necessary to study, model, and optimize its behaviour so as to achieve certain economic and technological criteria, taking into consideration the specific nature and conditions for its implementation.

In this regard, the paper proposes a new approach to the modelling and multipurpose optimization of elastic abrasive cutting, which reflects the specifics of its particular implementation in cutting two types of structural steels (C45 – medium carbon steel and 42Cr4 – alloy chrome steel), which are widely used in machine building for producing workpieces. The optimum conditions to implement the process are determined and verified to ensure the best match between the rate of cut-off wheel wear, time per cut, cut piece temperature, cut off wheel temperature and workpiece temperature. This will ensure higher productivity of the elastic abrasive cutting process and lower costs, as well as higher quality of the machined surfaces of the structural steels under study.

Taking into account the high productivity and low cost of the elastic abrasive process, the proposed multipurpose optimization approach and the obtained theoretical-experimental results presented in this paper could be used in every enterprise specialized in machine building.

1 INVESTIGATION AND MODELLING OF ELASTIC ABRASIVE CUTTING RESPONSE VARIABLES

1.1 Equipment, Materials, Methods

The purpose of this study is to establish the correlation dependencies between the response variables of the elastic abrasive cutting process: cut-off wheel wear δ_h, cut off wheel temperature $T_{s,h}$, workpiece temperature $T_{w,h}$, cut piece temperature $T_{d,h}$ and time per cut $t_{c,h}$ (h is index corresponding to the type of material being machined; h = 1 for elastic abrasive cutting of C45 steel; h = 2 for elastic abrasive cutting of 42Cr4 steel), and the conditions required to perform the process. Therefore, the cut-off wheel diameter d_s, the compression force F and the workpiece rotational frequency n_w were chosen as control factors.

To perform the elastic abrasive cutting process, a special attachment (Fig. 2) was designed. It is fixed to the main carriage of a combination lathe, supplied with a device for a stepless adjustment of workpiece rotational frequency n_w. The attachment comprises an angle grinder (2), which ensures constant rotational frequency of the cut-off wheel (n_s = 8500 min^{-1}), and a unit for adjusting the amount of the compression force F of the cut-off wheel (3) exerted on the workpiece (1). An angle grinder (GA7020 model) is attached to the front end of the arm (5), which is fixed by a bearing (4). A counterweight (6), whose weight is greater than that of the angle grinder, is fixed on the opposite end of the arm. The compression force of the abrasive wheel F exerted on the workpiece is regulated by moving the counterweight along the arm (5). The cut-off wheel stroke in cutting is limited by a locking screw. An aspirator system (7) is included to arrest, collect and remove the flying chips and sparks during abrasive cutting. The principle description of the experimental setup is shown in Fig. 2.

Fig. 2. *Work stand for elastic abrasive cutting*

Experimental studies have been conducted during counter-directional cutting with high speed reinforced cut-off wheels 41-180x22.2x3.0 A30RBF, produced by the Abrasive Tools Factory – Berkovitsa, Bulgaria [31]. The abrasive wheels are marked in compliance with EN 12413:2007: type and size of the cut-off wheel; abrasive material type; A = aluminium oxide; grit size according to ISO 8486 – 30 (Coarse); hardness grade, R = hard; bond, BF = fibre-reinforced resinoid bond.

The materials being machined are C45 (1.0503) and 42Cr4 (1.7045) steels (BS EN 10277-2:2015 [32]) (Table 1). They are in the shape of cylindrical rods of diameter d_w = 30 mm.

The general form of the models describing the relationship between the studied parameters (cut-off wheel wear, cut off wheel temperature, workpiece temperature, cut piece temperature and time per cut) and the group of independent variables (factors $d_s(X_1)$, $F(X_2)$ and $n_w(X_3)$) is:

$$y_{g,h} = b_0 + \sum_{i=1}^{3} b_i X_i + \sum_{i=1}^{3} b_{ii} X_i^2 + \sum\sum_{i<j} b_{ij} X_i X_j, \quad (1)$$

where g = 1 to 5, for index corresponding to the type of the studied elastic abrasive cutting parameter: $y_{1,1} = \delta_1$, $y_{2,1} = T_{s,1}$, $y_{3,1} = T_{w,1}$, $y_{4,1} = T_{d,1}$, $y_{5,1} = t_{c,1}$, $y_{1,2} = \delta_2$, $y_{2,2} = T_{s,2}$, $y_{3,2} = T_{w,2}$, $y_{4,2} = T_{d,2}$, $y_{5,2} = t_{c,2}$.

Table 1. *Chemical composition and physio-mechanical properties of the steels studied*

Steel type	Chemical composition				Tensile strength [MPa]	Hardness [HB]
	C [%]	Mn [%]	Cr [%]	Si [%]		
C45	0.44	0.5	0.2	0.2	750	192
42Cr4	0.4	0.5	1	0.25	1000	205

The form of the model was chosen on the basis of the theoretical and experimental studies of the effect of elastic abrasive cutting conditions on cut-off wheel wear, temperature and cutting ability as the non-linear nature of experimental dependencies $\delta_h = f(d_s, F, n_w)$, $T_{s,h} = f(d_s, F, n_w)$, $T_{w,h} = f(d_s, F, n_w)$, $T_{d,h} = f(d_s, F, n_w)$, and $T_{c,h} = f(d_s, F, n_w)$ were taken into account [23], [29] and [30].

To build the theoretical and experimental models in Eq. (1), multi-factor experiments were conducted using an orthogonal central-composite design. The number of trials is $N = 2^n + 2n + 1 = 15$ ($n = 3$ is the number of control factors). Three observations were made for each experiment. The variation limits of control factors are presented in Table 2. They are determined on the basis of the conducted experimental studies on the temperature in elastic abrasive cutting and the performance of cut-off wheels estimated by the parameters: wear, tool life, and cutting ability [23], [29] and [30].

The models were built using the measured values of the cut-off wheel wear, cut-off wheel maximum contact temperature, workpiece maximum instantaneous temperature, cut piece temperature at the end of the cut-off cycle and time per cut. Each measurement of wear, time per cut and temperature were performed three times.

Table 2. *Factor levels in the experimental design*

Factors		Factor levels		
		–1	0	+1
X_1	d_s [mm]	120	150	180
X_2	F [daN]	1	2	3
X_3	n_w [min^{-1}]	22	91	160

The cut-off wheel wear was determined as a mean value of the differences between the tool diameters measured in two mutually perpendicular directions at the beginning and the end of the respective observation performed under specific cutting conditions. Cut-off wheel diameters were measured using a Mitutoyo Digital Calliper, ABSOLUTE, LCD of Range: 0 mm to 200 mm, Resolution: 0.01 mm, Accuracy: ±0.02 mm, Repeatability: 0.01 mm.

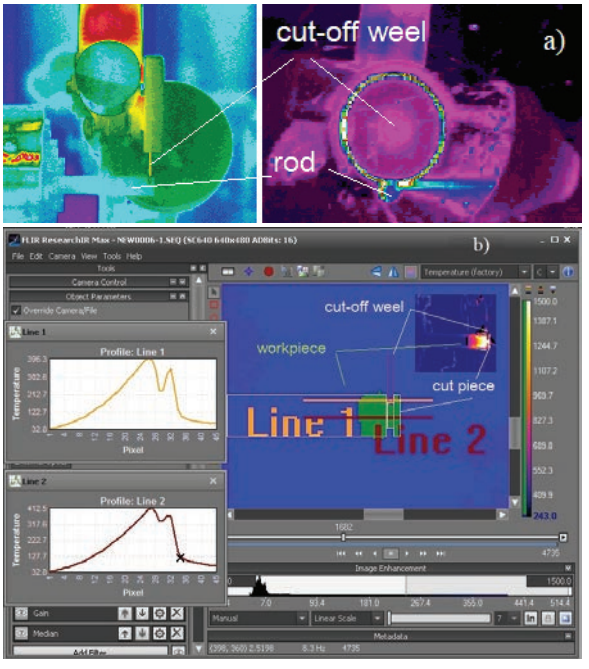

Fig. 3. *Illustration of thermography measurement process of cut-off wheel, workpiece and cut piece temperatures, respectively in elastic abrasive cutting of cylindrical rods*

The time per cut corresponds to the duration of the respective cut-off cycle. The cut-off wheel, workpiece and cut piece, and respective maximum contact temperatures during the elastic abrasive cutting of cylindrical rods, were measured using a thermal imaging camera. Non-destructive thermography measurement leads to a reduction of measurement temperature errors compared to thermocouple measurement, as described in [23] and [33]. The whole cutting process was registered by infrared cameras ThermaCam FLIR SC640, with an image resolution of 640 × 480 pixels, temperature measurement range from –40 ºC to +2000 ºC, reading accuracy of ±2 % and IP-link using FireWire. Thermovision SDK software was used to manage, change settings, and control the calibration of the cameras. The ResearchIR MAX software package was also used for real-time monitoring and temperature measurements of the cutting area, selected as the region of interest (ROI). Surface temperature measurements were recorded simultaneously in two ROI positions: cutoff wheel profile and face view of side (Fig. 3a).

Fig. 3b illustrates real-time monitoring and surface temperature measurement of the cutting area using ResearchIR MAX.

Further thermograms processing was performed in MATHLAB, for noise reduction, contouring, additional analysis, recognition and classification of the areas with the highest and lowest temperature or other ROI interesting areas.

1.2 Experimental Results and Modelling

The designs of the experiments, including the values of the studied response variables of the elastic abrasive cutting process, are presented in Table 3.

After statistical analysis of the experimental results and by applying the regression analysis method and QstatLab software [34], theoretical and experimental models of the cut-off wheel wear, cutoff wheel temperature, workpiece temperature, cut piece temperature and time per cut were made (Table 4).

The regression models include only the significant regression coefficients determined in accordance with the condition $\hat{t} > t_{g,h(\alpha/2,v)}$, where $\hat{t}$ and $t_{g,h(\alpha/2,v)}$ are, respectively, the calculated values of Student's *t*-criterion for each coefficient b_0, b_i, b_{ij}, b_{ii} of the regression equations, the general form of which is presented by Eq. (1) and the tabular value of Student's *t*-criterion ($\alpha = 0.05$ is the significance level; $v = N - k$ is the number of degrees of freedom; *k* is the number of coefficients in the model), presented for each model in Table 4. The constructed models are relevant since the condition $\widehat{F}_{g,h} > F_{g,h(\alpha,v_1,v_2)}$ has been met with a confidence level of 95 %. The calculated $\widehat{F}_{g,h}$ and tabular $F_{g,h(\alpha,v_1,v_2)}$ values of the Fisher criterion ($\alpha = 0.05$; $v_1 = k - 1$ and $v_2 = N - k$ are degrees of freedom) for each regression model are presented in Table 4. The theoretical and experimental models extremely accurately describe the dependencies between the studied response variables and the control factors. The values of the determination coefficients are $\widehat{R}^2_{g,h} = 0.880$ to 0.999 (Table 4).

The effect of cutting conditions on the cut-off wheel wear, cutoff wheel temperature, workpiece temperature, cut piece temperature and time per cut according to the created theoretical and experimental models (Table 4) is graphically presented in Fig. 4. To determine the impact rate of control factors on the studied response variables of the elastic abrasive cutting process, an analysis of variance (ANOVA) was conducted.

1.3 Analysis of Experimental Results

The investigation of the response variables of the elastic abrasive cutting process shows that they depend, to a large extent, on the conditions for implementing the process. However, the effect of the cut-off wheel diameter, compression force, and workpiece rotational frequency on the cut-off wheel wear, time per cut, cut piece temperature, workpiece temperature and cut off wheel temperature is different, and it is related to the theoretically established influence of d_s, F and n_w on the length of the contact arc between the cut-off wheel and the workpiece, the

Table 3. *Design of the experiments and response variables of the elastic abrasive cutting process of C45 and 42Cr4 steels*

Control factors			Response variables									
			Cut-off wheel wear		Cut-off wheel temperature		Workpiece temperature		Cut piece temperature		Time per cut	
d_s [mm]	F [daN]	n_w [min-1]	δ_1 [mm]	δ_1 [mm]	$T_{s,1}$ [°C]	$T_{s,2}$ [°C]	$T_{w,1}$ [°C]	$T_{w,2}$ [°C]	$T_{d,1}$ [°C]	$T_{d,2}$ [°C]	$t_{c,1}$ [s]	$t_{c,2}$ [s]
120	1	22	0.977	1.051	160	164	970	989	201	215	10.90	12.08
180	1	22	0.551	0.583	195	200	830	850	220	235	9.91	10.80
120	3	22	1.882	1.981	175	179	989	1008	208	223	8.90	10.06
180	3	22	1.422	1.513	205	210	863	880	235	251	7.90	8.86
120	1	160	3.141	3.272	135	144	1093	1149	145	154	12.9	14.88
180	1	160	2.294	2.390	150	160	950	1000	170	180	11.87	13.64
120	3	160	4.476	4.865	160	172	1125	1184	152	161	10.94	12.69
180	3	160	4.307	4.631	180	193	965	1015	184	195	9.87	11.45
120	2	91	2.528	2.689	149	156	907	936	173	184	10.96	12.49
180	2	91	2.109	2.221	183	190	838	864	207	222	9.89	11.37
150	1	91	1.652	1.721	157	165	865	889	193	205	11.40	12.80
150	3	91	2.948	3.189	173	182	879	905	206	219	9.40	10.52
150	2	22	1.218	1.282	185	196	805	838	215	230	9.45	10.58
150	2	160	3.374	3.628	156	164	933	956	180	192	11.41	13.12
150	2	91	2.308	2.455	165	175	872	900	202	215	10.43	10.43

Table 4. *Theoretical and experimental models of cut-off wheel wear, temperature and time per cut during elastic abrasive cutting and statistical characteristics of the models*

Steel, type	Response variables	Models	Student's criterion	Fisher criterion		Determination coefficient
				Calculated	Tabular	
C45	Cut-off wheel wear	$\delta_1 = 1.218 - 0.008d_s + 0.382F + 0.011n_w + 0.003Fn_w$	2.228	294.382	3.478	0.988
	Temperature of the cut-off wheel	$T_{s,1} = 103.865 + 0.447d_s + 8F - 0.201n_w$	2.201	48.371	3.587	0.910
	Temperature of the workpiece	$T_{w,1} = 2603.317 - 19.479d_s - 194.928F + 0.0578d_s^2 + +51.557F^2 + 0.005n_w^2$	2.262	38.234	3.482	0.930
	Temperature of the cut piece	$T_{d,1} = -88.426 + 3.69d_s + 4.667F - 0.359n_w - 0.011d_s^2$	2.228	98.168	3.478	0.965
	Time per cut	$t_{c,1} = 13.486 - 0.017d_s - 0.881F + 0.015n_w - 0.029F^2 - -6.6.10^{-6}d_s n_w$	2.262	19098,664	3.481	0.999
42Cr4	Cut-off wheel wear	$\delta_2 = 1.344 - 0.008d_s + 0,391F + 0.011n_w + 0.004Fn_w$	2.228	370,829	3.478	0.991
	Temperature of the cut-off wheel	$T_{s,2} = 105.799 + 0.46d_s + 8.583F - 0.168n_w$	2.201	35.092	3.587	0.880
	Temperature of the workpiece	$T_{w,2} = 2695.024 - 21.143d_s - 140.028F + 0.063d_s^2 + +37.403F^2 + 0.006n_w^2$	2.262	38.494	3.482	0.931
	Temperature of the cut piece	$T_{d,2} = -89.928 + 3.887d_s + 5F - 0.394n_w - 0.011d_s^2$	2.228	90.495	3.478	0.962
	Time per cut	$t_{c,2} = 15.212 - 0.02d_s - 1.062F + 0.019n_w$	2.201	863.138	3.587	0.994

depth of cut and the thickness of the layer of material being cut by one abrasive grain **[29]** and **[35]**.

The analysis of the theoretical and experimental models (Table 4) and the graphics plotted on the basis of them (Fig. 4), as well as the interpretation of ANOVA results, allow us to draw the following conclusions:

(1) The workpiece rotational frequency has the highest effect on the elastic abrasive cutting process response variables. The increase of n_w within the range being studied results in increasing cut-off wheel wear (from 2.4 to 4.2 times depending on the compressive force and cut off wheel diameter), time per cut (by up to 25 %), and workpiece temperature (by up to 18 %), as well as in decreasing cut piece temperature (by up to 29 %) and cut off wheel temperature (by up to 17.6 %). The intensified cut-off wheel wear and the increased time per cut are connected with the increased thickness of the layer being cut off by one abrasive grain, thus resulting in increasing the load of abrasive grains and establishing preconditions for faster filling of the cut off wheel pores with chips **[29]** and **[35]**, as well as with the change of the ratio between the normal and main cutting force, which results in deteriorating the possibilities for abrasive grain cutting **[30]**. The decrease of cut piece temperature is caused by the enhanced heat removal resulting from the thicker layer being cut and the cross section of the chip being cut off by one abrasive grain **[29]** and **[35]**, as well as the time per cut. The increased workpiece temperature and the decreased cut off wheel temperature are linked to an increase of the contact area between the cut-off wheel and the workpiece, as well as to the fact that in the course of cutting the workpiece appears a tool coolant absorbing part of the released heat, which consequently is transferred to the chip.

(2) As the cut-off wheel diameter d_s decreases within the range under study, both the tool wear size and time per cut increase, from 11 % to 94 % and from 9 % to 14 %, respectively. That tendency could be explained with the decrease in the number of abrasive grains involved in the removal of the layer being cut per revolution of the cut-off wheel, the increase of the thickness of the chip being cut by one abrasive grain, respectively, the load on the abrasive grains, as well as with the inevitable decrease of the cut-off wheel speed since the rotational frequency n_s is constant **[29]** and **[35]**. All this deteriorates the cutting ability of the abrasive grains and logically results in intensifying tool wear and increasing time per cut. The influence of cut-off wheel diameter on tool wear and time per cut depends on the compression force, workpiece rotational frequency, and the effect of d_s on the wear decreases as the compression force and workpiece

rotational frequency increase. As the workpiece rotational frequency increases and the compression force decreases, the effect of d_s on the time per cut increases.

(3) As d_s decreases, the temperatures of the cut piece and cut-off wheel also decrease, whereas the workpiece temperature increases within a range of 11 % to 17 %. That is linked to an increase of the thickness of the layer of material being cut and the cross-section of the chip being cut by one abrasive grain [29] and [35], which enhances heat removal and to an increase of time per abrasive cut and a decrease of cutting speed.

(4) The increase of the compression force F results in decreasing elastic abrasive time per cut (by 14 % to 20 %), respectively, increasing process performance in increasing cut-off wheel wear (from 1.6 to 2.7 times). That is linked to the increase of the length of contact arc and the depth of cut [29] and [35], as a result of which cut off wheel pores are filled with chips and abrasive particles faster. The effect of the compression force increases when the cut-off wheel diameter increases and the workpiece rotational frequency decreases.

(5) The compression force has little effect on temperature. As it increases, the temperatures of the cut piece, cut-off wheel and workpiece increase by 5 % to 11 %. The minimum effect of the compression force is related to the fact that when F increases, elastic abrasive time per cut decreases and, in contrast, the length of contact arc and the depth of cut increase [29] and [35].

(6) The nature and level of influence of workpiece rotational frequency, cut off wheel diameter and compression force on cut-off wheel wear, time per cut and elastic abrasive cutting temperature are equal for the two materials being machined (C45 and 42Cr4 steels). Nevertheless, the temperatures of cut-off wheel, workpiece, and cut piece are higher when machining 42Cr4 steel (by 1.9 % to 7.5 %), which is related to the higher hardness and strength of this material. The values of cut-off wheel wear and time per cut are also higher, respectively by 4.2 % to 8.7 % and by 9 % to 11 %.

2 OPTIMIZATION OF ELASTIC ABRASIVE CUTTING CONDITIONS

2.1 Optimization Method

The undertaken investigation, modelling, and analysis of the response variables of the elastic abrasive cutting process show complicated and different nature of change of cut-off wheel wear, cut-off

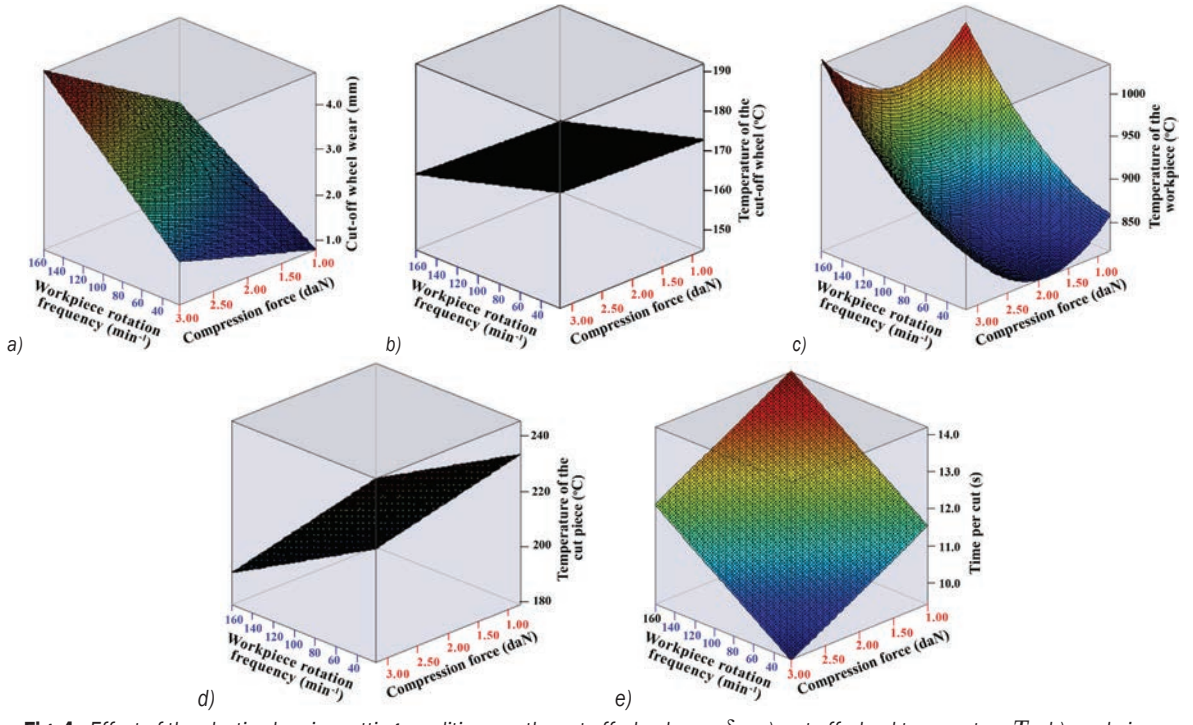

Fig. 4. *Effect of the elastic abrasive cutting conditions on the cut-off wheel wear δ_s ; a), cut off wheel temperature T_s , b), workpiece temperature T_w , c), cut piece temperature T_d , d) and time per cut t_c , e) (for steel 42Cr4, d_s = 150 mm)*

wheel temperature, workpiece temperature, cut piece temperature and time per cut depending on the cut-off wheel diameter, the compression force exerted by the cut-off wheel on the workpiece and the workpiece rotational frequency. This implies that the optimum values of the investigated response variables will be obtained at different combinations of values of control factors (d_s, F and n_w). Hence, the optimization of the elastic abrasive cutting process by one parameter is irrelevant. Multi-objective optimization will provide much more information so as to make a justified decision on the selection of optimum cutting conditions.

The common multi-objective optimization methods can be classified into three main groups [36] to [38]. The first group includes methods that use one of the response variables as an objective function and the rest of the response variables are considered to be limits. The major disadvantage of those methods is that they do not apply the main idea of multi-objective optimization: specifically, all response variables to be considered simultaneously. The proposed procedures from this category would result in unreal solutions, especially when there are conflicting objectives. In addition, in many cases, it is difficult to choose one of the response variables as an objective function. When applying the methods from the second group, a domain where different response variables meet specific requirements occurs. This approach is effective in the case of a small number of control factors (2 or 3) and response variables (up to three). The third group comprises methods that combine a set of response variables in a generalized objective function defined as a utility function, desirability function, loss function, or proportion of conformance. In those cases, the optimization problem is solved as a single-objective one.

To define the optimum elastic abrasive cutting conditions, the generalized utility function method was chosen [36], [37] and [39]. It is based on the idea that the quality of a product or process with a set of response variables is unacceptable if one of the response variables is outside the utility limits. This method defines the result as a combination of response variables and chooses a set of factors where the result is a maximum value. The generalized utility function has many advantages compared to other combining methods, mainly due to its flexibility since it makes it possible to maximize some output quantities and minimize others simultaneously.

The generalized utility function could be defined as a geometric-mean value $\Phi_{G,h}$ or an arithmetic-mean value $\Phi_{A,h}$ of the partial utility functions $\eta_{g,h}$ obtained by transforming the studied and modelled response variables of the elastic abrasive cutting process $y_{g,h}$ (Table 4) into dimensionless quantities [37] and [39]. To solve the specific optimization problem, the generalized geometric-mean utility function was chosen as an optimization parameter since if one of the response variables of the elastic abrasive cutting process does not meet the requirements of utility limits, then $\Phi_{G,h}=0$. In this case, the arithmetic generalized utility function is $\Phi_{A,h}\neq 0$ and could have a maximum value but the elastic abrasive cutting conditions under which this value of $\Phi_{A,h}$ has been obtained are not optimum.

The generalized geometric-mean utility function is a complex indicator, which is determined in conformity with the dependency [37] and [39]:

$$\Phi_{G,h}=\sqrt{\prod_{g=1}^{5}\eta_{g,h}}=\sqrt[5]{\prod_{g=1}^{5}\frac{k_g\left(y_{g,h}-y_{g(u)}\right)}{\Delta y_g}}, \qquad (2)$$

where k_g is utility coefficient ($k_g=+1$), when the increase of the studied response variable $y_{g,h}$ is useful; ($k_g=-1$), when the decrease of $y_{g,h}$ is useful); $y_{g,u}$ is the most useless result of the response variable $y_{g,h}$, obtained within the limits of the permissible space; $\Delta y_g=y_{g\max}-y_{g\min}$; $y_{g\max}$ and $y_{g\min}$ is utility limits (maximum and minimum value of $y_{g,h}$).

The solution of the optimization problem is reduced to defining the combination of the control factors of the elastic abrasive cutting process; cut-off wheel diameter d_s, compression force F and workpiece rotational frequency n_w, where the generalized geometric-mean utility function has a maximum. The problem is solved for each material being machined (C45 and 42Cr4 steels).

2.2 Modelling of Generalized Utility Function

To solve the optimization problem, mathematical models for defining the generalized geometric-mean utility function depending on the control factors of the elastic abrasive cutting process were built. The general form of the models, assumed on the basis of the performed analysis of the influence of elastic abrasive cutting conditions on its response variables: cut off wheel wear δ_h, cut-off wheel temperature $T_{s,h}$, workpiece temperature $T_{w,h}$, cut piece temperature $T_{d,h}$, and time per cut $t_{c,h}$, is:

$$\Phi_{G,h}=A_0+\sum_{i=1}^{3}A_iX_i+\sum_{i=1}^{3}A_{ii}X_i^2+ \\ +\sum\sum_{i<j}A_{ij}X_iX_j+A_{123}X_1X_2X_3. \qquad (3)$$

The models in Eq. (3) under the conditions of elastic abrasive cutting of C45 and 42Cr4 were built on the basis of the results from the experiments carried out according to an optimum design involving the following number of trials $N=2^n+2n+1=15$ ($n=3$ is the number of control factors) in Table 5. With each trial, the generalized geometric-mean utility function was determined in compliance with dependency in Eq. (2), as the values of the most useless result and the utility limits of the response variables of the elastic abrasive cutting process were determined in compliance with the following equations:

$$\delta_{(u)}=(\delta_h)_{\max};\ T_{s(u)}=(T_{s,h})_{\max};\ T_{w(u)}=(T_{w,h})_{\max};$$
$$T_{d(u)}=(T_{d,h})_{\max};\ t_{c(u)}=(T_{c,h})_{\min};$$

$$\Delta\delta=(\delta_h)_{\max}-(\delta_h)_{\min};\ \Delta T_s=(T_{s,h})_{\max}-(T_{s,h})_{\min};$$
$$\Delta T_w=(T_{w,h})_{\max}-(T_{w,h})_{\min};\ \Delta T_d=(T_{d,h})_{\max}-(T_{d,h})_{\min};$$
$$\Delta t_c=(t_{c,h})_{\max}-(t_{c,h})_{\min};$$

where $(\delta_h)_{\min}$, $(\delta_h)_{\max}$, $(T_{s,h})_{\min}$, $(T_{s,h})_{\max}$, $(T_{w,h})_{\min}$, $(T_{w,h})_{\max}$, $(T_{d,h})_{\min}$, $(T_{d,h})_{\max}$, $(T_{c,h})_{\min}$, $(T_{c,h})_{\max}$ are, respectively, the minimum and maximum values of cut off wheel wear, cut-off wheel temperature, workpiece temperature, cut piece temperature and time per cut, calculated by using the regression models in Eq. (1) (Table 4).

The models in Eq. (3), Table 6, were built on the basis of the defined values of the generalized geometric-mean utility function (Table 5) by applying the regression analysis method and QstatLab software [34]. They include only the significant regression coefficients defined according to the condition $\hat{t}>t_{h(\alpha/2,v)}$, where $\hat{t}$ and $t_{h(\alpha/2,v)}$ are respectively the calculated values of Student's t-criterion for each coefficient of the regression equations and the tabular value of Student's t-criterion ($\alpha=0.05$) is the significance level; $v=N-k$ is the number of degrees of freedom; k is the number of coefficients in the model). The tabular values of Student's t-criterion for each model are: $t_{1(0.025,6)}=2.447$ and $t_{2(0.025,9)}=2.262$. The constructed models are relevant since the condition $\widehat{F}_h>F_{h(\alpha,v_1,v_2)}$ has been met with a confidence level of 95 %. They extremely accurately describe the dependencies between the studied response variables and control factors. The calculated $\widehat{F}_h$ and tabular $F_{h(\alpha,v_1,v_2)}$ values of Fisher criterion ($\widehat{F}_h=0.05$; $v_1=k-1$ and $v_2=N-k$ are degrees of freedom), as well as the values of the determination coefficient $\widehat{R}_h^2$ for each regression model in Eq. (3) are shown in Table 6.

The effect of cutting conditions on the generalized utility function according to the created theoretical and experimental models (Table 6) is graphically presented in Figs. 5 and 6.

Table 5. *Design of the experiment and generalized utility functions during elastic abrasive cutting of C45 and 42Cr4 steels*

Control factors			Generalized utility function	
d_s [mm]	F [daN]	n_w [min^{-1}]	$\Phi_{G,1}$	$\Phi_{G,2}$
120	1	22	0.604	0.497
180	1	22	0.437	0.000
120	3	22	0.486	0.365
180	3	22	0.474	0.000
120	1	160	0.484	0.000
180	1	160	0.563	0.400
120	3	160	0.335	0.000
180	3	160	0.400	0.215
120	2	91	0.593	0.473
180	2	91	0.498	0.285
150	1	91	0.608	0.478
150	3	91	0.475	0.323
150	2	22	0.480	0.311
150	2	160	0.541	0.395
150	2	91	0.574	0.447

To determine the impact rate of control factors on the generalized utility function, ANOVA was

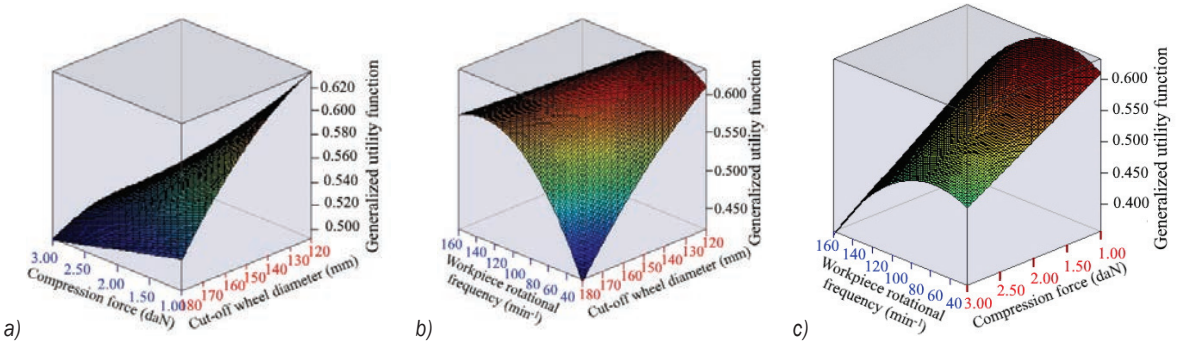

Fig. 5. *Generalized utility function in elastic abrasive cutting of C45 steel; a) n_w = 63.7 min–1 , b) F = 1 daN; and c) d_s = 120 mm*

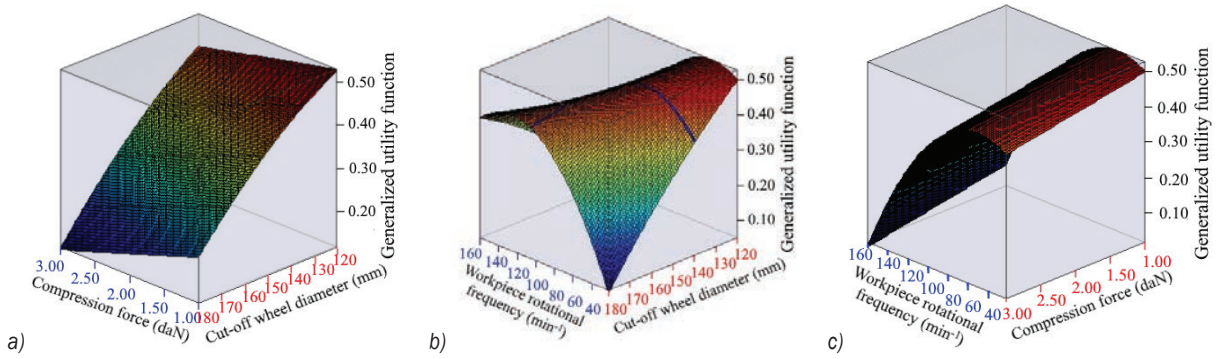

Fig. 6. *Generalized utility function in elastic abrasive cutting of 42Cr4 steel; a) n_w = 49.9 min^{-1}, b) F = 1 daN, c) d_s = 120 mm*

conducted. QstatLab software [34] was used, and the interaction between the factors was considered.

It has been established that the elastic abrasive cutting conditions have different effects, in terms of nature and level, on the generalized geometric-mean utility function, depending on the type of material being machined. In the elastic abrasive cutting of C45 steels, the highest effect is exerted by the compression force. As F decreases, the generalized utility function value $\Phi_{G,1}$ increases. The effect of the compression force increases as the workpiece rotational frequency n_w increases and the cut-off wheel diameter d_s decreases. In the elastic abrasive cutting of 42Cr4 steels, the highest effect on the generalized utility function $\Phi_{G,1}$ is exerted by the workpiece rotational frequency and the relationship $\Phi_{G,2}=f(n_w)$ has a maximum whose value depends on the cut-off wheel diameter and compression force. The effect of n_w on $\Phi_{G,2}$ increases as the cut-off wheel diameter decreases and the compression force increases. It is highest when cutting with abrasive wheels of diameter d_s = 120 mm and compression force F = 3 daN.

2.3 Definition of Optimum Elastic Abrasive Cutting Conditions

The optimization problem was solved upon elastic abrasive cutting of C45 and 42Cr4 steels by using a genetic algorithm and QStatLab software [34]. The defined optimum conditions (cut-off wheel diameter d_s, compression force F and workpiece rotational frequency n_w), where the generalized utility function $\Phi_{G,h}$ has a maximum, are presented in Table 7 and Figs. 5 and 6. The elastic abrasive cutting under these conditions ensures the best possible match between the rate of cut off wheel wear, time per cut, cut piece temperature, cut-off wheel temperature and workpiece temperature, respectively, in the elastic abrasive cutting of C45 steels: δ_1 = 1.532 mm, $T_{s,1}$ = 1.527 °C, $T_{w,1}$ = 975 °C, $T_{d,1}$=177.8 °C and $t_{c,1}$ = 8.21 s; in the elastic abrasive cutting of 42Cr4 steels: δ_2 = 1.524 mm, $T_{s,2}$ = 161.2 °C, $T_{w,2}$ = 977.4 °C, $T_{d,2}$ = 212.6 °C, and $t_{c,2}$ = 12.7 s.

Under the predicted optimum elastic abrasive cutting conditions (cut-off wheel diameter d_s = 120 mm, compression force F = 1 daN; workpiece rotational frequency n_w = 63.7 min^{-1} and n_w = 49.9 min^{-1}, respectively for C45 steels and 42Cr4 steels), confirmation run experiments were performed, where cut off wheel wear, cut-off wheel temperature, workpiece temperature, cut piece temperature and time per cut were determined. The experimental values of the elastic abrasive cutting process response variables are presented in Table 7. They are determined as an arithmetical mean of the four observations done for each of them. A comparison between the experimental

Table 6. *Theoretical and experimental models of the generalized utility function and statistical characteristics of the models*

Steel type	Models	Fisher criterion		Determination coefficient
		Calculated	Tabular	
C45	$\Phi_{G,1}=0.899-0.25F-0.003n_w-1.791.10^{-5}d_s^2-1.318.10^{-5}n_w^2+$ $+0.001Fn_w+0.002d_sF+4.08.10^{-5}d_sn_w-1.058.10^{-5}d_sFn_w$	5.425	4.147	0.717
42Cr4	$\Phi_{G,2}=0.917-0.007n_w-3.06.10^{-5}d_s^2-3.61.10^{-5}n_w^2+$ $+9.107.10^{-5}d_sn_w-3.057.10^{-4}d_sF$	12.553	3.482	0.804

Table 7. *Optimum elastic abrasive cutting conditions*

Steel type	Optimal conditions of elastic abrasive cutting			Response variables										Generalized utility function, $\Phi_{G,h}$
				Cut off wheel wear, δ_h [mm]		Temperature of the cut off wheel, $T_{s,h}$ [°C]		Temperature of the workpiece, $T_{w,h}$ [°C]		Temperature of the cut piece, $T_{d,h}$ [°C]		Time per cut, $t_{c,h}$ [s]		
	d_s [mm]	F [daN]	n_w [min^{-1}]	PV	EV	PV	EV	PV	EV	PV	EV	PV	EV	
C45	120	1	63.7	1.532	1.578	152.7	155	975	960	177.8	183	8.21	8.33	0.634
42Cr4	120	1	49.9	1.524	1.561	161.2	167	977.4	965	202.6	212	12.7	12.95	0.528

EV = experimental value; PV = predicted value

and the predicted, according to the models, Eq. (1), Table 4, values of the elastic abrasive cutting process response variables (Table 7) shows that error percentage is: 2.37 % to 2.92 % for cut off wheel wear; 1.48 % to 3.47 % for cut off wheel temperature; 1.28 % to 1.56 % for workpiece temperature; 2.84 % to 4.43 % for cut piece temperature; 1.44 % to 1.93 % for time per cut. These results prove that the recommended elastic abrasive cutting conditions are optimum and correct.

3 CONCLUSIONS

This paper proposes a new approach for optimizing the elastic abrasive cutting process, which takes into consideration the specifics of its particular implementation. The generalized geometric-mean utility function has been chosen as an optimization factor. It appears to be a complex indicator characterizing the technological and economic parameters of elastic abrasive cutting.

The proposed optimization approach has been applied to determine the optimum conditions of elastic abrasive cutting of C45 and 42Cr4 steels. The following results have been achieved:

(1) To determine the generalized utility function, theoretical and experimental models reflecting the complex influence of the control factors of the process (cut-off wheel diameter d_s, compression force F and workpiece rotational frequency n_w) have been developed. The models are based on the findings of complex studies and modelling of the parameters of the elastic abrasive cutting process (cut off wheel wear, time per cut, cut piece temperature, cut-off wheel temperature, and workpiece temperature) depending on the conditions of its implementation.

(2) By applying the generalized utility function and genetic algorithm, the optimum conditions for implementing the process have been determined as follows: cut-off wheel diameter d_s=120 mm; compression force F=1 daN; workpiece rotational frequency n_w = 63.7 min^{-1} and n_w = 49.9 min^{-1}, respectively for C45 and 42Cr4 steels. The authenticity of the determined optimum conditions has been proven by an experimental study of the response variables of the elastic abrasive cutting process. It has been established that they ensure the best possible match between the rate of cut off wheel wear ($\delta \leq 1.58$ mm), the cut off wheel temperature ($T_s \leq 167$ °C), the workpiece temperature ($T_w \leq 965$ °C), the cut piece temperature ($T_d \leq 212$ °C) and the time per cut ($t_c \leq 12.95$ s).

The results obtained in applying the new optimization approach provide possibilities for enhancing efficiency and controlling the elastic abrasive cutting process by choosing optimum conditions in accordance with the specifics and implementation of the particular abrasive cutting process. They also confirm the key role of the workpiece rotational frequency, compression force and cut-off wheel diameter for the cut off wheel lifetime, the productivity of the elastic abrasive cutting process and the temperature distribution within the tool, workpiece and cut piece. Taking into account the high productivity and low cost of the elastic abrasive process, the proposed multipurpose optimization approach and the obtained theoretical-experimental results, presented in this paper, could be used in every enterprise specialized in machine building.

4 ACKNOWLEDGEMENTS

This work was supported by the European Regional Development Fund within the OP "Science and Education for Smart Growth 2014 - 2020", Project CoC "Smart Mechatronic, Eco- and Energy-saving Systems and Technologies", No BG05M2OP001-1.002-0023 and the Research fund of the Technical University of Gabrovo (Project no 2008 M).

5 REFERENCES

[1] Ganev, G. (2013). *Elastic Abrasive Cutting of Rotational Workpieces in Mechanical Engineering*. PhD Thesis, Technical University of Gabrovo, Gabrovo. (in Bulgarian)

[2] Neugebauer, R., Hess, K.-U., Gleich, S., Pop, s. (2005). Reducing tool wear in abrasive cutting. *International Journal of Machine Tools and Manufacture*, vol. 45, no. 10, p. 1120-1123, **DOI:10.1016/j.ijmachtools.2005.01 .002**.

[3] Putz, M., Cardone, M., Dix, M. (2017). Cutoff grinding of hardened steel wires - modelling of heat distribution. *Procedia CIRP*, vol. 58, p. 67-72, **DOI:10.1016/j.procir.2017.03.198**.

[4] Nenkov, N., Aleksandrova, I., Ganev, G. (1999). Methods of abrasive cutting of workpieces. *Mashinostroene*, no. 5-6, p. 38-40. (in Bulgarian)

[5] Kaczmarek, J. (2011). Using a thermovision method for measuring temperatures of a workpiece during abrasive cutoff operation. *Advance in Manufacturing Science and Technology*, vol. 35, no. 4, p. 85-95.

[6] Sahu, P., Sagar, R. (2006). Development of abrasive cutoff wheel having side grooves. *The International Journal of Advanced Manufacturing Technology*, vol. 31, p. 37-40, **DOI:10.1007/s00170-005-0138-2**.

[7] Levchenko, E., Pokintelitsa, N. (2017). Investigation of thermal processes in abrasive pipe samplin. *MATEC Web of Conferences*, vol. 129, **DOI:10.1051/matecconf/201712901082**.

[8] Lopes, J.C., Ribeiro, F.S.F., Javaroni, R.L., Garcia, M.V., Ventura, C.E.H., Scalon, V.L., de Angelo Sanchez, L.E., de Mello, H.J., Aguiar, P.R., Bianchi, E.C. (2020). Mechanical and thermal effects of abrasive cutoff applied in low and medium carbon steels using aluminum oxide cutting disc. *The International Journal of Advanced Manufacturing Technology*, vol. 109, p. 1319-1331, **DOI:10.1007/s00170-020-05753-5**.

[9] Luo, S.Y., Tsai, Y.Y., Chen, C.H. (2006). Studies on cutoff grinding of BK7 optical glass using thin diamond wheels. *Journal of Materials Processing Technology*, vol. 173, no. 3, p. 321-329, **DOI:10.1016/j.jmatprotec. 2005.11.036**.

[10] Ortega, N., Martynenko, V., Perez, D., Krahmer, D.M., López de Lacalle, L.N., Ukar, E. (2020). Abrasive disc performance in dry-cutting of medium-carbon steel. *Metals*, vol. 10, no. 4, art. ID 538, **DOI:10.3390/met10040538**.

[11] Riga, A., Scott, C. (2001). Failure analysis of an abrasive cut-off wheel. *Engineering Failure Analysis*, vol. 8, no. 3, p. 237-243, **DOI:10.1016/S1350-6307(00)00014-5**.

[12] Yoshida, T., Nagasaka, K., Kita, Y., Hashimoto, F. (1986). Identification of a grinding wheel wear equation of the abrasive cutoff by the modified GMDH. *International Journal of Machine Tool Design and Research*, vol. 26, no. 3, p. 283-292, **DOI:10.1016/0020-7357(86)90006-5**.

[13] Ojolo, S., Orisaleye, J., Adelaja, A. (2010). Development of a high speed abrasive cutting machine. *Journal of Engineering Research*, vol. 15, p. 1-8.

[14] Kaczmarek, J. (2008) The effect of abrasive cutting on the temperature of grinding wheel and its relative efficiency. *Archives of Civil and Mechanical Engineering*, vol. 8, no. 2, p. 81-91, **DOI:10.1016/S1644-9665(12)60195-2**.

[15] Ni, J., Yang, Y., Wu, C. (2019). Assessment of water-based fluids with additives in grinding disc cutting process. *Journal of Cleaner Production*, vol. 212, p. 593-601, **DOI:10.1016/j.jclepro.2018. 12.066**.

[16] Yamasaka, M., Fujisawa, M., Oku, T., Masuda, M., Okamura, K. (1990). improvement of straightness in precision cut-off grinding using thin diamond wheels. *CIRP Annals*, vol. 39, no. 1, p. 333-336, **DOI:10.1016/S0007-8506(07)61066-X**.

[17] Braz, C.O., Ventura, C.E.H., De Oliveira, M.C.B.,Antonialli, A.Í.S., Ishikawa, T. (2019). Investigating the application of customized abrasive cut-off wheels with respect to tool wear and subsurface integrity in metallographic cutting of pure titanium. *Metallography, Microstructure, and Analysis*, vol. 8, p. 826-832, **DOI:10.1007/s13632-019-00587-4**.

[18] Wang, Z., Li, Y., Yu, T., Zhao, J., Wen, P.H. (2018). Prediction of 3D grinding temperature field based on meshless method considering infinite element. *The International Journal of Advanced Manufacturing Technology*, vol. 100, p. 3067-3084, **DOI:10.1007/s00170-018-2801-4**.

[19] Eshghy, S. (1968). Thermal Aspects of the Abrasive Cut off Operation. Part 2 - Partition Functions and Optimum Cut off. *Journal of Engineering for Industry*, vol. 90, no. 2, p. 360-364, **DOI:10.1115/1.3604641**.

[20] Hou, H., Komanduri, R. (2004). On the mechanics of the grinding process, Part III - thermal analysis of the abrasive cutoff operation. *International Journal of Machine Tools and Manufacture*, vol. 44, no. 2-3, p. 271-289, **DOI:10.1016/j.ijmachtools.2003.09.009**.

[21] Putz, M., Cardone, M., Dix, M., Wertheim, R. (2019). Analysis of workpiece thermal behaviour in cutoff grinding of high-strength steel bars to control quality and efficiency. *CIRP Annals*, vol. 68, no. 1, p. 325-328, **DOI:10.1016/j.cirp.2019.04.023**.

[22] Malkin, S., Guo, C. (2007). Thermal analysis of grinding. *CIRP Annals*, vol. 56, no. 2, p. 760-782, **DOI:10.1016/j.cirp.2007.10.005**.

[23] Stoynova, A., Aleksandrova, I., Aleksandrov, A., Ganev, G. (2018). Infrared thermography for elastic abrasive cutting process monitoring. *MATEC Web of Conferences*, vol. 210, **DOI:10.1051/matecconf/201821002018**.

[24] Stoynova, A., Aleksandrova, I., Aleksandrov, A., Goranov, G. (2019). Non-contact measurement and monitoring of cutoff wheel wear. *28th International Scientific Conference Electronics*, **DOI:10.1109/ET.2019.8878321**.

[25] Ortega, N., Bravo, H., Pombo, I., Sánchez, J., Vidal, G. (2015). Thermal analysis of creep feed grinding. *Procedia Engineering*, vol. 132, p. 1061-1068, **DOI:10.1016/j.proeng.2015.12.596**.

[26] Nagasaka, K., Yoshida, T., Kita, Y., Hashimoto, F. (1987). Optimum combination of operating parameters in abrasive cutoff. *International Journal of Machine Tools and Manufacture*, vol. 27, no. 2, p. 167-179, **DOI:10.1016/S0890-6955(87)80048-2**.

[27] Shaw, M. (1975). The rating of abrasive cut-off wheels. *Journal of Engineering for Industry*, vol. 97, no. 1, p. 138-146, **DOI:10.1115/1.3438526**.

[28] Vologin, K. (2002). *Selection of rational conditions for cutting workpieces of difficult to machine material with abrasive*

wheels. PhD Thesis, Moscow State University of Technology Stankin, Moscow. (in Russian)

[29] Aleksandrova, I., Ganev, G., Hristov, H. (2019). Performance of cutoff wheels during elastic abrasive cutting of rotating workpieces. *Tehnički vjesnik - Technical Gazette*, vol. 26, no. 3, p. 577-583, **DOI:10.17559/TV-20151223184850**.

[30] Aleksandrova, I., Ganev, G., Hristov, H. (2016). Cutting forces and power during elastic abrasive cutting of rotating workpieces. *Tehnički vjesnik - Technical Gazette*, vol. 23, no. 2, p. 343-348, **DOI:10.17559/TV-20131108115506**.

[31] Catalogue of the Abrasive Tools Factory - Berkovitsa (2020). from *https://zai-bg.com/wp-content/uploads/2020/01/ZAI-2020.pdf*, accessed on 2021-10-16.

[32] Steel and Cast Iron Standards EN 10277 (2008). Steel grades/numbers, from *http://www.steelnumber.com/en/standard_steel_eu.php?gost_number=10277*, accessed on 2021-10-16.

[33] Jamuła, B. (2021). Temperature measurement analysis in the cutting zone during surface grinding. *Journal of Measurements in Engineering*, vol. 9, no. 2, p. 106-116, **DOI:10.21595/jme.2021.21894**.

[34] Vuchkov, I.N., Vuchkov, I.I. (2009). *Statistical methods of quality control, robust engineering, planning, modeling and optimization*, QStatLab, v 5.3. (in Bulgarian)

[35] Aleksandrova, I., Hristov, H., Ganev, G. (2011). Dynamic and technological characteristics of the process elastic abrasive cutting of rotating workpieces. *Journal of the Technical University Sofia, Branch Plovdiv: Fundamental Sciences and Applications*, vol. 16, p. 123-128.

[36] Mukherjee, I., Ray, P. (2006). A review of optimization techniques in metal cutting processes. *Computers & Industrial Engineering*, vol. 50, no. 1-2, p. 15-34, **DOI:10.1016/j.cie.2005.10.001**.

[37] Stoyanov, S. (1993). *Optimization of Manufacturing Processes*. Tehnika, Sofia.

[38] Yusup, N., Zain, A., Hashim, S. (2012). Evolutionary techniques in optimizing machining parameters: Review and recent applications (2007-2011). *Expert Systems with Applications*, vol. 39, no. 10, p. 9909-9927, **DOI:10.1016/j.eswa.2012.02.109**.

[39] Aleksandrov, A., Aleksandrova, I. (2012). *Theory of Experiment*. Ex-Press. Gabrovo. (in Bulgarian)

Strojniški vestnik - Journal of Mechanical Engineering 67(2021)12, 649-665

DOI:10.5545/sv-jme.2021.7322 Original Scientific Paper
Received for review: 2021-07-12
Received revised form: 2021-09-19
Accepted for publication: 2021-10-07

Investigation of Cutting Performance of a Circular Saw Blade Based on ANSYS/LS-DYNA

Zhiwen Wang[1] – Qingliang Zeng[1,3*] – Zhenguo Lu[2] – Lirong Wan[1] – Xin Zhang[1] – Zhihai Liu[2]

[1] Shandong University of Science and Technology, College of Mechanical and Electronic Engineering, China
[2] Shandong University of Science and Technology, College of Transportation, China
[3] Shandong Normal University, College of Information Science and Engineering, China

The circular saw blade is widely applied in rock processing; its cutting performance significantly impacts rock processing. Therefore, the numerical simulation model of rock cutting with the flexible circular saw blade has been established to investigate the effects of cutting parameters on the stress and cutting force of circular saw blade, and the damage and stress of rock in the circular saw blade cutting into rock vertically at constant feed speed and rotation speed. The research results indicate that the stress of the saw blade and rock rises with the increase of feed speed and rotation speed of the saw blade. Furthermore, the rock damage and the cutting force of the circular saw blade increase with the increasing feed speed and decrease with increasing rotation speed. The circular saw blade cutting force, vertical force, and horizontal force increase with the rising distance between the double circular saw blade. However, the axial force decreases. The research results of cutting hard rock with the flexible circular saw blade can aid in the optimization of cutting parameters and improve cutting efficiency.
Keywords: circular saw blade, rock damage, cutting force, stress

Highlights

- *The circular saw blade cutting rock numerical simulation is established based on ANSYS/LS-DYNA.*
- *The numerical simulation and uniaxial compression test results are compared to verify the numerical simulation model and improve the accuracy.*
- *The influence of the circular saw blade cutting parameters on cutting performance has been studied.*
- *The results indicate that the stress of the saw blade and rock rises with the increasing feed speed and rotation speed.*

0 INTRODUCTION

The circular saw blade has good cutting performance and is widely used for ceramics, marble, glass, and other materials with high hardness and brittleness. Many scholars have researched the circular saw blade and studied the influence of structural parameters, cutting parameters, and rock properties on the specific cutting energy consumption, wear of saw blade, and cutting force, and explored the circular saw blade noise through modal analysis.

Many scholars have researched the cutting force, and the specific energy consumption of circular saw blades and the effect of cutting parameters and rock properties on the circular saw blade cutting performance. Aydin et al. [1] to [3] studied the effect of the operating parameters and the rock properties on energy consumption with the experiments. Goktan et al. [4] studied the effect of Knoop micro-hardness on the sawblade specific cutting energy. Li et al. [5] researched the tool wear effect on cutting energy. Yilmaz et al. [6] investigated the material remove rate influence on specific cutting energy. Ataei et al. [7] applied the sawability index to evaluate the rock-sawing energy consumption. Atici et al. [8] studied the prediction model of the cutting specific energy and the drilling with the regression analysis method. Aslantas et al. [9] researched the axial force influence on cutting performance. Ersoy et al. [10] investigated the cutting parameters effect on cutting performance. Tumac et al. [11] and [12] studied the rock properties influence on the saw blade cutting performance. Mikaeil et al. [13] researched the rock physical and mechanical properties for optimizing machine application. Yilmaz et al. [14] studied the active power consumption, force ratio, specific wear rate, and noise emission of the sandwich core saw blade and traditional saw blade. Tonshoff et al. [15] studied the mechanism of the interaction between diamond particles and rock. Xu et al. [16] investigated the influence of cutting speed, cutting depth, and feed rate on cutting force. Karakurt et al. [17] studied the cutting force of the saw blade on granite in cutting granite. Buyuksagis and Goktan [18] established the empirical equation of specific cutting energy consumption of different natural stones based on the diamond saw blade cutting experiment. Jiang et al. [19] came up with a new gangue distribution function to simulate the gangue distribution condition and studied the cutting force and specific cutting energy with different gangue. Agarwal and Rao [20]

*Corr. Author's Address: Shandong University of Science and Technology, Qingdao, China, qlzeng@sdust.edu.cn

discussed the mechanism of damage and material removal of SiC cutting. Burek et al. [21] analysed the cutting edge-shape cutting-force components model, and the study proved that serrated cutting edges adopting end mills had lower cutting force components.

Lu et al. [22] explored rock-cutting performance with a cutting saw blade with numerical simulation and experimental methods. Zeng et al. [23] studied the distance between the sawblade and free surface influence on rock cutting performance. Hoang et al. [24] researched the milling conditions effect on surface roughness with the test and analyzed the cutting conditions impact on cutting force and the surface amplitude. Liu et al. [25] have studied the milling cutting wear and geometric structure parameters on the machined surface integrity and cutting force.

Fermando et al. [26] established the mathematical cutting force prediction model of rotary ultrasonic cutting rock, and predicted the relationship between input variables and cutting force. Zuperl et al. [27] presented a neuro-mechanistic model to accurately predict the multidirectional layer material helical end milling cutting force. Peng and Fang [28] proposed a resultant force-positioning model based on the tangential force distribution on the saw blade, which was verified with experiments. Liu et al. [29] studied the rock damage on rock fracture and cutting performance with the discrete element method.

Many scholars have researched the saw blade and rock fracture mechanism; however, there is less investigation on circular sawblade cutting rock as a flexible body based on numerical simulation of the rock cutting process. Furthermore, in the circular saw blade cutting rock process in the numerical simulation model, the rock breaking effect is ideal. The influence of lubrication during circular saw blade cutting is not considered. The hard rock cutting studied in the paper is represented by the granite, which will be extended to other hard rocks in the following research. The cutting parameters of the flexible circular saw blade influence on rock damage and rock stress and circular saw blade stress and the cutting force is investigated with the ANSYS/LS-DYNA to establish the flexible circular saw blade cutting rock numerical simulation model. The circular saw blade feed speeds are set as 0.10 m/s, 0.15 m/s, 0.20 m/s, 0.25 m/s, and 0.30 m/s, and the rotation speeds are defined as 1000 r/min, 1500 r/min, 2000 r/min, 2500 r/min, and 3000 r/min. To optimize the circular saw blade cutting parameters and improve cutting efficiency, the effects of saw blade feed speed, rotation speed, and other parameters on the circular saw blade stress and cutting force explored the effect of rock damage and breakage.

1 THE MODEL OF ROCK DAMAGE

The inhomogeneous propagation of cracks causes the anisotropy of derived materials. The anisotropic behaviour needs to be considered to establish the constitutive damage relation with the action of external load. Consider the normal vector discreteness, and each crack family is given a damage variable to describe the crack state. The damage variables of all fracture families are defined as a set, expressed as Eq. (1), d_i is the internal damage variable of the i^{th} crack.

$$D = \{d_1, d_2, ..., d_N\}. \tag{1}$$

To simplify the equation, it should first be considered that the rock matrix contains a single group of fractures. In general, assuming that the normal vector of the group fractures is **n**, and the $d = d(\mathbf{n})$, used to represent the fracture distribution density, that is, the damage variable. It is necessary to determine the free energy expression of the fracture matrix system to establish a damage mechanics model based on thermodynamics. When only the energy dissipation caused by crack propagation is considered, the strain-free energy of the system is the function of the macroscopic variable ε and the damage variable d, as plotted in Eq. (2):

$$\psi(\varepsilon, d) = \frac{1}{2}\varepsilon : C^{\text{hom}}(d) : \varepsilon, \tag{2}$$

among that, $C^{\text{hom}}(d)$ is the effective elastic tensor of the damaged material.

The state variable, called thermodynamics associated with internal variables, is the energy dissipation‘s driving force, which can be obtained by deriving the free energy from the internal variables. First, establish the macro stress-strain relation as shown in Eq. (3).

$$\sigma = \frac{\partial \psi}{\partial d} = C^{\text{hom}} : \varepsilon. \tag{3}$$

The thermal force related to the damage variable is obtained, that is, the damage drive force.

$$F_d = -\frac{\partial \psi}{\partial d} = -\frac{1}{2}\varepsilon : \frac{\partial C^{\text{hom}}}{\partial d} : \varepsilon. \tag{4}$$

The combination of micromechanics and thermodynamics based on macroscopic expression is an effective method of damaging fractured materials. On the one hand, the effective mechanical

properties of the materials are determined by means of micromechanics and the constitutive equation and internal variable evolution criterion are established by fully considering the mechanical mechanism of material damage and failure. On the other hand, based on the irreversible thermodynamics theory of internal variables, the thermodynamic constraints of the constitutive equation and the development process of the standardized numerical program are provided, which can consider the engineering practicability of the constitutive model. According to the second law of thermodynamics, the energy dissipation caused by fracture propagation is nonnegative, and it satisfies Eq. (5).

$$D_e = F_d \dot{d}. \tag{5}$$

In the framework of the thermodynamics, the damage criterion based on the strain energy release rate is usually adopted, shown as Eq. (6)

$$g(F_d, d) = F_d - R(d) \le 0, \tag{6}$$

where $R(d)$ is the resistance function of damage evolution (crack propagation), shown in the damage criterion Eq. (7). The loading conditions are as follow:

$$\begin{cases} \dot{d} = 0 & F_d < R(d) \\ \dot{d} > 0 & F_d \ge R(d) \end{cases}. \tag{7}$$

In the analysis of meso-damage mechanics, the need for analytical mathematical expression is considered, and it is usually assumed that the fracture propagation process is similar, meaning that the fracture shape remains coin-shaped and only propagates in the damage injuring plane, so the normal vector of fracture surface does not change.

Assuming that the rock is orthorhombic material, the damage evolution obeys the orthogonalization criterion Eq. (8).

$$\dot{d} = \lambda^d \frac{\partial (F_d, d)}{\partial F_d}, \quad \lambda^d \ge 0, \tag{8}$$

where, λ^d is the damage multiplier.

Similar to the classical plastic theory, the damage evolution equation considering the loading and unloading condition is Eq. (9).

$$\dot{d} = \begin{cases} 0 & g < 0 \text{ or } g = 0 \text{ and } \dot{g} < 0 \\ \lambda^d & g = 0 \quad \text{and} \quad \dot{g} = 0 \end{cases}. \tag{9}$$

The damage multiplier λ^d can be determined by the damage consistency condition ($g = 0$ and $\dot{g} = 0$), as the following Eq. (10).

$$\dot{g} = \frac{\partial g}{\partial \varepsilon} : \dot{\varepsilon} + \frac{\partial g}{\partial d} \dot{d}. \tag{10}$$

In addition, the stress-strain relationship in the form of rate can be established based on the damage evolution criterion. Firstly, the macroscopic stress-strain relationship is expressed in differential form as the Eq. (11):

$$\dot{\sigma} = \dot{C}^{\text{hom}} : \varepsilon + C^{\text{hom}} : \dot{\varepsilon}. \tag{11}$$

Furthermore, there is the following equation, shown as Eq. (12).

$$C^{\text{hom}} : \varepsilon = \frac{\partial C^{\text{hom}} : \varepsilon}{\partial d}; \dot{d} = -\frac{\partial F_d}{\partial \varepsilon} \lambda^d = -\frac{\partial g}{\partial \varepsilon} \lambda^d, \tag{12}$$

and then obtain Eq. (13).

$$\dot{\sigma} = C^{\tan} : \dot{\varepsilon}, \tag{13}$$

where, $C^{\tan}$ is the tangential elastic tensor of the material, the specific expression as Eq. (14).

$$C^{\tan} = C^{\text{hom}} - \frac{1}{H_d} \frac{\partial g}{\partial \varepsilon} \otimes \frac{\partial g}{\partial \varepsilon}, \tag{14}$$

among them, the damage hardening parameters $H_d = \partial g / \partial d$.

2 NUMERICAL SIMULATION MODEL

The research flow chart of the circular saw blade cutting rock with various feed speeds and vertical feed is shown in Fig. 1.

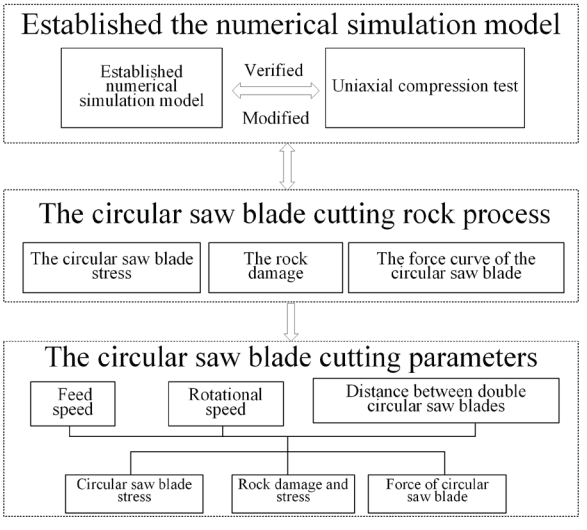

Fig. 1. *The circular saw blade cutting rock research flow chart*

The numerical simulation model is established, and the feasibility of the model is verified using the

uniaxial compression experiment and the numerical simulation with the same parameters. The circular saw the changes in the circular saw blade stress, rock damage, cutting force, vertical force, horizontal force, and the axial force curves with the cutting distance at the second step. The feed speed, rotational speed, and the distance between the double circular saw blades affect the circular saw blade stress and forces, and the rock damage and the stress have been researched in the third step.

2.1 Established Numerical Simulation Model

Establish the circular saw blade cutting a rock geometric model by SolidWorks. The cuboid size is 500 mm × 200 mm × 200 mm; the circular saw blade diameter is 390 mm, and there are 24 segments. Import the geometric model into the ANSYS/LS-DYNA to establish a circular saw blade cutting rock numerical simulation model. Applied the MeshTool to mesh the model with the SOLID164, a hexahedral element with eight nodes, to mesh the rock and circular saw blade. Define the circular saw blade material as PLASTIC_KINEMATIC, and the rock material is defined as RHT; the fundamental rock properties parameters are shown in Table 1. The contact between rock and the circular saw blade is set as SURFACE_TO_SURFACE_ERODING. Add constraints, the full displacement constraints and rotation constraints are added to the bottom surface of the rock, add *X*, *Y* direction displacement constraints to the front and back surface of the rock, and add *X*, *Z* direction constraints to the left and right surfaces of rock. Apply the Z-direction displacement constraint and rotation constraint around *X* and *Y*-axes to the circular saw blade, which is plotted as Fig. 2. To improve the accuracy of numerical simulation, add the no-boundary-reflection condition to the un-cut surface of the rock model to simulate the large rock mass with a small model. Apply the initial rotation around the *Z*-axis clockwise and the initial feed speed along the *X*-axis to the flexible circular saw blade model. The motion load of the circular saw blade is set to rotate around the *X*-axis clockwise and feed along the *X*-axis. The solution time and calculation step are defined as 1 and 0.02 s, respectively. The established numerical simulation model is exported to generate the k file and apply the ANSYS solver to solve the k file. The workstation is used to solve the numerical simulation model, and the calculation core is set to 40 calculation cores.

Table 1. *The rock key properties parameters*

Elastic modulus [GPa]	57.2
Density [kg/m^3]	2670
Compressive strength [MPa]	120
Tensile strength [MPa]	11.8
Poisson's ratio	0.20

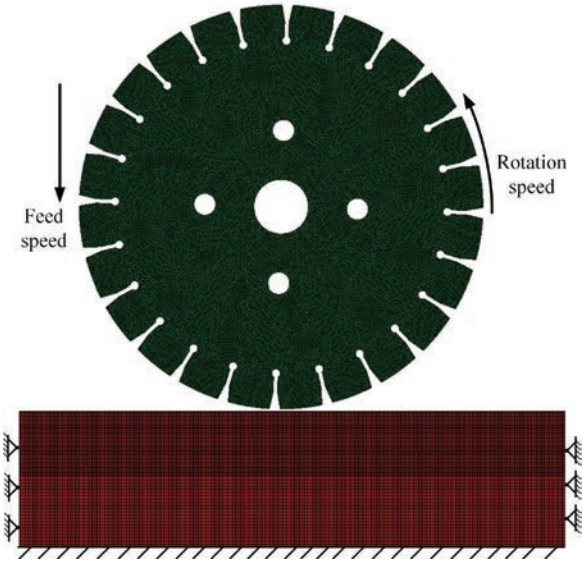

Fig. 2. *The circular saw blades cutting rock numerical simulation model*

2.2 Verified and Modification

The numerical simulation and uniaxial compression test results are compared to verify the numerical simulation model and improve the accuracy. Two 70 mm × 70 mm × 10 mm cylinders are built as the base and the loading body, and a Φ50 mm × 100 mm cylinder is applied to simulate the rock column. Set the base and loading body as rigid, set the rock column as RHT material, and add the total constraints to the bases. The contact type between the rock column and the base and between the rock column and loading body is set as the surface-to-surface erosion contact. The loading body is added with 0.001 m/s uniform motion along the cylinder‘s axis, as shown in Fig. 3a. The uniaxial compression test is carried out on the granite core sample on the uniaxial compression test bench, and the stress-strain curve is measured. The experiment results are shown in Figs. 3b and d, marking the rock sample cracks. The uniaxial compression‘s numerical simulation results are shown in Figs. 3c and d. The rock cracks are consistent with the uniaxial compression numerical simulation results and test results. The stress-strain curves of the test and

numerical simulation are shown in Fig. 3d. The peak stress of the numerical simulation is 108.13 MPa, and the peak stress of the test result is 108.55 MPa. The stress error between the numerical simulation and test results is 0.39 %, which means that the numerical simulation model is accurate and reliable.

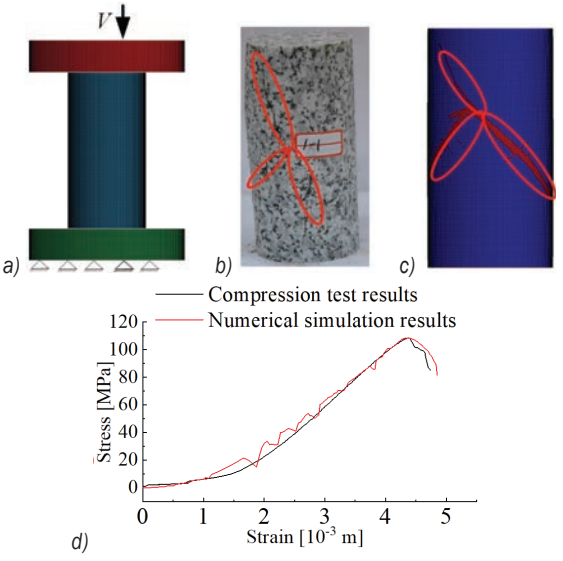

Fig. 3. *The results of uniaxial compression; a) the numerical simulation of the uniaxial compression, b) the result of the uniaxial compression test, c) the result of the uniaxial compression numerical simulation, and d) the stress-strain curve of the numerical simulation and test*

3 RESULTS AND DISCUSSION

3.1 The Circular Saw Blade Cutting into Rock Process

The circular saw blade cutting rock with a rotation speed of 2000 r/min, feed speed of 0.30 m/min cutting into rock vertically is shown in Figs. 4, 5, and 6. When the circular saw blade does not contact the rock, the circular saw blade‘s middle deformation is obvious, and the stress nephogram extends to the direction of the four holes, as shown in Fig. 4a. With the action of the driving force, the circular saw blade matrix strain extends outward along the rotation direction, as plotted in Fig. 4b. In addition, the stress area distribution appears at the bottom of the circular saw blade and the groove of the saw blade matrix in contact with the rock. Stress also occurs in the rock where the circular saw blade contacts it, as shown in Fig. 5a. The stress concentration point appears in the rock that is in contract with the saw blade and expands rapidly under the cutting action of the saw blade, as shown in Fig. 5b. After the saw blade stably cuts the rock, the stress range and peak value in the central area of the saw blade decrease obviously, as shown in Fig. 4c. While the circular saw blade continues to cut into the rock, the circular saw blade segment stress increases obviously. The stress of saw blade segments appears from the saw blade‘s position in contacting the rock. When the saw blade extends the distance backward along the rotation direction, the stress of the saw blade gradually decreases until it disappears. With the increased circular saw blade cutting depth, the circular saw blade‘s contact arc length and the rock increase. Moreover, the saw blade segments‘ stress decreases and appears to need more time while the saw blade cutting out of contact with the rock, and the stress range of the circular saw blade increases significantly.

When the circular saw blade starts running, the stress appears in the saw blade matrix under the action of the large driving force, and the stress gradually decreases in a ring shape from the centre to the outside. When the circular saw blade segment contacts the rock, the stress of the saw blade matrix increases significantly, and the arc extension appears at the outer edge of the stress, as shown in Fig. 4. The rock stress begins to appear when the rock cutting with the circular saw blade, and rock stress appears due to extrusion. Under the rotary shear of the circular saw blade, the rock stress extends along the rotation direction. Moreover, the stress range at the position where the rock contacts the saw blade is smaller than when the saw blade is separated from the rock. While the circular saw blade cuts into rock stably, the circular saw blade matrix stress area and peak value decrease, and the stress cloud area is concentrated. Meanwhile, while the circular saw blade cuts the rock, the rock stress area is mainly distributed along the cutting arc of the circular saw blade. The stress nephogram of the rock in the feed direction of the saw blade is an extensive cutting-away position of the saw blade. Due to the rock fragments on both sides of the sawed joint and the circular saw blade squeezing each other on the rock wall of the saw joint, there is apparent stress appearing on the rock wall. Some rock units do not restore the plastic strain of rock with the removal of the loading, with the shear and tension of the saw blade cause the plastic strain.

In the rock-cutting process with a circular saw blade, when the circular saw blade contacts the rock, the stress concentration point appears on the rock due to the circular saw blade cutting the rock with high cutting speed. The circular saw blade cuts the rock for a certain distance: the contact area between the rock and circular saw blade. For the circular saw blade cutting for a certain distance, at the contact area

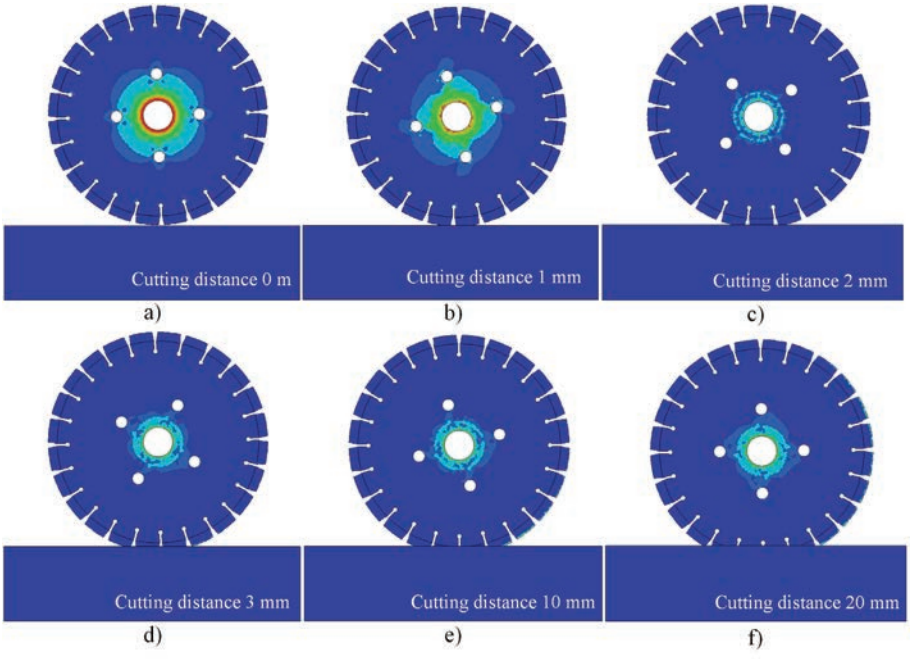

Fig. 4. *The circular saw blade stress nephogram of the circular saw blade cutting rock process*

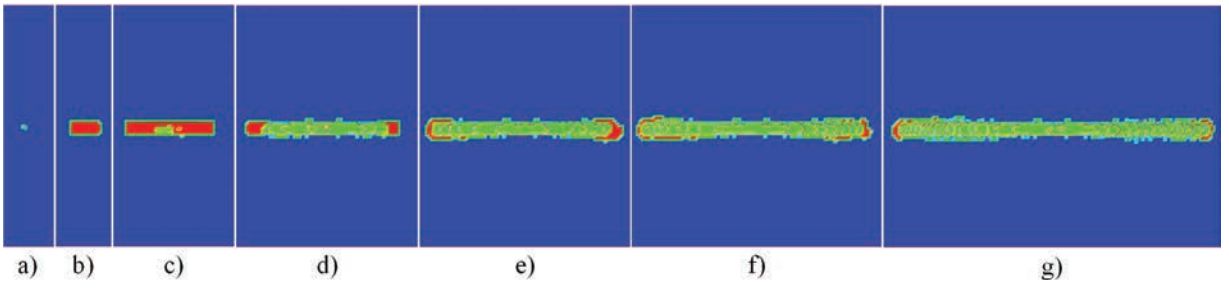

Fig. 5. *The rock damage nephogram of a circular saw blade cutting rock*

between the circular saw blade and rock, a prominent stress area appears and expands. When the cutting depth reaches 0.005 m, the damage value of the rock unit reaches 1 under the action of the circular saw blade. While the circular saw blade continues to cut the rock, the forms a rock saw gap of a certain width and rock walls on both sides of the circular saw blade. The circular saw blade continues to cut the rock, the rock forms a certain saw gap, and the rock walls on both sides of the circular saw blade is randomly broken. When the cutting depth of the circular saw blade is 0.015 m, the damage area at both ends of the saw seam is prominent, but the damage value at both sides of the saw seam is smaller, and the middle section width of the saw seam is slightly narrower than that at both ends.

Moreover, while the circular saw blade cutting depth reaches 0.020 m, the damaged area at both ends of the saw seam decreases significantly. It is significantly narrower than the middle section at both ends of the saw seam. With the increasing cutting depth, the damage area at both ends of the saw seam decreases significantly.

The cutting force curves of a circular saw blade cutting rock are shown in Fig. 6. While the circular saw blade contacts the rock, the circular saw blade cuts into the rock vertically at the constant cutting speed and feed speed. The cutting force and vertical force increase sharply with the impact between the circular saw blade and rock. The cutting force and vertical force fluctuate up and down around the stable value, closely related to the cutting depth of the circular saw blade. The cutting force, horizontal force, and vertical force increase with the increase of cutting depth. When the circular saw blade cuts into the rock, the axial force of the saw blade is small. With the increasing cutting depth, the axial force amplitude curve of the saw blade, the contact arc length between

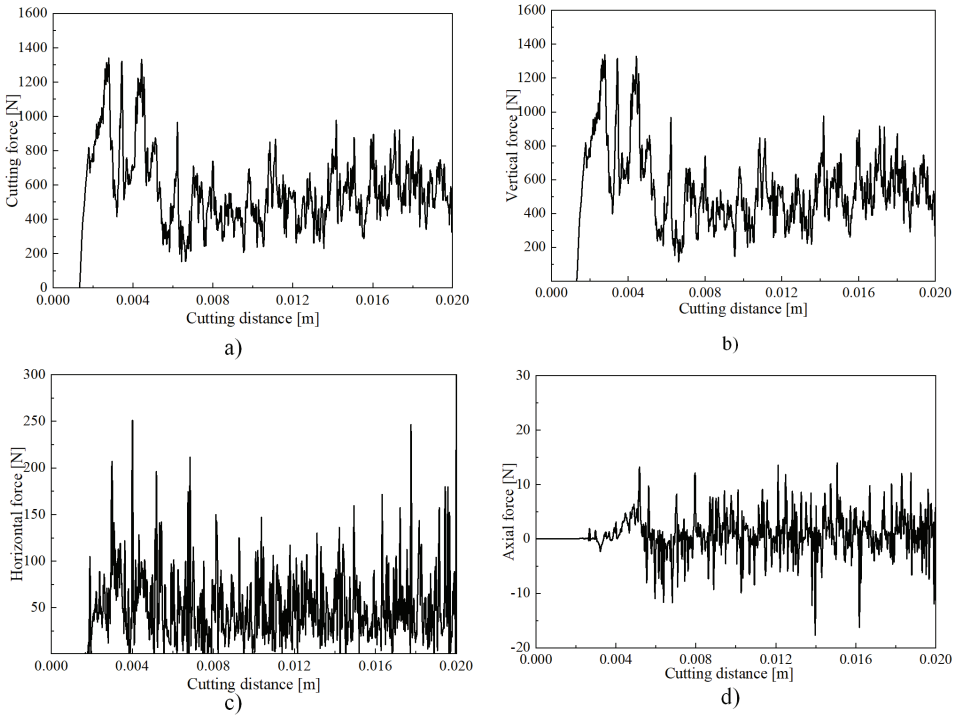

Fig. 6. *The force curve of the circular saw blade cutting rock; a) cutting force curve, b) vertical force curve, c) horizontal force curve, d) axial force curve*

the saw blade and rock increases, and the cutting force and vertical force increase. Meanwhile, the overlap area between the circular saw blade and rock increase with the increasing cutting depth. The discharge speed of rock debris, which is formed by the circular saw blade cutting rock, slows down, and the axial force amplitude increases owing to compression of the circular saw blade what the rock wall at saw seam both sides.

3.2 The Influence of Feed Speed on Circular Saw Blade Cutting Performance

The circular saw blade cuts into rock vertically with a rotation speed of 2000 r/min, and feed speed of 0.10 m/s, 0.15 m/s, 0.20 m/s, 0.25 m/s, and 0.30 m/s. The results of the circular saw cutting rock are shown in Fig. 7. In order to investigate the relation between the average peak cutting force and the feed speed, the cutting depth is controlled by the cutting distance. The stress nephograms of the circular saw blade with various cutting depths are shown in Fig. 7. It is evident that the circular saw blade stress nephogram is closely related to the feed speed. The stress range of the circular saw blade expands with increasing feed speed. When the circular saw blade feed speed is 0.10 m/min, the circular saw blade stress is mainly concentrated in the centre of the circular saw blade matrix, and the area with apparent stress in the circular saw blade segments account for about 35.4 % of the total. While the cutting speed of 0.20 m/min, the stress nephogram of the circular saw blade increases significantly compared with that of the feed speed of 0.10 m/min, and the stress concentration at the edge of the mounting hole of the circular saw blade matrix is more significant than that at the outer edge. There are apparent stress blocks, accounting for about 48.8 % of the total. However, when the feed speed of 0.30 m/min, the circular saw blade stress increases obviously, the matrix stress nephogram expands the four holes position of the circular saw blade matrix, and the stress extends along with the position of the rotation direction. The number of stress blocks increases, accounting for about 50.0 % of the total. With the increase of the feed speed, the water trough stress in the cutting area of the section that contacts the rock appears obvious, and the stress concentration appears at the tip of the section. The stress concentration appears at the connection position between the circular saw blade segments and the circular saw blade matrix.

In the circular saw blade cutting rock process, the rock stress nephograms are shown in Fig. 8. When the circular saw blade cuts into rock with constant cutting depth and rotation speed, it is clear that rock stress

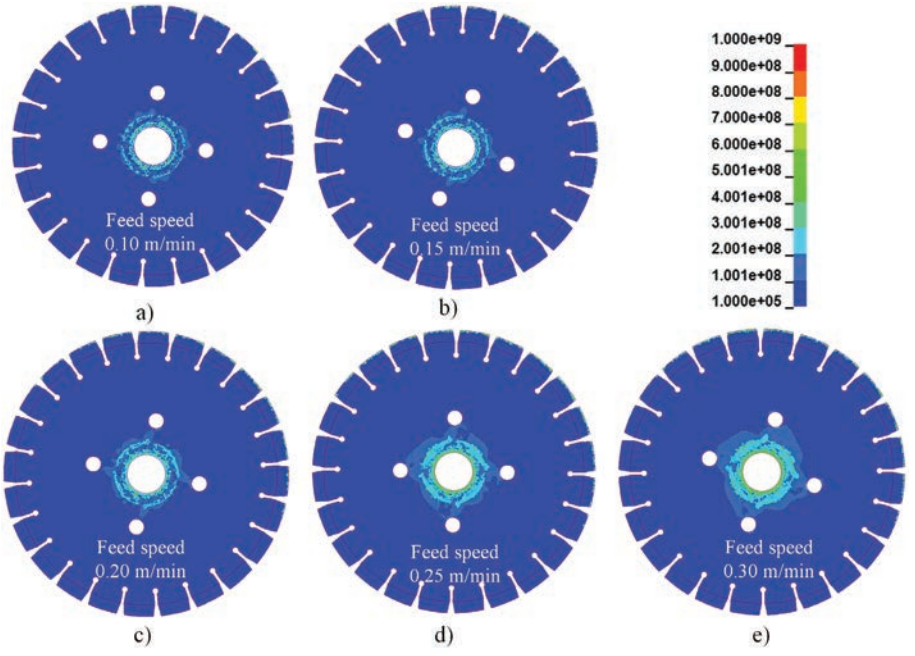

Fig. 7. *The circular saw blade stress nephogram with different feed speed*

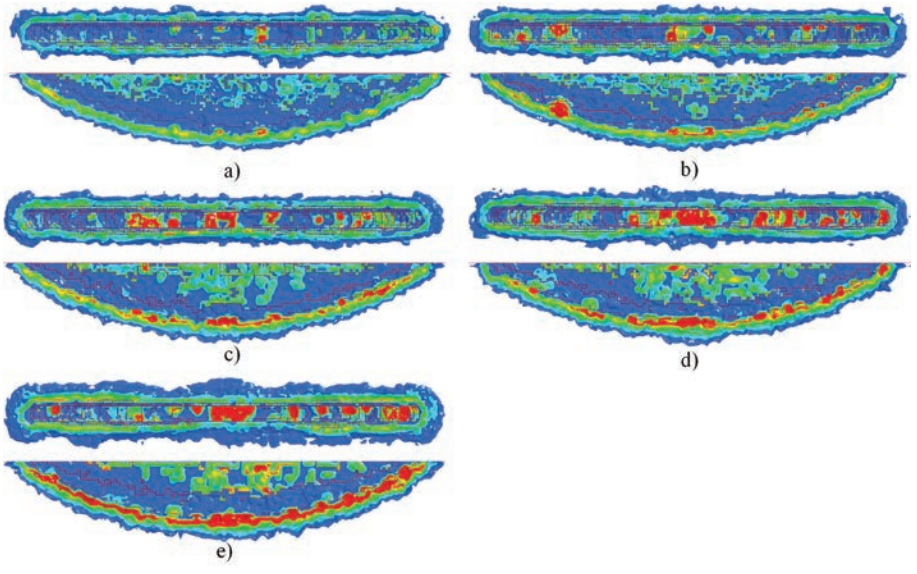

Fig. 8. *The rock stress nephogram with different feed speed; a) feed speed of 0.10 m/min, b) feed speed of 0.15 m/min, c) feed speed of 0.20 m/min, d) feed speed of 0.25 m/min, e) feed speed of 0.30 m/min*

increases with the feed speed increasing. From the top view, the stress concentration area of rock is mainly distributed from the circular saw blade to the middle of the saw seam. The stress concentration gradually increases with the rising circular saw blade feed speed. The rock stress concentration area and the stress area width increase significantly with the circular saw blade feed speed rise. When the feed speed is 0.10 m/min, there are three obvious stress concentration points in the top view and four in the section view. However, when the feed speed increases to 0.30 m/min, 12 stress concentration points are in the top view.

Furthermore, in the rock stress profile, it can be observed that under the condition of a certain rotation speed the rock stress area increases significantly with the increased feed speed. When the feed speed is 0.10 m/min, there are few stress concentration areas on the action arc between the circular saw blade and

rock. The stress concentration areas on the action arc between the circular saw blade and rock increase with the rise of the feed speed. When the circular saw blade feed speed rises 0.30 m/min, the action arc between the circular saw blade and rock forms a continuous stress region. Therefore, the circular saw blade stress increase with the increasing feed speed, and the maximum stress and stress range of the circular saw blade increases significantly.

The circular saw blade cuts the rock at different feed speeds, and the rock damage clouds are presented in Fig. 9. The circular saw blade cuts rock with constant rotation speed and different feed speeds, and the rock damage cloud area and degree are closely related to the feed speed. It can be observed from Fig. 9 that with the increase of feed speed, the width of rock damage cloud increase gradually, and the damage area at both ends of the damage cloud increases obviously. From the observation of the rock damage profile, it can be seen that the scope of rock damage rises significantly, and the damage area at the saw seam bottom increases gradually. With the increasing circular saw blade feed speed, the rock damage area increases and progressively connects with each other. Moreover, the rock damage at the cutting in area of the circular saw blade is more considerable than that

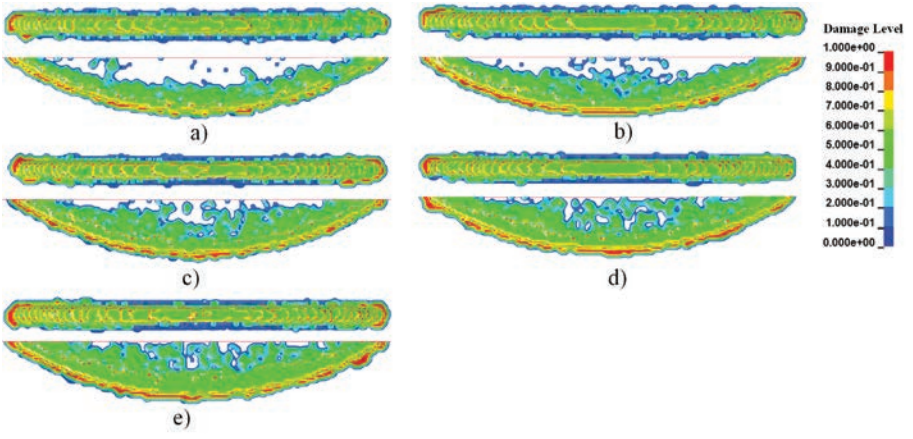

Fig. 9. *The rock damage cloud with different feed speed, a) feed speed of 0.10 m/min, b) feed speed of 0.15 m/min,* c) feed speed of 0.20 m/min, d) feed speed of 0.25 m/min, and e) feed speed of 0.20 m/min

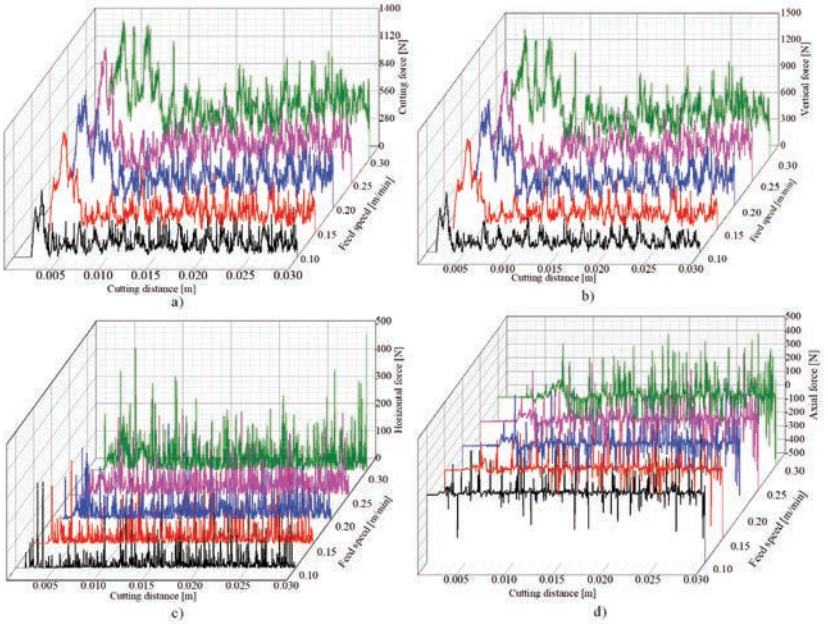

Fig. 10. *The force curves of circular saw blade with different feed speeds; a) cutting force with different feed speeds, b) vertical force with different feed speeds, c) horizontal force with different feed speeds, d) axial force with different feed speeds*

at the cutting out area of the circular saw blade, and the damage range at the lowest part of the saw seam is the largest.

The curves of cutting force, vertical force, horizontal force, and axial force are shown in Fig. 10, showing when the circular saw blade cuts rock with different feed speeds. The cutting force is closely related to the circular saw blade feed speed and increases sharply with increasing feed speed, as presented in Fig. 10a. The circular saw blade‘s horizontal cutting force and vertical cutting force increase obviously with increasing feed speed, as shown in Figs. 10b and c. The curves of cutting force, vertical force, horizontal force of the circular saw blade at different feed speeds show regularity. When the circular saw blade contacts the rock, the force curve increases significantly and decreases sharply, and fluctuates up and down around a stable value. The fluctuation of the circular saw blade cutting force and vertical force curve are similar. The curve of the circular saw blade axial force and the feed speed is shown in Fig. 10d. The axial force of different feed rates is basically same, and there is no obvious change between circular saw blade axial force and feed speed.

With the feed speed of the circular saw blade increasing, the thickness of the rock cutting by a circular saw blade increases while rotating a circle. As a result, the interaction between the circular saw blade and rock increases, and the horizontal and vertical forces increase. However, because of the axial force in the compression of the broken rock between the circular saw blade and the rock wall of the saw seam, the axial force of the circular saw blade appears. Because the rock is quasi-brittle heterogeneous material, the rock fracture under the action of a circular saw blade has apparent randomness, so the force of rock cutting by the saw blade does not necessarily act on the plane of a circular saw blade.

The relation curve between the average peak force of the saw blade and the feed speed is presented in Fig. 11. The average peak force of the circular saw blade increases significantly. The variation trend of the average peak cutting force and the average vertical force is similar, increasing the feed speed. Meanwhile, the average peak horizontal force and axial force of the circular saw blade increase with the increasing feed speed. However, the increased amplitude is less than that of the cutting force and vertical force. The average peak cutting force and the average peak vertical force decrease with the increasing rotation speed, and the difference is significant, but the difference between the average peak horizontal force and average peak axial force is not obvious. The average peak axial force increases with the feed speed,

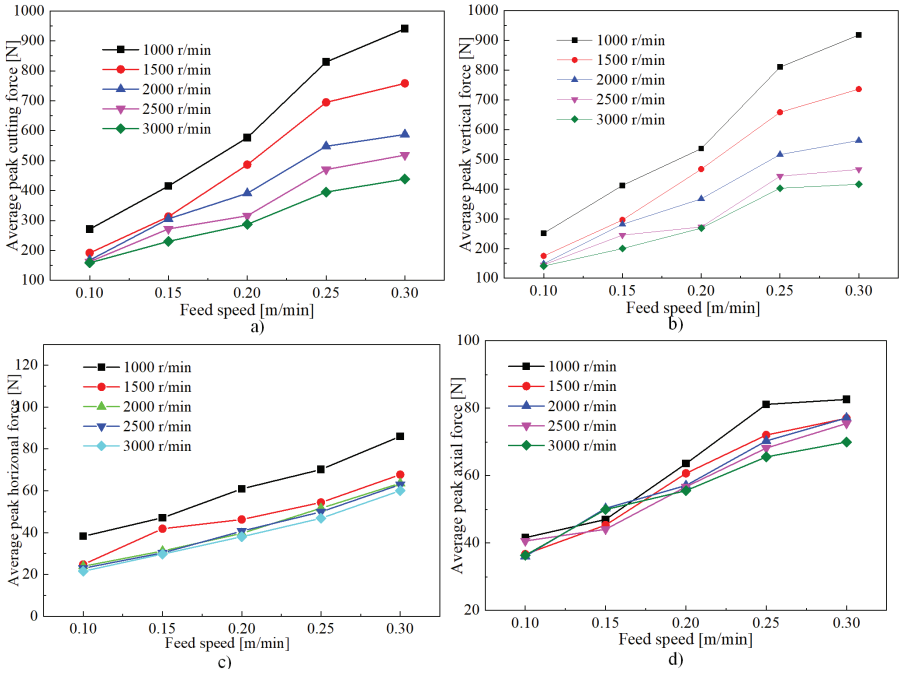

Fig. 11. *The relationship curves between average peak force and feed speed; a) average peak cutting of different feed speeds, b) average peak vertical force of different feed speeds, c) average peak horizontal force of different feed speeds, d) average peak axial force of different feed speeds*

but the average peak axial force has little response to the rotation speed.

3.3 The Influence of Rotation Speed on Circular Saw Blade Cutting Performance

The circular saw blade cuts into the rock at the feed speed of 0.20 m/min and the rotation speed of 1000 r/min, 1500 r/min, 2000 r/min, 2500 r/min, and 3000 r/min. The circular saw blade stress nephogram is shown in Fig. 12. With the increasing rotation speed, there is a significant correlation between the stress cloud area and the peak value of the cloud and the rotation speed. With the increase of the circular saw blade rotation speed, the width of the annular stress area formed in the centre of the saw blade increases obviously. Furthermore, with the increasing rotation speed, the outward radiation area of the circular saw blade stress nephogram expands to the middle of the circular saw blade. The rotation speed significantly affects the

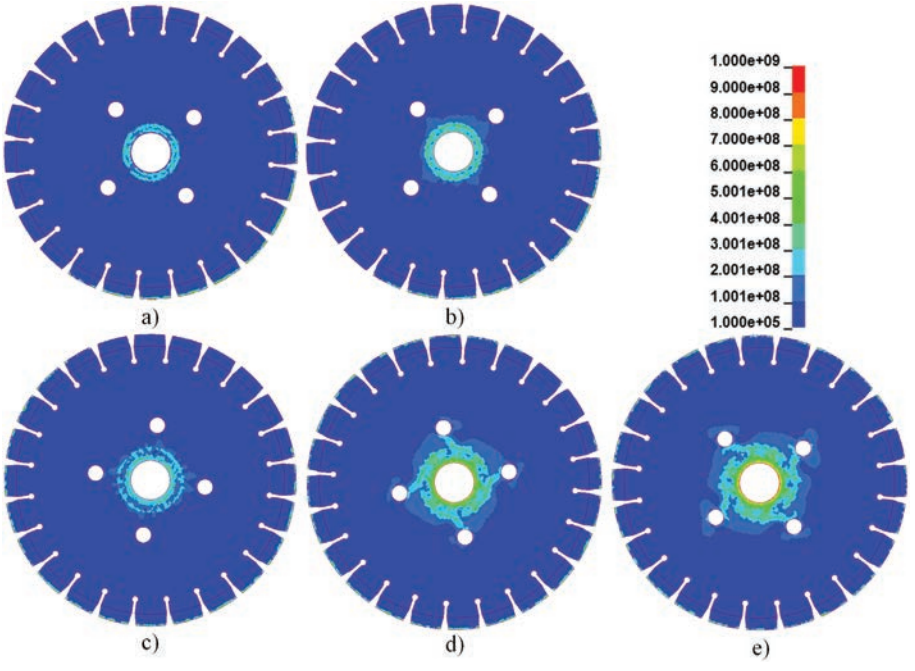

Fig. 12. *The circular saw blade stress nephogram with different rotation speeds; a) rotation speed 1000 r/min, b) rotation speed 1500 r/min, c) rotation speed 2000 r/min, d) rotation speed 2500 r/min, e) rotation speed 3000 r/min*

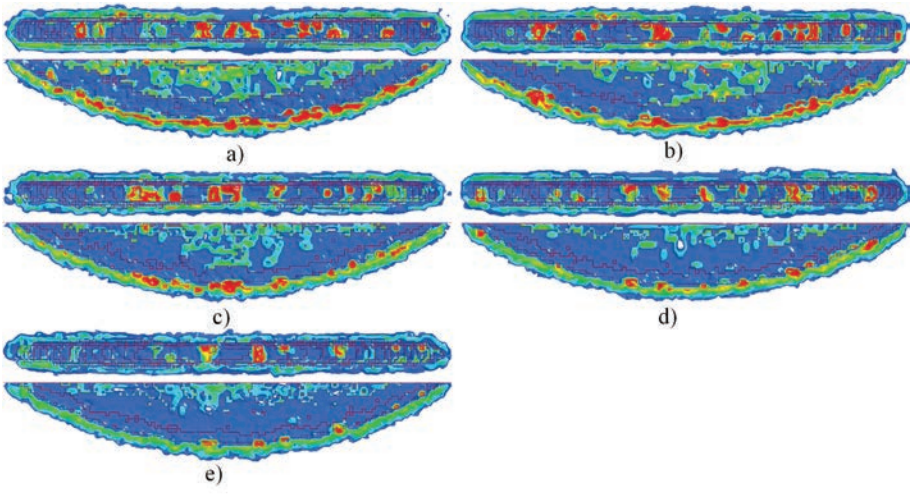

Fig. 13. *The rock stress nephogram with different rotation speeds; a) rotation speed of 1000 r/min, b) rotation speed of 1500 r/min, c) rotation speed of 2000 r/min, d) rotation speed of 2500 r/min, e) rotation speed of 3000 r/min*

stress of the circular saw blade, and the stress range of the saw blade segments increases. When the rotation speed of the saw blade is 1000 r/min, the arc of the apparent stress of circular saw blade segments is about 43.75 %, and when the rotation speed of the saw blade is 3000 r/min, the arc of the apparent stress cloud of the circular saw blade segment is about 100 %.

The rock stress cloud with the circular saw blade cutting rock at different rotational speeds is shown in Fig. 13. According to the rock stress nephogram, the top view and rock stress nephogram are closely related to the rotation speed. Under the circular saw blade action, the rock stress concentration area decreases significantly with the theorized rotation speed. From the top view of the rock stress nephogram, it can be concluded that the rock stress concentration area decreases obviously. Moreover, from the profile of the rock stress nephogram, it can be concluded that the stress concentration area of the rock decreases with the rotation speed increasing. With the increasing rotation speed, the rock stress decreases with the rise of the rotation speed.

The circular saw blade cuts into the rock at different rotation speeds, and the rock damage

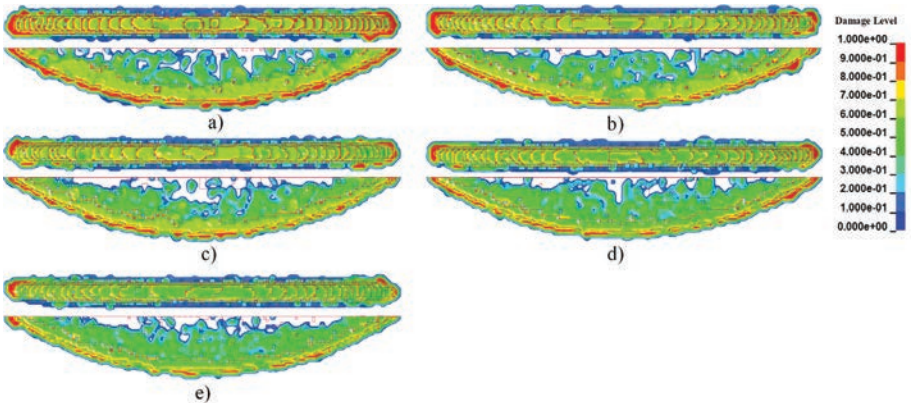

Fig. 14. *The rock damage nephogram with different rotation speeds; a) rotation speed of 1000 r/min, b) rotation speed of 1500 r/min, c) rotation speed of 2000 r/min, d) rotation speed of 2500 r/min, e) rotation speed of 3000 r/min*

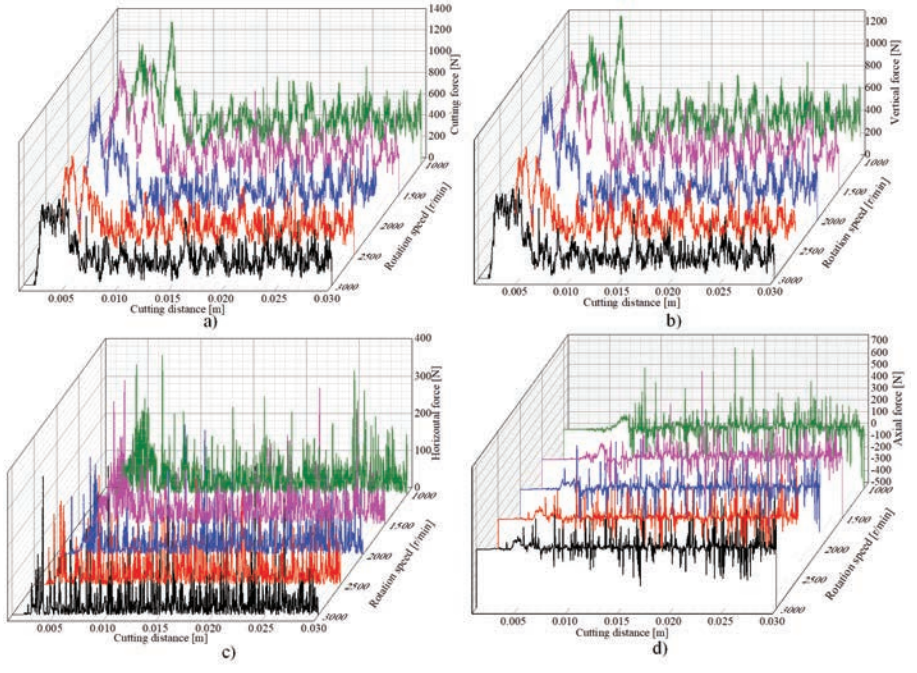

Fig. 15. *The force curves of circular saw blade cutting rock with different rotation speeds; a) cutting force curve of different rotation speeds, b) vertical force curve of different rotation speeds, c) horizontal force curve of different rotation speeds, d) axial force curve of different rotation speeds*

nephograms are shown in Fig. 14. The circular saw blade rotation speed is constant, and the rock damage decreases with the rotation speed increase. From the top view of rock damage nephograms, it is apparent that rock damage gradually decreases, and the rock damage in the cut in and cut out area decreases with the rising rotation speed. In addition, the damage area of the rock saw seam bottom decreases with the increase of the circular saw blade rotation speed. While the rotation speed is 1000 r/min, the damage area at the bottom of the saw seam is connected. When the rotation speed increases to 3000 r/min, the damage area at the saw seam bottom decreases obviously, and the damage breaks off.

The curves of the cutting force, vertical force, horizontal force, and axial force of circular saw blade cutting rock at the cutting speed of 0.20 m/min, the rotation speed of 1000 r/min, 1500 r/min, 2000 r/min, 2500 r/min, and 3000 r/min are shown in Fig. 15. The results show that cutting force, vertical force, horizontal force, and axial force of circular saw blade with different rotation speeds are similar to the distance curve. There is a significant sudden increase when the circular saw blade contacts the circular saw blade rock. There is a negative correlation between the force and rotation speed. After the cutting force returned to stable fluctuation, the circular saw blade's cutting force and vertical force were positively correlated with the circular saw blade cutting depth. The changing trend of fluctuation increases. The fluctuation of the horizontal force curve of the circular saw blade decreases, and the horizontal force increases sharply when the circular saw blade contacts the rock. It returns to stability in a short time. Compared with the cutting force, vertical force, and horizontal force, the axial force appears later. The axial force fluctuates up and down around the stable value, and the fluctuation amplitude decreases with the increases of circular saw blade rotation speed.

The circular saw blade cut into rock vertically with the constant feed speed and rotation speed. At the moment of the circular saw blade contacting rock, the cutting force, horizontal force, vertical force curves increase sharply, owing to the impact of the circular saw blade. However, the relationship between peak cutting force and the rotation speed is significant, and rotation speed substantially affects the effects of the circular saw blade. The circular saw blade cuts rock at a constant feed speed. The rotation speed directly affects the cutting amount of circular saw blades in one cycle and then affects the cutting and transverse forces. When the rotation speed is low, the cutting amount of the saw blade for a cycle increases, but the cutting force, vertical force, and horizontal force

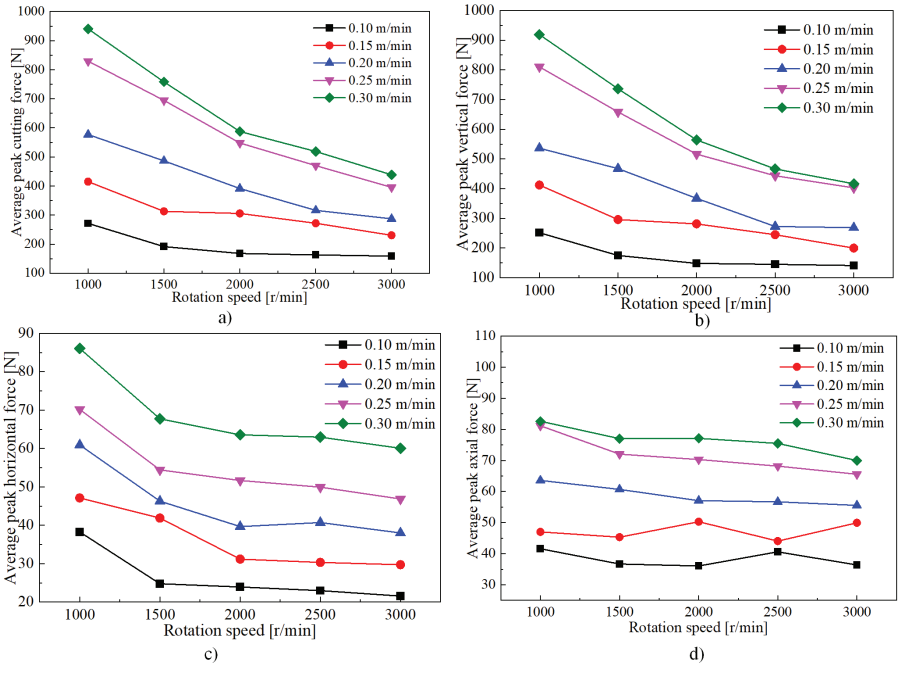

Fig. 16. *The average peak force with different rotation speeds; a) average peak cutting force of different rotation speeds, b) average peak vertical force of different rotation speeds, c) average peak horizontal force of different speeds, d) average peak axial force of different rotation speeds*

increase. The rotation speed directly affects the discharge speed of rock debris, so the axial force of the circular saw blade is affected by the rotation speed of the saw blade and decreases with the increase of the rotation speed.

The average peak cutting force, vertical, horizontal, and axial force curves with different feed speeds are plotted in Fig. 16. The average peak cutting force, vertical, horizontal, and axial force correlate closely with rotation speed. With increasing rotation speed, the cutting force, vertical force, horizontal force, vertical force, and axial force decreases, but the reduced amplitude decreases. The average peak cutting force, vertical force, horizontal force, and axial force of circular saw blade respond rapidly to the speed of the circular saw blade. It is apparent that the cutting force and vertical force are significantly affected by the rotation speed of the circular saw blade, and the variation trend is similar. The horizontal force of the circular saw blade decreases slightly with the increase of the rotation speed, which is slightly less than the cutting force and vertical force of the circular saw blade. However, the rotation speed curves of the average peak cutting force, vertical force, horizontal force, and axial force of the circular saw blade under different feed speeds do not cross.

3.4 The Double Circular Saw Blades Distance Influence on Cutting Performance

The double circular saw blade cuts vertically with a feed speed of 0.20 m/min, a rotation speed of 2000 r/min, and a distance between double circular saw blades of 30 mm. The curves of cutting force, vertical force, horizontal force, axial force, and cutting distance of single and double circular saw blades are shown in Fig. 17. Comparing the cutting force of the single circular saw blade and double circular saw blades, it can be seen that the cutting force, vertical force, horizontal force, and axial force of the double circular saw blade are smaller than that of the single circular saw blade. When the circular saw blade contacts the rock, the impact action of the circular saw blade results in a sharp increase in the force position curve. After the stable cutting, the cutting force curve restores to the stable value. The cutting force, vertical force, horizontal force fluctuate up and down around the stable value, and show an upward trend, because the superposition effect of the cutting force of the double circular saw blade is smaller than that of the single circular saw blade, and the fluctuation range of the cutting force, vertical force and horizontal force of the double circular saw blade is smaller than that of the single circular saw blade. Comparing the curves of the axial force curve of the single circular

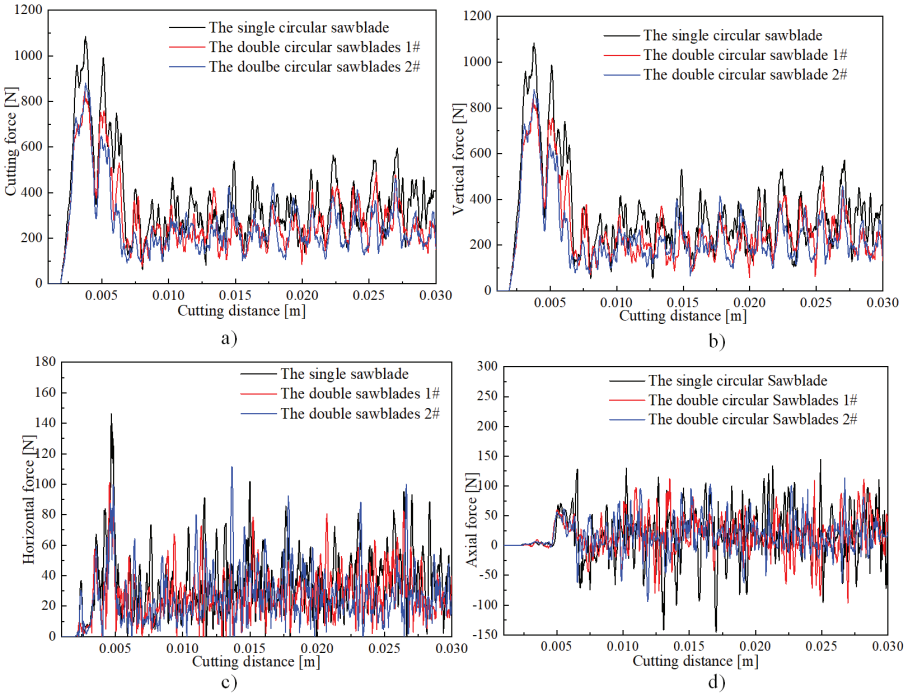

Fig. 17. *The force curves of single circular saw blade and double circular saw blades*

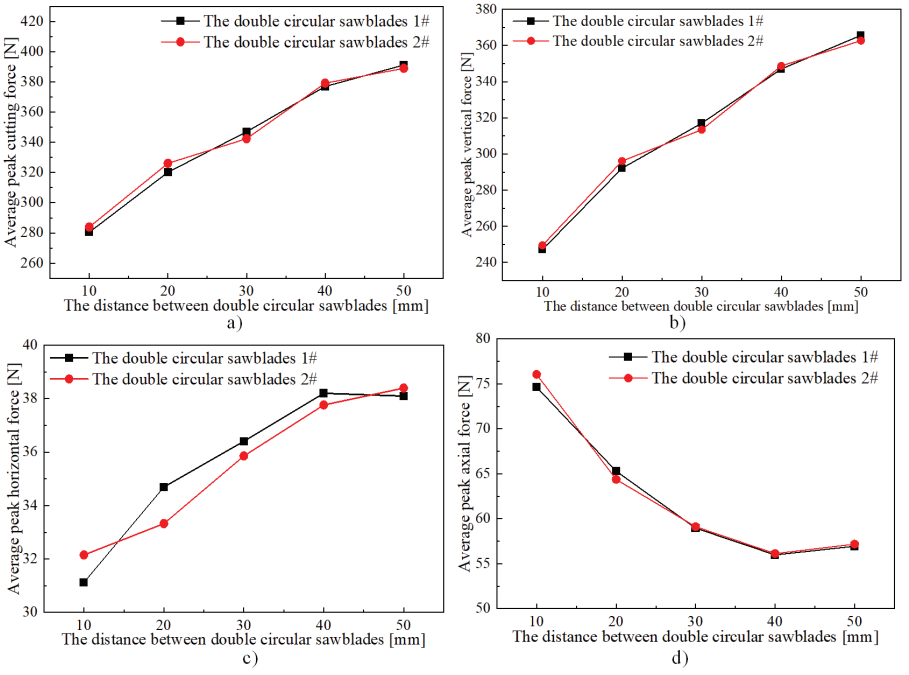

Fig. 18. *The average peak force of the double circular saw blade with different distances between double circular saw blades; a) the average peak cutting force of different distance between double circular sawblades, b) the average peak vertical force of different distance between double circular sawblades, c) the average peak horizontal force of different distance between double circular sawblades, d) the average peak axial force of different distance between double circular sawblades*

saw blade and the double circular saw blade, the axial force fluctuation of the axial force curve of the double circular saw blade is smaller than that of the single circular saw blade. Therefore, with the same cutting parameters, the double circular saw blade cutting rock is conductive to reducing the impact load and can effectively improve the service life of the circular saw blade.

The results show that the circular saw blade cutting rock with the rotation speed of 2000 r/min, the feed speed of 0.20 m/min, and the distance between the double circular saw blade is 10 mm, 20 mm, 30 mm, 40 mm, and 50 mm, respectively. The curves of the average peak cutting force, vertical force, horizontal force, and axial force of the double circular saw blade are shown in Fig. 18. With the increase of the double circular saw blades, the average peak cutting force, vertical force, horizontal force gradually increase and tend to be stable. The average peak cutting force decreases gradually and tends to be stable. This is seen by comparing the cutting force, vertical force, horizontal force, and axial force of the double circular saw blade. When the distance of the double circular saw blades are small, the average peak cutting force, vertical force, horizontal force, and axial force of the circular saw blade are significantly smaller than that of the single circular saw blade. However, the axial force of the double circular saw blade is more significant than that of the single circular saw blade. With the distance between the double circular saw blade increase, the average peak cutting force, vertical force, horizontal force, and the axial force of the double circular saw blade are close to that of the single saw blade.

When the double circular saw blades cut into the rock vertically, the double circular saw blades spacing significantly affects the stress superposition of the double circular saw blades. The stress distribution of the single circular saw blade cutting rock presents a large arc, while the double saw blades cut rock with different distances between the double circular saw blades. The stress superposition of rock is closely related to the double circular saw blade spacing. Owing to the superposition of the stress acting on the rock, the average peak cutting force, vertical force, and horizontal force are closely related to the distance between the double circular saw blades. However, due to the superimposed stress of the double saw blade, the axial force of the saw blade is negatively correlated with the distance between the double circular saw blades. When the distance between the two saw blades is small, the axial force of the rock cutting by the

double circular saw blades is significantly greater than that cut by the single circular saw blade. When the distance between double circular saw blades increases to a certain distance, the average peak cutting force, vertical force, horizontal force, and axial force are similar to those of the single circular saw blade.

4 CONCLUSION

The flexible circular saw blade cutting into rock process with different feed speeds and rotation speeds was investigated based on the ANSYS/LS-DYNA. The cutting parameters of the circular saw blade influence the stress distribution of flexible circular saw blade and rock, as well as the cutting force, vertical force, horizontal force, and axial force. The conclusions are as follows:

(1) The feasibility of the numerical simulation is verified by uniaxial compression test and uniaxial compression numerical simulation to correct the accuracy of the rock cutting model of the flexible circular saw blade.
(2) The results indicated that the stress distribution range of a flexible circular saw blade increases with the increase of feed speed and rotation speed. The stress distribution of circular saw blade segment and circular saw blade has a significant correlation with cutting parameters.
(3) The cutting force of the circular saw blade is closely related to the cutting parameters of the saw blade, which decreases with the increase of the rotation speed of the saw blade and increases with the growth of the feed speed.
(4) The results show that the double saw blade‘s cutting force, vertical force, and horizontal force are smaller than that of the single saw blade, but the axial force is more significant than that of the single saw blade.
(5) The cutting force, horizontal force, and vertical force of double saw blade increase with the increase of saw blade spacing, but the axial force of the saw blade decreases with the increase of saw blade spacing.

In the future investigation, I will study the circular saw blade cutting different kinds of hard rocks and research the rock parameters effects on the circular saw blade cutting performance and rock fracture.

5 ACKNOWLEDGEMENTS

This work was supported by the projects of the Key Research and Development project of China (Grant No. 2017YFC0603000), Shandong Provincial Key Research and Development Project (2019SDZY01), and the Natural Science Foundation of Shandong Province (Grant No. ZR2019BEE069).

6 REFERENCES

[1] Aydin, G., Karakurt, I., Aydiner, K. (2013). Development of predictive models for the specific energy of circular diamond saw blades in the sawing of granitic rocks. *Rock Mechanics Rock Engineering*, vol. 46, p. 767-783, **DOI:10.1007/s00603-012-0290-6**.

[2] Aydin, G., Karakurt, I., Hamzacebi, C. (2015). Performance prediction of diamond saw blades using artificial neural network and regression analysis. *Arabian Journal for Science and Engineering*, vol. 40, p. 2003-2012, **DOI:10.1007/s13369-015-1589-x**.

[3] Aydin, G., Karakurt, I., Aydiner, K. (2013). Wear performance of saw blades in processing of granitic rocks and development of models for wear estimation. *Rock Mechanics and Rock Engineering*, vol. 46, p. 1559-1575, **DOI:10.1007/s00603-013-0382-y**.

[4] Goktan, R.M., Yilmaz, N.G. (2017). Diamond tool specific wear rate assessment in granite machining by means of Knoop micro-hardness and process parameters. *Rock Mechanics and Rock Engineering*, vol. 50, p. 2327-2343, **DOI:10.1007/s00603-017-1240-0**.

[5] Li, Y., Huang, H., Shen, J.Y., Xu, X.P., Gao, Y.S. (2002). Cost-effective machining of granite by reducing tribological interactions. *Journal of Materials Processing Technology*, vol. 129, no. 1-3, p. 389-394, **DOI:10.1016/S0924-0136(02)00699-4**.

[6] Yilmaz, N.G. (2016). Size analysis of the chips generated during abrasive machining of granite in relation to productivity and efficiency parameters. *Particulate Science and Technology*, vol. 34, no. 5, p. 593-601, **DOI:10.1080/02726351.2015.1096872**.

[7] Ataei, M., Mikaeil, R., Hoseinie, S.H., Hosseini, S.M. (2012). Fuzzy analytical hierarchy process approach for ranking the sawability of carbonate rock. *International Journal of Rock Mechanics and Mining Sciences*, vol. 50, p. 83-93, **DOI:10.1016/j.ijrmms.2011.12.002**.

[8] Atici, U., Ersoy, A. (2009). Correlation of specific energy of cutting saws and drilling bits with rock brittleness and destruction energy. *Journal of Materials Processing Technology*, vol. 209, no. 9, p. 2602-2612, **DOI:10.1016/j.jmatprotec.2008.06.004**.

[9] Aslantas, K., Ozbek, O., Ucun, I., Buyuksagis, I.S. (2009). Investigation of the effect of axial cutting force on circular diamond saw blade used in marble cutting process. *Material and Manufacturing Processes*, vol. 24, no. 12, p. 1423-1430, **DOI:10.1080/10426910903344039**.

[10] Ersoy, A., Atici, U. (2004). Performance characteristics of circular diamond saws in cutting different types of rocks. *Diamond and Related Materials*, vol. 13, no. 1, p. 22-37, **DOI:10.1016/j.diamond.2003.08.016**.

[11] Tumac, D. (2015). Predicting the performance of large diameter circular saws based on Schmidt hammer and other properties for some Turkish carbonate rocks. *International*

Journal of Rock Mechanics and Mining Sciences, vol. 75, p. 159-168, **DOI:10.1016/j.ijrmms.2015.01.015**.

[12] Tumac D. (2016). Artificial neural network application to predict the sawability performance of large diameter circular saws. *Measurement*, vol. 80, p. 12-20, **DOI:10.1016/j.measurement.2015. 11.025**.

[13] Mikaeil, R., Haghshenas, S.S., Haghshenas, S.S., Ataei M. (2016). Performance prediction of circular saw machine using imperialist competitive algorithm and fuzzy clustering technique. *Neural Computing and Applications*, vol. 29, p. 283-292, **DOI:10.1007/s00521-016-2557-4**.

[14] Yilmaz, N.G. (2013). Process efficiency comparison of a sandwich-core saw blade and a conventional saw blade used in stone-machining. *Journal of Cleaner Production*, vol. 47, p. 26-31, **DOI:10.1016/j.jclepro.2013.01.042**.

[15] Tonshoff, H.K., Hilmann-Apmann, H., Asche, J. (2002). Diamond tools in stone and civil engineering industry: cutting principles, wear and applications. *Diamond and Related Materials*, vol. 11, p. 736-741, **DOI:10.4028/www.scientific.net/KEM.250.103**.

[16] Xu, X., Li, Y., Yu, Y. (2003). Force ratio in the circular sawing of granites with a diamond segmented blade. *Journal of Materials Processing Technology*, vol. 139, no. 1-3, p. 281-285, **DOI:10.1016/S0924-0136(03)00236-X**.

[17] Karakurt, I., Aydin, G., Aydiner, K. (2013). Experimental and statistical analysis of cutting force acting on diamond sawblade in sawing of granitic rocks. *Proceedings of the Institution of Mechanical Engineers, Part B: Journal of Engineering Manufacture*, vol. 227, no. 2, p. 286-300, **DOI:10.1177/0954405412460971**.

[18] Buyuksagis, I.S., Goktan, R.M. (2005). Investigation of marble machining performance using an instrumented block-cutter. *Journal of Materials Processing Technology*, vol. 169, no. 2, p. 258-262, **DOI:10.1016/j.jmatprotec.2005.03.014**.

[19] Jiang, K., Gao, K., Wan, L. (2020). Effect of gangue distributions on cutting force and specific energy in coal cutting. *Strojniški vestnik - Journal of Mechanical Engineering*, vol. 66, no. 3, p. 203-212, **DOI:10.5545/sv-jme.2019.6461**.

[20] Agarwal, S., Rao, P.V. (2008). Experimental investigation of surface/subsurface damage formation and material removal mechanisms in SiC grinding. *International Journal of Machine Tools and Manufacture*, vol. 48, no. 6, p. 698-710, **DOI:10.1016/j.ijmachtools.2007.10.013**.

[21] Burek, J., Plodzien, M., Zylka, L., Sulkowicz, P. (2019). High-performance end milling of aluminum alloy: Influence of different serrated cutting edge tool shapes on the cutting force. *Advances in Production Engineering & Management*, vol. 14, no. 4, p. 494-506, **DOI:10.14743/apem2019.4.344**.

[22] Lu, Z., Zeng, Q., Wang, Z., Li, X., Gao, K. (2019). Experimental and numerical studies on rock cutting with saw blade and conical pick combined cutting method. *Mathematical Problems in Engineering*, vol. 2019, art. ID 5046873, **DOI:10.1155/2019/5046873**.

[23] Zeng, Q., Wang, Z., Lu, Z., Wan, L., Zhang, X. (2021). Numerical simulation of the influence of the distance between the diamond sawblade and free surface on cutting performance. *Shock and Vibration*, vol. 2021, art. ID 2958204, **DOI:10.1155/2021/2958204**.

[24] Hoang, H.T., Nguyen, N.T., Tran, D.Q., Nguyen, V.T. (2019). cutting forces and surface roughness in face-milling of SKD61 hard steel. *Strojniški vestnik - Journal of Mechanical Engineering*, vol. 65, no. 6, p. 375-38, **DOI:10.5545/sv-jme.2019.6057**.

[25] Liu, J., Sun, J., Zaman, U.K.U., Chen, W. (2020). Influence of wear and tool geometry on the chatter, cutting force, and surface integrity of TB6 titanium alloy with solid carbide cutters of different geometry. *Strojniški vestnik - Journal of Mechanical Engineering*, vol. 66, no. 12, p. 709-723, **DOI:10.5545/sv-jme.2020.6714**.

[26] Fernando, P.K.S.C., Pei, Z.J., Zhang, M.. (2020). Mechanistic cutting force model for rotary ultrasonic machining of rocks. *International Journal of Advanced Manufacturing Technology*, vol. 109, p. 109-128, **DOI:10.1007/s00170-020-05624-z**.

[27] Zuperl, U., Cus, F., Zawada-Tomkiewicz, A., Stepien, K. (2020). Neuro-mechanistic model for cutting force prediction in helical end milling of metal materials layered in multiple directions. *Advances in Production Engineering and Management*, vol. 15, no. 1, p. 5-17, **DOI:10.14743/apem2020.1.345**.

[28] Peng, Z.H., Fang, C.F. (2019). Study on force distribution and its location in granite sawing. IOP Conference Series: Materials Science and Engineering, vol. 504, art. ID 012112, **DOI:10.1088/1757-899X/504/1/012112**.

[29] Liu, S.F., Lu, S.F., Wan, Z.J., Cheng, J.Y. (2019). Investigation of the influence mechanism of rock damage on rock fragmentation and cutting performance by the discrete element method. *Royal Society Open Science*, vol. 6, art. ID 190116, **DOI:10.1098/rsos.190116**.

Strojniški vestnik - Journal of Mechanical Engineering 67(2021)12, 666-681

DOI:10.5545/sv-jme.2021.7289 Review Scientific Paper
Received for review: 2021-06-11
Received revised form: 2021-09-18
Accepted for publication: 2021-10-29

Review of Peridynamics: Theory, Applications, and Future Perspectives

Gábor Ladányi[1] – Viktor Gonda[2]
[1]University of Dunaújváros, Institute of Engineering Sciences, Hungary
[2]Óbuda University, Donát Bánki Faculty of Mechanical and Safety Engineering, Hungary

The modelling and simulation of material degradations, particularly fractures in solids of different lengths and time scales, remains challenging despite the numerous approaches that have been developed. In this review, the focus is set on research work concerned with a very promising non-local method: peridynamic modelling. With this approach, continuous phenomena may be described, and the complete evolution (i.e., initiation, propagation, branching, or coalescence) of cracks and other discontinuities can be followed in solids in an integrated framework. Evaluating the large number of publications on this topic, the authors chose to present concisely the key concepts, applications, and results in identifying possible future paths: the incorporation of mechanics of large deformations and material nonlinearities, and the development of high-efficiency peridynamic solvers. This review does not intersect with recent relevant reviews, which reflects its significance to readers.
Keywords: peridynamics, fracture mechanics, damage mechanics, non-local mechanics

Highlights
- *Basic concepts and different branches of peridynamic modelling of crack propagation are introduced.*
- *The evolution of peridynamic research is assessed based on a wide and representative review of the literature.*
- *The most frequent fields of applications are highlighted where consensus and contention are reached in modelling.*
- *Evaluating the features of peridynamic modelling, future research perspectives are highlighted in treating material and geometrical nonlinearities, improving numerical efficiency.*

0 INTRODUCTION

Analytical and numerical methods of continuum physics are the most successful methods in solving engineering problems of solid and fluid mechanics. As the performance of computers has increased, motivated by safety and economic reasons, the field of solvable problems has become wider. New maintenance strategies introduced reliability and risk-based operation methods **[1]** and **[2]**. In these methods, the damage of a structure may not lead to the end of its operability. The lifetime ends when reliability decreases under a predefined limit. The definition of this criterion and the estimation of the risk require the analysis of the damaged structure.

Structural failure is a complex phenomenon; it is usually initiated on the micro-scale with micro-damage of the material. After the evolution of microdamage, damage appears in the meso- and macro-scales. As this mechanism is in process, the mechanical behaviour of the whole structure may change (e.g., post-buckling behaviour or unstable, brittle failure); sometimes, the change is localized (e.g., ductile failure).

In classical continuum mechanics (CCM), the continuity and usually the differentiability of the state variables are assumed. As failure involves discontinuities, solving the governing equations defined by CCM with typical computational methods is troublesome **[3]**. CCM can follow the displacements and strain field as a function of external loads with various material models from simple elasticity to the viscoplastic flow of solids. Limitations of the analytical description are reached when discontinuities appear in any state variables. Continuum damage mechanics can account for the effect of the microcracks and voids through homogenized material properties **[4]**. Unfortunately, it fails when the size of the damaged zone reaches the macroscale **[5]**.

For an accurate simulation of the fracture process, the numerical method needs to be capable of modelling crack initiation, propagation, bifurcation, coalescence, and separation. Classical linear elastic fracture mechanics (LEFM) or non-linear fracture mechanics (NLFM) may be applied for the load-bearing structures of simple geometry and predefined cracks only. By employing special numerical methods, e.g., extended finite element method (X-FEM) **[6]** or meshless methods **[7]**, more complicated problems can be solved with acceptable accuracy. The chosen method is acceptable if it is not mesh-dependent. In most cases, the mesh generation at every time step of the solution is necessary to fulfil this requirement **[6]**. The increased time of mesh generation is a very serious drawback. Additionally, crack initiation and crack branching remain open questions in this context,

*Corr. Author's Address: University of Dunaújváros, Institute of Engineering Sciences, Táncsics M. u. 1/a, 2400 Dunaújváros, Hungary, ladanyi@uniduna.hu

and the crack-tip kinematics has to be controlled with artificial criteria [3].

The above problems are not inherited in the analysis of discrete mechanical systems, e.g., molecular dynamics [8]. Unfortunately, on the available computational resources, only a very limited volume and time segment can be handled: the size of the observable body is at 10^{-6} m^3 in volume, and the time segment is in 10^{-6} s scale. In these models, an ultra-high speed load is necessary. From experimental results, it is uncertain whether the mechanism of damage at ultra-high speed is similar to that at normal speed [9].

These drawbacks and open questions were the motivation, in the year 2000, when the first article of Silling was published, founding the basics of the peridynamic material model [10]; several publications have followed this.

This review aims to summarize the state of the art of the peridynamic theory of solids concisely, and highlight possible future directions. The review is concerned with the theoretical background, classification, and the recent applications of peridynamics. A deep investigation into the different approaches of the peridynamic modelling and the details of numerical implementation is outside the scope of this work. Based on the review, we are identifying and emphasizing four paths of developments in peridynamics: (1) handling materials nonlinearity with improvements in solver technology, (2) handling geometric nonlinearity with improved numerical stability, (3) efficiency of numerical solvers, and application of parallel computing, and (4) applications in coupled multiphysical problems.

The theory and classification of peridynamics are described in Section 1. The peridynamic specified enforcement of boundary conditions and the simulation of discontinuities are also covered in this section. Constitutive models of peridynamics and their applications are described in Section 2. All the references cited in this review can help to navigate and find the appropriate publication between the expansive set of peridynamics related papers.

1 THE PERIDYNAMIC THEORY

The name of the peridynamic model was proposed from ancient Greek words “near” and “force”. The model is a strongly non-local model; the equilibrium (or the motion) of the material particle is affected by finite distance interactions [10].

With its first formulation during the motion and deformation, each particle pairs have an internal force between them, and the motion of a particle depends on the sum of these forces. Let X and X' be two arbitrary particles of the body. Let $u(X,t)$ be the displacement field. The equations of motion of particle X are:

$$\rho \cdot \ddot{u} = L_u + b, \tag{1}$$

$$L_u = \int_V f\left(u,u',t\right)dX', \tag{2}$$

where b is a prescribed volumetric load, ρ is the mass density and is the acceleration at particle X. The L_u operator is the peridynamic force function. It represents the non-local effect on particle X caused by the deformation of its environment.

1.1 The Bond-Based Peridynamic (BB-PD) Model

In Silling’s pioneering article [10], the so-called bond based model was introduced, which proved to be very accurate. The peridynamic force, f was the exclusive function of the relative displacement vector, $\eta = u' - u$. The scheme of the bond-based kinematics and kinetics is shown in Fig. 1. Despite the simplicity of the model, it was proved to be highly successful at modelling crack initiation, propagation, and branching in brittle materials.

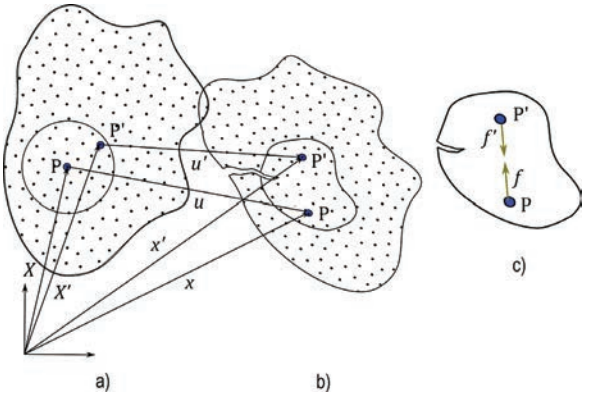

Fig. 1. *The kinematics and kinetics of neighbours in Bond-based Peridynamic model; a) initial (undeformed) configuration of the body, b) current (deformed) configuration of the body, c) the pairwise force between material points*

In this model, the material was linear elastic originating from the relation between the stretch of the bond between the two particles and the linear peridynamic force. Nevertheless, the relation was strongly non-linear in a geometric sense. The direction of the peridynamic force was parallel with the current direction of the relative position.

In physical interactions, the intensity of the effects usually decreases rapidly with the distance between the interacting particles. It suggests defining

a characteristic length to cut the radius of interaction around particle X. In peridynamic literature, this radius is referred to as material horizon, δ. Let the reference vector of two arbitrary particles X and X' be $\xi := X - X'$. The intensity of interaction between two points can be characterized by an influence function $\omega(X, X')$. The influence function is a strictly positive, finite support function. The radius of the support is the material horizon. When it depends only on the reference vector, $\omega(X, X') = \breve{\omega}(\xi)$, it is called structureless. If it depends only on the Eulerian length of the reference vector, $\omega(X, X') = \breve{\omega}(|\xi|)$, it is called 'spherical'! [11].

Let $\mathcal{H}_X$ be the set of points in the body where $\omega(X, X') > 0$. The $\mathcal{H}_X$ set is called to a family of particle X. Assuming a finite material horizon, Eq. (2) can be written in simplified form:

$$L_u = \int_{\mathcal{H}_X} f(u, u', t)\, dX'. \tag{3}$$

In the peridynamic model, the force function $\boldsymbol{f}$ contains all the constitutive information. In the previous two decades, this very simple model was applied in many fields of engineering: elasticity, plasticity, damage and fracture of solids, heat conduction and thermo-elasticity, etc. Some applications are summarized in Section 3.

Unfortunately, bond-based peridynamics have some disadvantages, e.g., the limited value of Poisson's ratio or the disability of the separation of volumetric from distortional deformation, which required the development of a more general theory of peridynamics.

1.2 The State-Based Peridynamic (SB-PD) Mechanical Model

Independently of the formulation in the above-cited articles, a generalized version of the peridynamic model was proposed by Silling et al. [12]. By employing the main concept of the state-based model, the peridynamic force between two material points is the function of the deformation state of the points.

The state of order (m) is a tensor-vector function $\mathcal{A}\langle\cdot\rangle$. The most relevant applications of the states are the scalar (0th-order), vector (1st-order) and tensor (2nd-order) states.

The initial and the current configuration of a material point can be described by *the reference state* $\mathcal{X}$ and the deformed state $\mathcal{Y}$, respectively:

$$\mathcal{X}[X]\xi = \xi = X' - X, \tag{4}$$

$$\mathcal{Y}[X]\xi = \xi + \eta = x' - x. \tag{5}$$

The displacement state $\mathcal{U}$ can be defined with a similar expression:

$$\mathcal{U}[X]\xi = u' - u. \tag{6}$$

Neither the reference nor the deformed state, as shown in Fig, 2, have to be a continuous function of the vector variable.

However, a first-order state is a more general vector-vector function; therefore, the reduced form of the state can be defined. Vice versa, if a tensor is given, then an expanded state can be defined.

Fig. 2. *The neighbourhood (family) around a material point in State-based peridynamics; a) the reference state $\mathcal{X}[X]$, and b) the deformed state $\mathcal{Y}[X]$*

Let $\omega(X, X')$ be the influence function. Let ξ be the reference vector, and W be a second-order tensor. The vector state expanded from the tensor is

$$\mathcal{V}[X]\xi = W \cdot \xi. \tag{7}$$

The tensor product of two vector states A and B is defined as:

$$A * B = \int_{\mathcal{H}_X} \omega(X, X') \cdot A\langle\xi\rangle \otimes B\langle\xi\rangle\, dX'. \tag{8}$$

The reference shape tensor is defined as

$$K = \mathcal{X} * \mathcal{X}. \tag{9}$$

Let $\mathcal{V}$ be a vector state. The *tensor reduced form* W of the vector state is

$$W = (\mathcal{V} * \mathcal{X}) \cdot K^{-1}, \tag{10}$$

It is worth mentioning, assuming continuous displacements, the 0-limit of horizon leads to

$$F(X) = \lim_{\delta \to 0}\left((\mathcal{Y} * \mathcal{X}) \cdot K^{-1}\right), \tag{11}$$

where $F(X)$ is the deformation gradient of CCM at particle X [12].

Let a and b are two vector states. The dot product between the two vector states is defined by

$$a \bullet b = \int_{\mathcal{H}_X} A\langle\xi\rangle \cdot B\langle\xi\rangle\, dX'. \tag{12}$$

In CMM, the constitutive information is contained in the stress-strain relationship. In bond-based peridynamic theory, the material behaviour

is described through the bond stretch–bond force relationship. In state-based peridynamics, the deformation state–force state relationship plays this role. The force state is a deformation-dependent vector-vector function. The equation of motion contains the force state.

$$\rho \cdot \ddot{u} = L_u + b, \tag{13}$$

$$L_u = \int_{\mathcal{H}_X} T\left[X,t\right]\left\langle \xi \right\rangle - T\left[X',t\right]\left\langle -\xi \right\rangle dX'. \tag{14}$$

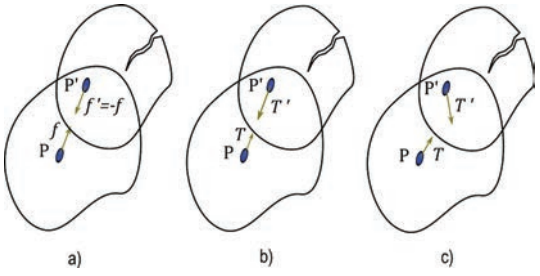

Fig. 3. *The kinetics of state-based peridynamics; a) properties of bond-based, b) ordinary- and c) non-ordinary state-based peridynamic force*

It is worth introducing the reference and deformed direction states, respectively:

$$e_r\left\langle \mathcal{X} \right\rangle = \frac{\mathcal{X}}{\left|\mathcal{X}\right|}, \tag{15}$$

$$M\left[X\right]\left\langle X'-X \right\rangle = \frac{\mathcal{Y}}{\left|\mathcal{Y}\right|}. \tag{16}$$

In bond-based peridynamic theory, the bond force vector is parallel to the instant direction of the bond, and the magnitude is a pairwise function:

$$f\left[X\right]\left\langle \xi \right\rangle = f\left(x,x'\right)\cdot M = -f\left[X'\right]\left\langle -\xi \right\rangle. \tag{17}$$

In ordinary state-based peridynamic theory, the direction of the force vector state is parallel to the instant direction of the bond, but the magnitude of the force from X to X' can be different from X' to X:

$$T\left[X\right]\left\langle X'-X \right\rangle = t\left(x,x'\right)\cdot M, \tag{18}$$

$$f\left[X\right]\left\langle \xi \right\rangle = t\left(x,x'\right)\cdot M - t\left(x',x\right)\cdot M'. \tag{19}$$

In non-ordinary state-based peridynamic theory, the direction of the force vector state is not parallel to the instant direction of the bond and the magnitude of the force from X to X' can be different from X' to X:

$$T\left[X\right]\left\langle X'-X \right\rangle \neq t\left(x,x'\right)\cdot M, \tag{20}$$

$$\left|T\left[X\right]\left\langle X'-X \right\rangle\right| \neq \left|T\left[X'\right]\left\langle X-X' \right\rangle\right|. \tag{21}$$

The relation of bond-based, ordinary state-based and the non-ordinary state-based peridynamic models are compared in Fig. 3.

Recently, other physical states (i.e., heat flux state, chemical concentration state, etc.) have been introduced and applied with success to model discontinuous field problems. In Section 3, some major fields of applications are shown related to the present concept.

1.3 Damage Evolution and Crack Propagation

In peridynamics, material damage is modelled by the bond failure between pairs of particles. Once a bond is broken, the interaction between particles provided by that bond will no longer exist during the rest of the analysis. The damage index $\varphi(X,t)$ has been suggested to measure the relation of damaged bonds and active bonds for any given particles.

$$\varphi\left(X,t\right) = 1 - \frac{\int_{\mathcal{H}_X} \mu\left(\xi,t\right) dX'}{\int_{\mathcal{H}_X} dX'}, \tag{22}$$

and

$$\mu\left(\xi,t\right) = \begin{cases} 1 & \text{if the bond is active} \\ 0 & \text{if the bond is broken} \end{cases}. \tag{23}$$

This is based on Eq. (23), $0 \le \varphi(X,t) \le 1$, where 0 represents the undamaged state and 1 represents the breakage of all the bonds of a given particle. The damage parameter $\mu(\xi, t)$ is used only to specify whether a bond is active or broken. The influence function $\omega(X,X')$ will equal to zero when $\mu(\xi,t)$ equals to zero.

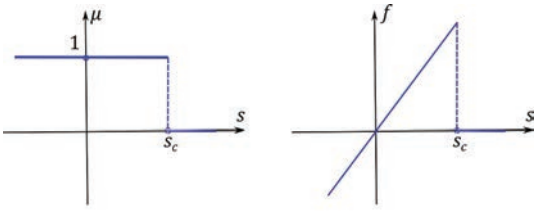

Fig. 4. *The damage model of peridynamics: a) The damage parameter-strain function, b) The force-strain function*

This condition ensures that damaged bonds are excluded from the calculation of the equation of motion in the case of bond-based peridynamics, or they can be excluded during the calculation of deformation gradient tensor F and shape tensor K

and that the resulting force state $T[X]<\xi>$ is set to 0 at damaged bonds.

For isotropic brittle materials, based on energy release rate equivalency of CCM and PD, Silling and Askari [13] derived the critical stretch for bond failure as

$$s_c = \sqrt{\frac{5 \cdot G_0}{9 \cdot k \cdot \delta}}, \tag{24}$$

where, G_0 is the fracture energy of the material. The simplest damage parameter-strain and force-strain functions are shown in Fig. 4.

The disadvantage of the above, naive criteria is that, for some materials, it is an oversimplification. Conversely, using this approach, the complete PD fracture mechanics may be defined without the necessity of strain and stress concepts.

If the critical stretch for the failure of a given bond is dependent on conditions in all other bonds or the orientation of the bond, then a more sophisticated PD model is necessary. For anisotropic (composite) materials, Shang et al. [14] advised the introduction of multiple failure conditions, dependent on the end positions of the specified bond. In their article, the bond failure criteria correspond to mechanical stress components (calculated based on peridynamic force state) through the combination of "Maximum stress" and "Hashin" failure criteria of damage mechanics of composites.

If the energy release rate equivalency is too complicated or such traditional failure criteria cannot be adopted, then the critical stretch parameters can be obtained using experimental methods [15] and [16] or calibration using an inverse approach [17].

In concurrent methods (X-FEM, meshless methods), maintaining the crack geometry is a dedicated problem. To couple the chosen numerical solver with the level set method to follow the evolution of the crack is the most popular way to solve the above problem. This coupling is very robust (fast and stable), but the descriptions of crack initiation, branching or fragmentation are open research areas. Additionally, the crack-tip kinematics has to be controlled with artificial criteria [3]. Controversially, crack initiation, propagation (or complete fragmentation) in PD framework, using of any additional database on crack geometry is not necessary: peridynamic bond activity delivers the solution. Orientation and speed of the crack tip are also determined by the bond damage evolution. (e.g. [18] to [20])

In a paper by Zhao et al. [21], the crack propagation of double-notched and double-centre crack specimens were studied. Comparing X-FEM and peridynamics, PD is more computation consuming, and the numerical stability is an open question [22]. To improve the efficiency of PD, additional efforts are usually necessary. The related results are summarized in Section 2.3.

In the detailed review by Diehl et al. [23], PD and experimental results were collected and compared based on 39 publications. The abilities of PD for wave propagation simulation were compared on four common experiments and on crack propagation problems was compared on five such experiments. Both the wave analysis and the crack geometry and velocity analysis of crack tip during dynamic loading show excellent accuracy with experimental results.

1.4 Evaluation of Boundary Conditions

In primal problems of classical continuum mechanics, mechanical problems are usually defined by a boundary value problem containing the governing partial differential equations, Eqs. (25) to (27), the essential, Eq. (28), and the natural, Eq. (29), boundary conditions (BC). These equations are valid only in the linearized theory of small displacements. The essential BCs are the constraints on a subregion of the body surface. The natural BCs are the surface tractions (or free surface) of the adjoint subregion of the body surface. The relation between the surface traction, the mechanical stress, and the partial derivatives of the displacement field are essential.

$$\rho \cdot \ddot{u} = \nabla \sigma + b, X \in V, \tag{25}$$

$$\sigma = \sigma(\varepsilon) \quad \text{or} \quad \dot{\sigma} = \dot{\sigma}(\varepsilon, \dot{\varepsilon}, \ldots), \tag{26}$$

$$\varepsilon = \frac{1}{2} \cdot (\nabla \otimes u + u \otimes \nabla), \tag{27}$$

$$u = u_0, \quad X \in S_u, \tag{28}$$

$$\sigma \cdot n = t, \quad X \in S_t. \tag{29}$$

In peridynamic theory, the governing Eq. (1) is an integro-differential equation containing the time derivative and spatial integral of the displacement field. The direct evaluation of essential boundary condition in peridynamics is easily possible. It is worth mentioning that, during the numerical solution of peridynamic problems, to avoid the appearance of artificial bond failures near the essential boundary conditions, the failure mechanism has to be forbidden [13].

The evaluation of natural boundary conditions in a peridynamic framework is not trivial. Observing the theory of peridynamics, it is clear that a complete

framework is built and that deformation, crack initiation, and propagation of a peridynamic body can be determined without the introduction and using the concept of spatial derivatives. The concept of surface traction is incompatible with the usual theory of peridynamics [10].

Considering the literature, three methods are developed to enforce natural boundary conditions: (1) in article of Le and Bobaru [24], using an (inner or artificial extern) boundary layer, the surface traction can be transformed to an artificial volumetric load. The thickness of the boundary layer is suggested as being equal to the peridynamic horizon. (2) By the articles [25] and [26], in correspondence (non-ordinary) state-based peridynamics, using the approximation of strains, the stress tensor and the surface traction can be enforced directly. (3) Huang [27] recommends the modification of the equation of motion to take the local interactions into account to evaluate the surface traction. The first method is very popular in the numerical solution of bond-based and native (non-correspondence) problems. In problems of correspondence peridynamics, almost solely the second method can be found. The third method is very new and promising, although it has not been widely applied yet.

The enforcement of contact conditions between solids leads to strongly non-linear equations, because of the changing boundary conditions on the solid surfaces. In traditional computational methods (FEM, Meshless), depending on the magnitude of the displacements and the complexity of the behaviour (material, geometry, surface conditions), there are usual methods of discretization (from "node to node" to "surface to surface" discretization) and to find the contacting surface between loaded bodies (penalty, Lagrange multipliers and augmented Lagrange methods).

In peridynamics, similarly to particle methods, the surface of the body is not modelled. For modelling contact conditions, extraordinary efforts are necessary. In the recent literature, only a few articles deal with this problem. Most applications contain peridynamic-rigid interactions inheriting contact models of particle methods. [28] The first dedicated article on this topic [29] deals with the contact of peridynamic and finite element models. An inverse isoparametric mapping technique and a node-to-surface contact algorithm are customized and implemented, and a penalty method enforcing displacement constraints is then incorporated for the transient analyses using the explicit time integration. Good agreement between numerical simulations and the analytical model is observed in the analysis of the residual velocities. The physical process of perforation is captured accurately in the simulations. In a recent paper [30], a new state-based (SB) non-local friction model was developed and compared with a bond-based (BB) contact model. The properties of various peridynamic contact models were demonstrated by applying them in finite element and meshfree peridynamic analyses of benchmark problems and an impact/penetration test. The BB model was computationally efficient and accurate to model Coulomb-friction but did not satisfy the physical principles of objectivity and balance of angular momentum. The SB model was physically correct and accurate to model Coulomb-friction, but the efficiency was less satisfactory.

1.5 Concepts of Convergence

Previously, the main concepts and definitions of the peridynamic material model were introduced. Some aspects of the relationship between the classical and peridynamic model were mentioned, but from the application point of view, one of the most important questions is the convergence abilities of the model.

The non-local nature of the peridynamic model allows the definition of the concept of convergence in different ways. On the one hand, it is worthwhile to observe the behaviour of the analytical solution of the peridynamic problem when the material horizon δ converges to zero. On the other hand, the convergence of the discretized model is also highly important.

The first aspect was studied in article [31] by Silling et al. This paper addresses the question of whether the peridynamic model for an elastic material reproduces the classical local model as this length scale approaches zero. If the motion, constitutive model, and any inhomogeneities are sufficiently smooth, then the peridynamic stress tensor converges to this limit to a Piola-Kirchhoff stress tensor that is a function only of the local deformation gradient tensor, similarly as in the classical theory. This limiting Piola-Kirchhoff stress tensor field is differentiable, and its divergence represents the force density due to internal forces. The limiting, or collapsed, stress-strain model satisfies the conditions in the classical theory for angular momentum balance, isotropy, objectivity, and hyperelasticity, provided the original peridynamic constitutive model satisfies the appropriate conditions.

The convergence behaviour of peridynamics were studied in article [32] in which Mikata proved the δ-convergence of elastic PD model to classical continuum model in case studies of statics (peristatics) and dynamics (peridynamics). He studied the wave

dispersion abilities of the peridynamic model and, in the case of finite material horizon δ, found an interesting difference to CCM: some peridynamic materials can have negative group velocities in certain regions of wavenumber.

The second numerical aspect was studied in articles **[33]** and **[34]**. Considering a one-dimensional (1D) peridynamic bar with an equidistant Δx set of nodes, the region $[x-\delta, x+\delta]$ contains $2m+1$ number of nodes, where $m = 2\delta \div \Delta x$ and $\div$ is the integer division operator. Based on this discretization, three types of convergency can be defined:

- The m-convergence: δ is fixed and $m \to \infty$. By the results of the article, the numerical peridynamic approximation converges to the exact non-local peridynamic solution for the given δ.
- The δ-convergence: $\delta \to 0$ and m is fixed or increases but at a slower rate. (The number of nodes in the material horizon is fixed.) By the results, in this case, the numerical peridynamic approximation converges to an approximation of the classical solution almost everywhere. The larger m is, the closer this approximation becomes. The convergence is not guaranteed to be uniform.
- The (δm)-convergence: $\delta \to 0$ and m increases with decreasing δ with a higher rate than the δ goes to zero. In this case, we will see that the numerical peridynamic approximation converges to the analytical peridynamic solution and converges uniformly to the local classical solution, almost everywhere.

The results of standard numerical methods in fracture modelling usually suffer from mesh sensitivity. One of the main goals of the peridynamic model was to solve the problem of crack initiation propagation, branching, and material fragmentation without similar drawbacks.

Henke and Shanbhag **[34]** studied the effect of the spatial position of nodes on the results in the case of simple brittle crack propagation problems. They found that the case of a regular cubic set of nodes can cause artificial crack lines along the symmetry of the set. Using centroidal Voronoi tessellation (CVT) and an irregular set of nodes, this problem can be avoided. They mentioned that getting the same accuracy with these methods requires a higher number of nodes in the material horizon; m has to be higher. Unfortunately, it increases the computational cost. Their work showed that the careful placement of nodes seems to eliminate any obvious signs of mesh sensitivity without incurring significant additional computational costs within the simulation. This is an important result because, in many cases, the added cost of generating point distributions is amortized over several simulation runs that share the same geometry. In their article, equivolumetric nodes were used, but it seems that when using improved methods of positioning and weighing peridynamic nodes, the drawbacks of mesh sensitivity and increasing computational cost can be neglected.

2 CONSTITUTIVE MODELS AND APPLICATIONS IN PERIDYNAMICS

Constitutive equations and the related material properties are adequately defined in the framework of CCM. These parameters originated in the strongly local nature of the CCM material model. The bond-force or the force state model is strongly non-local **[35]**; consequently, the material properties and their meanings are completely different. To find the relation between the two sets of properties, two methods were introduced.

In the native (or non-correspondence) methods, after analysing peridynamic kinematics and kinetics, deformation and force measures are defined. After the definition of the material model, its assumptions and the corresponding peridynamic material properties, deformation energy density is identified. Assuming equality between the classical material model and the peridynamic model through simple cases of deformation (homogenous deformation, uniaxial tension, pure shear), the relation between the material properties can be found.

In the correspondence methods, new material properties are not introduced. Instead, the peridynamic approximation of classical deformation and force measures are defined. It is demonstrated that the limits of these approximations are identical to the classical measures as the peridynamic material horizon approaches zero **[31]**. After the identification of the relationship between classical and peridynamic measures, the classical material properties can be used in peridynamic balance laws **[31]**.

To demonstrate the two strategies, the derivation of equations of peridynamic elasticity is shown in the following subsection.

2.1 Peridynamic Elasticity

In the framework of bond-based peridynamics, Emmrich and Weckner **[36]** derived the relation between the displacement field and the peridynamic force vector. In their work, the strain s and instant

direction vector e of the peridynamic bond was introduced as

$$s = \frac{|x'-x|-|X'-X|}{|X'-X|} = \frac{|X'+u'-X-u|-|X'-X|}{|X'-X|}, \quad (30)$$

$$e = \frac{x'-x}{|x'-x|} = \frac{X'+u'-X-u}{|X'+u'-X-u|}. \quad (31)$$

Assuming small deformations and linear elastic behaviour, one can introduce the pairwise potential in the deformed bond as a quadratic form of the instant relative position of the endpoints of the bond:

$$w(X,X') = \frac{1}{2}\cdot(x'-x)^T \cdot C(X,X')\cdot(x'-x), \quad (32)$$

where C is the material stiffness tensor

$$C = \frac{c}{|\xi|^3}\cdot(\xi)\otimes(\xi). \quad (33)$$

Based on the equivalency of deformation energy of CCM and BB-PD material under simple deformation cases, the material property c can be calculated as

$$c = \frac{18\cdot k}{\pi\cdot\delta^4} \text{ in three dimensional,} \quad (34)$$

$$c = \frac{72\cdot k}{5\cdot\pi\cdot\delta^3} \text{ in two dimensional,} \quad (35)$$

$$c = \frac{18\cdot k}{5\cdot\pi\cdot\delta^2} \text{ in one dimensional problems,} \quad (36)$$

where k is bulk modulus of the material.

The peridynamic pairwise force f was written as the derivative of the elastic potential by the relative displacement:

$$f = \frac{\partial w}{\partial(u'-u)} = C\cdot(u'-u). \quad (37)$$

One of the greatest drawbacks of the original bond-based elastic model is the limited value of Poisson's ratio **[37]**. Similar to Navier's central force elastic model, Poisson's ratio of the bond based peridynamic material is $\nu = 1/4$ in spatial and $\nu = 1/3$ in planar problems. In many practical cases, this limitation is acceptable (e.g., crack propagation of concrete structures **[38]** and **[39]**), but such an approximation is unacceptable in many engineering applications.

Despite the limited value of the Poisson's ratio, BB-PD has been applied with success in fracture mechanics of brittle materials **[20]**, **[38]**, **[40]**, and other fields (see details in following subsections), from its beginning until recently. The original theory was analysed and compared with other fracture mechanics related methods, **[18]**, **[40]** and **[41]**, and it was modified to overcome the Poisson's ratio limitation **[38]** and **[42]** to **[46]**.

As noted in Section 1.2, the shortcomings of BB-PD led to the conception of the more generalized state-based peridynamics theory. The kinematics of deformation in the neighbour of a material point X is written by the deformation state, $\mathcal{Y}$. In case of elastic behavior, the specific strain energy function depends on this quantity, $W = W(\mathcal{Y},t)$. Similar to the previous paragraph of BB-PD, in case of small displacements, the force state T is

$$T = \mathbb{C}\bullet\mathcal{U}. \quad (38)$$

The elements of the modulus state $\mathbb{C}$ can be written as second derivative of the strain energy destiny:

$$\mathbb{C} = \nabla_{\mathcal{Y}}\nabla_{\mathcal{Y}}W(\mathcal{Y})\big|_{\mathcal{Y}=\mathcal{X}}. \quad (39)$$

According to Aguiar **[47]**, relations between material properties of classical homogeneous isotropic linear elastic materials and elastic peridynamic materials are given more specifically. In the reference configuration, the reference direction $e_r\langle\mathcal{X}\rangle$ and angular state $e_n\langle\mathcal{X},\mathcal{X}'\rangle$ can be defined, respectively as:

$$e_r\langle\mathcal{X}\rangle = \frac{\mathcal{X}}{|\mathcal{X}|}, \quad (40)$$

$$e_n\langle\mathcal{X},\mathcal{X}'\rangle = \frac{\left(1-e_r\langle\mathcal{X}\rangle\otimes e_r\langle\mathcal{X}\rangle\right)\cdot e_r\langle\mathcal{X}'\rangle}{sin(\alpha)}, \quad (41)$$

and α is the smallest angle between the two observed bonds $\mathcal{X}$ and $\mathcal{X}'$.

Introducing the difference displacement ratio state by

$$h = \frac{\mathcal{U}}{|\mathcal{X}|}, \quad (42)$$

the linear and shear strain states can be defined as

$$\varepsilon = e_r\cdot h, \quad (43)$$

$$\gamma\langle\mathcal{X},\mathcal{X}'\rangle = \frac{1}{2}\cdot\left(e_n\langle\mathcal{X},\mathcal{X}'\rangle\cdot h\langle\mathcal{X}\rangle + e_n\langle\mathcal{X}',\mathcal{X}\rangle\cdot h\langle\mathcal{X}'\rangle\right). \quad (44)$$

Using these deformation states and reduced quadratic form of free energy function of an isotropic simple elastic material **[48]**, yields

$$W[h]=\int_{\mathcal{H}_X}\int_{\mathcal{H}_X}\omega(\mathcal{X}',\mathcal{X}'')\cdot \left[\begin{array}{l}\frac{\alpha_{11}}{2}(\varepsilon')^2+\alpha_{12}\cdot\varepsilon'\cdot\varepsilon''+\\ +\frac{\alpha_{33}}{2}(\gamma''')^2+\alpha_{13}\cdot\gamma'''\cdot\varepsilon'\end{array}\right]dX''dX', \quad (45)$$

where $\omega(\cdot,\cdot)$ is a given symmetric weight function and α_{11}, α_{12}, α_{13} and α_{33} are elastic peridynamic constants. Assuming equivalency between the elastic strain energy of classical Hookean material and the peridynamic elastic material, the relation of classical material properties and peridynamic material constants are

$$\alpha_{11}=\frac{5\cdot\mu}{m^2},\ \alpha_{12}=\frac{9\cdot\kappa-5\cdot\mu}{2\cdot m^2},\ \alpha_{33}=\frac{20\cdot\mu}{m^2}, \quad (46)$$

where the constant m is defined by

$$m=4\cdot\pi\cdot\int_0^{\delta}\omega(\rho)\cdot\rho^4 d\rho. \quad (47)$$

The remaining constant α_{13} is the coupling constant in elastic strain energy between linear and angular strains. A similar material property is not available in classical elasticity. Assuming a finite peridynamic horizon if the quadratic free energy function of the material is given, then the value of α_{13} can be determined from Eq. (45). In this sense, the material property α_{13} means a correction to compensate the effect of finite peridynamic horizon.

An alternative method to determine the state-based peridynamic material constants is to decompose the deformation state to dilatation and deviatoric terms. Silling et al. **[12]** and Madenci and Oterkus **[49]** followed slightly different ways during this decomposition and achieved different results.

In Silling's work the force state is

$$T[X]\langle\xi\rangle=M[X]\langle\xi\rangle\cdot\left(\frac{3\cdot k}{m}\cdot\omega\cdot\mathcal{X}\cdot\theta+\frac{15\cdot\mu}{m}\cdot\omega\cdot e^d\right), \quad (48)$$

where k and μ are the bulk and shear modulus, respectively. The scalar reference and extension state are defined, respectively:

$$\mathcal{X}=|\mathcal{X}|, \quad (49)$$

$$e(\mathcal{Y})=|\mathcal{Y}|-|\mathcal{X}|. \quad (50)$$

Weighted volume has to be introduced:

$$m=(\omega\cdot\mathcal{X})\bullet\mathcal{X}. \quad (51)$$

The dilatation- and deviatoric extension states are defined over the scalar extension state as:

$$\theta(\mathcal{Y})=\frac{3}{m}\cdot(\omega\cdot\mathcal{X})\bullet e(\mathcal{Y}), \quad (52)$$

$$e^d(\mathcal{Y})=e(\mathcal{Y})-\frac{\theta(\mathcal{Y})\cdot|\mathcal{X}|}{3}. \quad (53)$$

In Madenci's work

$$T[X]\langle\xi\rangle=2\cdot\delta\cdot M[X]\langle\xi\rangle\cdot\left(a\cdot\frac{\mathcal{Y}\cdot\mathcal{X}}{|\mathcal{Y}|\cdot|\mathcal{X}|}\cdot\theta+b\cdot\frac{|\mathcal{Y}|-|\mathcal{X}|}{|\mathcal{X}|}\right). \quad (54)$$

The dilatation-state in this context was:

$$\theta(\mathcal{Y})=d\cdot\delta\cdot\int_{\mathcal{H}_X}\frac{|\mathcal{Y}|-|\mathcal{X}|}{|\mathcal{X}|}\cdot\frac{\mathcal{Y}\cdot\mathcal{X}}{|\mathcal{Y}|\cdot|\mathcal{X}|}dX'. \quad (55)$$

The constants a, b and d in the above expressions were:

$$a=\frac{3\cdot k-5\cdot\mu}{2},\quad b=\frac{15\cdot\mu}{2\cdot\pi\cdot\delta^5},\quad d=\frac{9}{4\cdot\pi\cdot\delta^4}. \quad (56)$$

In articles and book by Madenci and Oterkus **[49]**, and **[50]**, the elastic peridynamic material properties were also analysed. In their works, the peridynamic states defined above were applied on a set of discrete material points.

Van Le and Bobaru **[51]** showed that the applicability of the above results is limited. Madenci's model is valid only in the case of small strains and infinitesimal rotations; Silling's model is valid in case of small strains and finite rotations **[51]**; Van Le has not found a valid peridynamic model for the case of finite strain and finite rotation deformations.

Using the approach of the above methods, in the applications, the concepts of strain and stress are not necessary. In the literature, this type of approach is referred to as a native or non-correspondence peridynamic model.

As mentioned, with the second method, the introduction of peridynamic material properties is not necessary. The peridynamic approximation of the displacement gradient can be written as

$$\nabla u=(\mathcal{U}*\mathcal{X})\cdot K^{-1}. \quad (57)$$

The approximating engineering strain tensor and the stress tensor are

$$\varepsilon=\frac{1}{2}\cdot(\mathcal{U}*\mathcal{X}+\mathcal{X}*\mathcal{U})\cdot K^{-1}, \quad (58)$$

$$\sigma=C\cdot\varepsilon. \quad (59)$$

Using Eq. (7) of expanded vector state, the peridynamic force state is:

$$T\left[X\right]\left\langle \xi \right\rangle = \omega\left(\left|\xi\right|\right)\cdot\sigma\cdot K^{-1}\cdot\xi. \tag{60}$$

Substituting Eq. (60) into the equation of motion, Eq. (13):

$$\rho\cdot\ddot{u} = \int_{\mathcal{H}_X}\omega\left(\left|\xi\right|\right)\cdot\sigma'\cdot K'^{-1}\cdot\xi' dX' - \\ -\int_{\mathcal{H}_X}\omega\left(\left|\xi\right|\right)\cdot\sigma\cdot K^{-1}\cdot\xi dX' + b\left(X\right). \tag{61}$$

The correspondence peridynamic model has the ability to describe large displacement, rotation, and deformation problems – theoretically. In numerical applications, some stability issues of this method were reported. Recently, several stabilization methods have been suggested for the original correspondence model **[22]** and **[52]** to **[54]**, but this area still has some open questions and challenges.

Parallel to the development of a peridynamic model for three-dimensional elastic bodies, the research of other special fields of elasticity appeared in the peridynamic literature. Silling and Bobaru **[55]**, used peridynamics to model the behaviour of rubberlike membranes and fibres. Gerstle et al. **[38]** introduced the micropolar bond-based peridynamics and used it to solve plane stress problems of concrete structures. With the micropolar model, one can avoid the drawback of fixed Poisson's ratio anomaly of bond-based peridynamics. Kilic et al. **[56]** published the first article about the peridynamics of composite laminates. They modelled the effect of fibre orientation on the crack propagation in planar composites. Oterkus et al. proved the validity of peridynamic theory through qualitative and quantitative comparisons against the test results for a stiffened composite curved panel with a central slot under combined internal pressure and axial tension **[15]**. The crack propagation of composite laminates under dynamic (impact and explosive) loads was modelled by peridynamics **[19]** and **[57]**. The peridynamic predictions correlated well with the experimental results available in the literature. Crack propagation in ceramic matrix composites **[58]** and in fibre-reinforced composites **[59]** was modelled using the peridynamic framework.

State-based peridynamics of beams was developed **[60]** to solve the problem of the Euler-beam. Yang et al. formulated the peridynamic theory of functional graded Thimosenko-beam **[61]**. The validation of the model was proven by testing different boundary conditions and loads. The results showed good agreement with analytical and finite element results.

2.2 The State-Based Peridynamic Plasticity

Although plasticity can be included in the bond-based theory by permitting permanent deformation of individual bonds **[62]**, this results in permanent deformation of a material undergoing volumetric strain (without shear). Metal forming experiments have suggested volumetric incompressibility of plastic deformation. It means that only shear deformations can induce plastic response **[63]**. Consequently, the bond based peridynamic model, in its original form, cannot describe the plastic deformation of metals.

In the work of Mitchell **[64]** and Littlewood et al. **[65]**, the ordinary state-based (non-correspondence) peridynamics was used to model elasto-plasticity and viscoplastic behaviour. The first paper is a theoretical foundation of PD plasticity without qualitative or quantitative results. The second publication contains a quantitative comparison between PD and experimental results.

In article of Mitchell **[64]**, PD plasticity was defined over continuous sets of points, using integral forms and Frechet-derivatives. In the article of Madenci and Oterkus, a discretized set of points was used to introduce inelasticity **[50]**.

Plastic deformation, in the case of most metals, is independent of volumetric deformation and hydrostatic pressure. To separate the hydrostatic effects from shear effects, the decomposition of deformation state is required to volumetric and deviatoric part. Using Eqs. (52) and (53), the deformation state can be decomposed to dilatation θ and deviatoric e^d terms. Using this assumption, the plastic deformation depends only on the second term of Eq. (48). The deviatoric part of the deformation extension state can be decomposed to elastic e^{de} and plastic e^{dp} parts:

$$e^d = e^{de} + e^{dp}. \tag{62}$$

Hence, the rate form of the balance Eq. (48) is

$$\dot{t} = \frac{3\cdot k}{m}\cdot\omega\cdot\mathcal{X}\cdot\dot{\theta} + \frac{15\cdot\mu}{m}\cdot\omega\cdot\left(\dot{e}^d - \dot{e}^{dp}\right). \tag{63}$$

Following the way of classical plasticity **[66]**, a perfectly plastic flow rule, consistency parameter (λ) and Kuhn-Tucker conditions were derived. Based on these quantities and relations, through linearization of the deformation and force states, the implicit time integration of the plastic model was developed.

The peridynamic yield function f of perfectly plastic material is

$$f\left(t^d\right) = \psi\left(t^d\right) - \psi_0 \le 0. \tag{64}$$

The relationship between the peridynamic yield condition ψ_0 and yield stress of the classical material model is

$$\psi_0 = \frac{75}{8 \cdot \pi} \cdot \frac{E_y^2}{\delta^5}, \tag{65}$$

where E_y is usually measured in uniaxial $E_y = \frac{\sigma_1}{\sqrt{3}}$ or pure shear $E_y = \sigma_{12}$ stress conditions.

Later, in the article [50], peridynamic plastic deformation according to the von Mises yield criterion with isotropic hardening was also developed.

Stefanelli et al. [67], in the framework of non-local vector calculus, analysed the solution of the peridynamic elasto-plastic problem. The existence and convergence to the CCM solution were proved. Based on this and other non-local vector calculus (NLVC) related publications, one can assume that the NLVC could be a pillar of the generalized, robust mathematical background behind the peridynamic theory.

The correspondence peridynamic model was first applied on viscoplasticity by Foster et al. [68]. Littewood reported a plastic localization model using peridynamics [65]. Sandia National Laboratories announce "Sandia Fracture Challenges", in every second year, with more and more challenging problems to predict material damage and crack propagation in ductile materials. State-based peridynamic solutions are often submitted, the results are published. and the accuracy of SB-PD is improving, but acceptable [69] to [71].

2.3 Relation of Peridynamics with Classical and Experimental Results

Out of the nearly 500 referred articles of peridynamics published in the previous two decades, 40 are related to damage, 124 are about fracture, and 70 are crack-related articles. On some fields of applications, only a few papers were published, although other fields were more fruitful (Table 1).

Topics with few publications are those for which the authors mostly only develop the PD framework of the specified problem and prove the capability of peridynamics to simulate the phenomena on some essential problems. On the more studied areas, usually the formulation of PD is better established and (next to the essential problems) more real world applications can be found. Here we would like to highlight only a few application areas where peridynamics have been successfully applied.

The most frequent research area in peridynamics is fracture mechanics. In applications, the comparability and relation between the classical and the PD material models are essential. The relation between peridynamics and material properties of classical fracture mechanics has been widely studied. The peridynamic non-local J-integral has also been thoroughly analysed in [72] and [24]. The displacement-based J-integral formulation, developed in [73], can be obtained with bond-based or state-based peridynamic models. In the article of Panchadhara and Gordon [74], a new peridynamic stress intensity factor (SIF) was introduced. This quantity enables peridynamics an effective way of replacing the more or less ad-hoc fracture criteria to motivate fracture initiation and direction of fracture propagation in conventional numerical techniques of fracture mechanics. It was proved that the peridynamic SIF used in conventional numerical methods improves the robustness of the solution. Furthermore, peridynamic SIFs may be applied to study complex fracture physics, such as the branching and interaction of stress waves with propagating fractures that would otherwise be difficult using conventional numerical methods.

Table 1. *Number of papers on the fields of PD applications*

Field of application	Number of published papers
Elasticity	23
Heat conduction, Thermoelasticity	12
Fluid transport and porose material	1
Plasticity	15
Damage	10
Fracture	76
Fatigue	9
Structural Stability	1
Corrosion and chemical damage	4
Electricity	4
Multiscale problems	2
Phase transformation	2
Technology and manufacturing	4

The most frequent research area in peridynamics is fracture mechanics. In applications, the comparability and relation between the classical and the PD material models are essential. The relation between peridynamics and material properties of classical fracture mechanics has been widely studied. The peridynamic non-local J-integral has also been thoroughly analysed in [72] and [24]. The displacement-based J-integral formulation, developed in [73], can be obtained with bond-based or state-based peridynamic models. In the article of Panchadhara and Gordon [74], a new peridynamic stress intensity

factor (SIF) was introduced. This quantity enables peridynamics an effective way of replacing the more or less ad-hoc fracture criteria to motivate fracture initiation and direction of fracture propagation in conventional numerical techniques of fracture mechanics. It was proved that the peridynamic SIF used in conventional numerical methods improves the robustness of the solution. Furthermore, peridynamic SIFs may be applied to study complex fracture physics, such as the branching and interaction of stress waves with propagating fractures that would otherwise be difficult using conventional numerical methods.

The linear elastic and later hyperelastic extension models were applied to describe the crack propagation phenomena in homogenous and heterogenic bodies of 3-D or 2-D (plane stress/strain) geometries [15] and [75]. The problem of tearing and crack propagating in shells and fibres were also solved with promising qualitative results [55]. These papers demonstrated the ability of PD in this field through different problems with visualized results but did not contain quantitative data comparable with the results of classical analytic or numerical methods.

O'Grady and Foster published the NOSB-PD model of a Kirchoff-Love plate. [37] In their paper, the simple bent square plates with different boundary conditions were studied and compared with analytical solutions. The δ-convergence of transverse displacements of the applied model was shown. A demonstration of brittle fracture in a bending (double torsion) plate showed the potential of this model to broaden the class of problems that can realistically be modelled using peridynamics.

Chowdhury et al. derived the PD formulation of thin and thick curved plates under the assumptions of linear elasticity. [76] Their proposal on the peridynamic shell theory is numerically assessed against simulations on static deformation of spherical and cylindrical shells, that of flat plates and quasi-static fracture propagation in a cylindrical shell.

Recently, based on a more general SB-PD model, the complete Reissner-Mindlin shell theory was adapted to the peridynamic framework, and validity was proven through several numerical problems of continuous and damaged, discontinuous thick shells [77]. The tested models (containing attractively low PD nodes) were compared to the analytical and FEM results and showed excellent accuracy in the cases of small and large displacements/deformations.

Crack initiation, propagation, and bifurcation were modelled in the framework of PD in multilayer structures [78] and composite laminates [56], [19], [57] and [79] under thermal and dynamic loads. Mechanical damage was modelled in impact loaded layered glass [80], tensioned hydrated cement paste [81] and glass-polycarbonate-glass layered structure [59] by BB-PD. Also, a modified BB-PD was used to model dynamic fracture in functionally graded materials [82]. The results of PD models were compared with different experimental setups. The capability of peridynamics to simulate different damage modes of multilayer and composite structures were proven. The main advantage of PD against other existing models is the ability to identify all of the failure modes without simplifying assumptions. Damage is inherently calculated in a PD analysis without special procedures, making progressive failure analysis more practical. The price for this completeness is the necessity of severe PD nodes (each layer of composite has its own set of nodes and bonds are defined in plane and in transverse directions) and the time-consuming computations.

The BB-PD model of heat transfer was introduced by Bobaru and Duangpanya [83]. Using the concept of very simple and intuitive thermal-bond, 1-D transient heat conduction was simulated under different boundary conditions. - and -convergence of the model were observed. Both converged to the analytic solutions.

Fully coupled OSB-PD thermo-elasticity was developed by Oterkus et al. [84]. The derivation of the governing equations was based upon thermodynamic considerations. The capability of a PD model was tested and proved on simple 1-D and 3-D convergence studies to analytic, FEM and BEM results. In their paper, practical problems were not studied.

Thermo-mechanically induced damage and fracture in viscoelastic solids was simulated using OSB-PD by Madenci and Oterkus. The deformation analysis successfully captured the relaxation behaviour of the material. The numerical results concerned first the verification problems and subsequently, a double-lap joint with a viscoelastic adhesive where failure nucleates and grows.

The very complex thermo-plastic material behaviour was simulated in the framework of NOSB-PD by Amani et al. [86]. The Johnson-Cook constitutive and damage models were used. Two experimental configurations (Taylor-bar impact test (TBIT) and Kalthoff–Winkler test (KWT)) were simulated and compared. The numerical results agreed well with the available experimental data, instead of the moderate number of peridynamic nodes (5400 in TBIT and 60291 in KWT).

Recently, thermo-mechanically induced fracture was also analysed in peridynamics [87]. This paper

presented an effective way to use a variable grid size in a weakly coupled thermo-mechanical peridynamic model. The proposed numerical method was equipped with a stretch control criterion to transform the grid discretization adaptively. Hence, the fine grid spacing was only used in limited zones where it was required. The computation time using the adaptive method was less than one third of the original fine grid. Predicting complex crack patterns without any a priori hypothesis on cracks is automatic in this model.

3 CONCLUSIONS

Aiming to highlight findings that are concerned with theory and applications of a new, strongly non-local method of continuum mechanics – peridynamics – foundations of the method are reviewed while seeking new paths in future developments.

In peridynamics, the advantages of classical continuum mechanics and molecular dynamics are alloyed (especially in the field of fracture mechanics) based on the theory and work of Silling. It was found that the nonlocality of peridynamics plays a significant role in the ability to simulate crack propagation, branching, and coalescence in brittle materials. Peridynamics was shown to describe the above phenomena without any artificial conditions of crack-tip velocity with excellent accuracy to experimental data in plenty of standardized and "real-world" configurations. Using the overview of the works published in the recent decades, directions for future developments are identified in four paths:

(1) Applying peridynamics in non-linear and ductile fracture mechanics possess broad potential. Combining peridynamics and ductility is challenging, and the usual explicit solvers of peridynamics are not sufficiently effective. The development of implicit and/or more effective explicit solvers is needed.

(2) Numerical stability issues were observed in large deformation peridynamics, and only a few authors have dedicated their work to these problems. The relation between the meshless methods and the peridynamics is established. Based on this fact, the introduction of higher-order peridynamics may provide a solution to these stability issues.

(3) Analysis of numerical stability, robustness, and efficiency of peridynamics are also research directions that may require more focus in the coming years. The peridynamics are very accurate, but the speed and efficiency in "industrial problems" are lower than the concurrent methods, such as Extended-FEM or meshless methods. Coupling of PD with these methods is very efficient **[16]** and **[88]** to **[90]** and, as an alternative solution the parallel computing (e.g. supercomputers or GPGPU), seems natively applicable in peridynamics, which could increase the speed and efficiency of the method **[91]** to **[93]**.

(4) It has also been noticed that there is an emerging number of coupled multiphysical and multidisciplinary works. In the case of successful implementation of peridynamics on mechanics of large deformation of solids, the research of separation (crack propagation) or merging of soft tissue would initiate and open opportunities for further biomechanical and other biophysical applications.

4 ACKNOWLEDGEMENTS

The authors would like to thank the financial support for publication by Project no. 2020-4.1.1-TKP2020, which has been implemented with the support provided by the Ministry of Innovation and Technology of Hungary from the National Research, Development and Innovation Fund, financed under the TKP 2020 funding scheme.

5 REFERENCES

[1] Milne, I., Ritchie, R. O., Karihaloo, B. (2007). *Comprehensive Structural Integrity*, Elsevier Science, New York.

[2] William T. B.; Roch J. S. (2010). *ASM Handbook - Failure Analysis and Prevention*, vol. 11, ASM International, New York.

[3] Sun, C. T., Jin Z. H. (2012). *Fracture Mechanics*, Elsevier, Berlin.

[4] Lemaitre, J., Desmorat, R. (2005). *Engineering Damage Mechanics*, Springer, Berlin.

[5] Baaser, H., Gross, D. (2003). Remarks on the use of continuum damage models and on the limitations of their applicability in ductile fracture mechanics. Baaser, H., Hutter, K. (eds.), *Deformation and Failure in Metallic Materials*, Springer, Berlin, p. 345-362, **DOI:10.1007/978-3-540-36564-8_14**.

[6] Khoei, A. R. (2015). *Extended Finite Element Method: Theory and Applications*, Wiley, Oxford, **DOI:10.1002/9781118869673**.

[7] Chen, Y., Lee, J., Eskandarian, A. (2006). *Meshless Methods in Solid Mechanics*, Springer, Berlin.

[8] Huang, D., Wang, M., Lu, G. (2014). Continuum fracture analysis and molecular dynamic study on crack initiation and propagation in nanofilms. *Journal of Nano-materials*, vol. 1, p. 1-7, **DOI:10.1155/2014 /732434**.

[9] Lee, J. G. (2012). *Computational Material Science*, CRC Press, New York.

[10] Silling, S. A. (2000). Reformulation of elasticity theory for discontinuities and long range forces. *Journal of Mechanics*

and Physics of Solids, vol. 48, no. 1, p. 175-209, **DOI:10.1016/S0022-5096(99)00029-0**.

[11] Silling, S. A. (2016). Introduction to peridynamics. Bobaru, F., Foster, J. T., Geubelle, S., Silling, S. A. (Eds.) *Handbook of Peridynamic Modeling*, Chapman and Hall/CRC, New York, p. 63-98.

[12] Silling, S. A., Epton, M., Weckner, O., Xu, J., Askari, E. (2007). Peridynamic States and Constitutive Modeling. *Journal of Elasticity*, vol. 88, p. 151-184, **DOI:10.1007/s10659-007-9125-1**.

[13] Silling, S. A., Askari, E. (2005). A meshfree method based on the peridynamic model of solid mechanics. *Computers and Structures*, vol. 83, no. 17-18, p. 1526-1535, **DOI:10.1016/j.compstruc.2004.11.026**.

[14] Shang, S., Qin, X., Li, H., Cao, X. (2019). An application of non-ordinary state-based peridynamics theory in cutting process modelling of unidirectional carbon fiber reinforced polymer material. *Composite Structures*, vol. 226, **DOI:10.1016/j.compstruct.2019.111194**.

[15] Oterkus, E., Madenci, E. (2012). Peridynamic analysis of fiber-reinforced composite materials. *Journal of Mechanics of Materials and Structures*, vol. 7, p. 45-84, **DOI:10.2140/jomms.2012.7.45**.

[16] Oterkus, E., Madenci, E., Weckner, O., Silling, S. A., Bogert, P., Tessler, A. (2012). Combined finite element and peridynamic analyses for predicting failure in a stiffened composite curved panel with a central slot. *Composite Structures*, vol. 94, no. 3, p. 839-850, **DOI:10.1016/j.compstruct.2011.07.019**.

[17] Colavito, K., Kilic, B., Celik, E., Madenci, E., Askari E., Silling, S. A. (2007). Effect of void content on stiffness and strength of composites by peridynamic analysis and static indentation test. *Proceedings of the 48th AIAA/ASME/ASCE/AHS/ASC Structures, Structural Dynamics and Materials Conference*, p. 2007-2021, **DOI:10.2514/6.2007-2251**.

[18] Bobaru F., Zhang, G. (2015). Why do cracks branch? A peridynamic investigation of dynamic brittle fracture. *International Journal of Fracture*, vol. 196, no. 1, p. 59-98, **DOI:10.1007/s10704-015-0056-8**.

[19] Chaoyang, S., Zaixing, H. (2016). Peridynamic simulation to impacting damage in composite laminate. *Composite Structures*, vol. 138, p. 335-341, **DOI:10.1016/j.compstruct.2015.12.001**.

[20] Wang, Q., Wang, Y., Zan, Y., Lu, W., Bai, X., Guo, J. (2018). Peridynamics simulation of the fragmentation of ice cover by blast loads of an underwater explosion. *Journal of Marine Science and Technology*, vol. 23, no. 1, p. 52-66, **DOI:10.1007/s00773-017-0454-x**.

[21] Zhao, J., Tang, H.-S. Yue, S. (2017). Peridynamics versus XFEM: a comparative study for quasistatic crack problems. *Frontiers of Structural and Civil Engineering*, vol. 12, **DOI:10.1007/s11709-017-0434-6**.

[22] Silling, S. A. (2017). Stability of peridynamic correspondence material models and their particle discretizations. *Computer Methods in Applied Mechanics and Engineering*, vol. 322, p. 42-57, **DOI:10.1016/j.cma.2017.03.043**.

[23] Diehl, P., Prudhomme, S., Levesque, M. (2019). A Review of Benchmark Experiments for the Validation. *Journal of Peridynamic and Non-local Models*, vol. 1, p. 14-35, **DOI:10.1007/s42102-018-0004-x**.

[24] Le, Q. V., F. Bobaru, F. (2018). Surface corrections for peridynamic models in elasticity and fracture. *Computational Mechanics*, vol. 61, no. 4, p. 499-518, **DOI:10.1007/s00466-017-1469-1**.

[25] Warren, T. L., Silling, S. A., Askari, A., Weckner, O., Epton, M. A., Xu, J. (2009). A non-ordinary state-based peridynamic method to model solid material deformation and fracture. *International Journal of Solids and Structures*, vol. 46, no. 5, p. 1186-1195, **DOI:10.1016/j.ijsolstr.2008.10.029**.

[26] Wu, C. T., Ren, B. (2015). A stabilized non-ordinary state-based peridynamics for the ductile material failure analysis in metal machining process. *Computer Methods in Applied Mechanics and Engineering*, vol. 291, p. 1-40, **DOI:10.1016/j.cma.2015.03.003**.

[27] Huang, Z. (2019). Revisiting the peridynamic motion equation due to characterization of boundary conditions. *Acta Mechanica Sinica*, vol. 35, no. 5, p. 972-980, **DOI:10.1007/s10409-019-00860-3**.

[28] Littlewood, D. (2010). Simulation of Dynamic Fracture Using Peridynamics, Finite Element Modeling, and Contact. *ASME International Mechanical Engineering Congress and Exposition, Proceedings (IMECE),* vol. 9, p. 209-217, **DOI:10.1115/IMECE2010-40621**.

[29] Lee, J., Liu, W., Hong, J.-W. (2016). Impact fracture analysis enhanced by contact of peridynamic and finite element formulations. *International Journal of Impact Engineering*, vol. 87, p. 108-119, **DOI:10.1016/j.ijimpeng.2015.06.012**.

[30] Kamensky, D., Behzadinasab, M., Foster, J. T., Bazilevs, Y. (2019). Peridynamic modeling of frictional contact. *Journal of Peridynamics and Non-local Modeling*, vol. 1, p. 107-121, **DOI:10.1007/s42102-019-00012-y**.

[31] Silling, S. A., Lehoucq, R. B. (2008). Convergence of peridynamics to classical elasticity. *Journal of Elasticity*, vol. 93, p. 13-37, **DOI:10.1007/s10659-008-9163-3**.

[32] Mikata, Y. (2012). Analytical solutions of peristatic and peridynamic problems for a 1D infinite rod. *International Journal of Solids and Structures*, vol. 49, p. 2887-2897, **DOI:10.1016/j.ijsolstr.2012.02.012**.

[33] Bobaru, F., Yang, M., Alves, L. F., Silling, S. A., Askari, E., Xu, J. (2009). Convergence, adaptive refinement, and scaling in 1D peridynamics. *International Journal for Numerical Methods in Engineering*, vol. 77, p. 852-877, **DOI:10.1002/nme.2439**.

[34] Henke, S. F., Shanbhag, S. (2014). Mesh sensitivity in peridynamic simulations. *Computer Physics Communications*, vol. 185, pp. 181-193, **DOI:10.1016/j.cpc.2013.09.010**.

[35] Eringen, A. C. (2002). *Non-local Continuum Field Theories*, Springer-Verlag New York Inc., New York.

[36] Emmrich, E. and Weckner, O. (2006). The peridynamic equation of motion in non-local elasticity theory. *III. European Conference on Computational Mechanics*, p. 1-8, **DOI:10.1007/1-4020-5370-3_62**.

[37] O'Grady, J., Foster, J. T. (2014). Peridynamic plates and flat shells: A non-ordinary, state-based model. *International Journal of Solids and Structures*, vol. 51, no. 25-26, p. 4572-4579, **DOI:10.1016/j.ijsolstr.2014.09.003**.

[38] Gerstle, W., Sau, N., Silling, S. A. (2007). Peridynamic modeling of concrete structures. *Nuclear Engineering and Design*, vol. 237, no. 12-13, p. 1250-1258, **DOI:10.1016/j.nucengdes.2006.10.002**.

[39] Huang, D., Zhang, Q., Qiao, P. Z. (2011). Damage and progressive failure of concrete structures using. *Science China Technological Sciences*, vol. 54, no. 3, p. 591-596, **DOI:10.1007/s11431-011-4306-3**.

[40] Agwai, A. Guven, I., Madenci, E. (2011). Predicting crack propagation with peridynamics: a comparative study. *International Journal of Fracture*, vol. 171, no. 1, p. 65-78, **DOI:10.1007/s10704-011-9628-4**.

[41] Weckner, O., Brunk, G., Epton, M. A., Silling, S. A. Askari, E. (2009). *Comparison between local elasticity and non-local peridynamics.*

[42] Dan, H., Guangda, L. Pizhong, Q. (2015). An improved peridynamic approach for quasi-static elastic deformation and brittle fracture analysis. *International Journal of Mechanical Sciences*, vol. 94-95, p. 111-122, **DOI:10.1016/j.ijmecsci.2015.02.018**.

[43] Zhu, Q.-Z., Ni, T. (2017). Peridynamic formulations enriched with bond rotation effects. *International Journal of Engineering Science*, vol. 121, p. 118-129, **DOI:10.1016/j.ijengsci.2017.09.004**.

[44] Liu, W., Hong, J.-W. (2012). Discretized peridynamics for linear elastic solids. *Computational Mechanics*, vol. 50, no. 5, p. 579-590, **DOI:10.1007/s00466-012-0690-1**.

[45] Wang, Y., Zhou, X., Wang, Y., Shou, Y. (2018). A 3-D conjugated bond-pair-based peridynamic formulation for initiation and propagation of cracks in brittle solids. *International Journal of Solids and Structures*, vol. 134, p. 89-115, **DOI:10.1016/j.ijsolstr.2017.10.022**.

[46] Diana, V., Casolo, S. (2019). A full orthotropic micropolar peridynamic formulation for linearly elastic solids. *International Journal of Mechanical Sciences*, vol. 160, p. 140-155, **DOI:10.1016/j.ijmecsci.2019.06.036**.

[47] Aguiar, A. R. (2016). On the determination of a peridynamic constant in a linear constitutive model. *Journal of Elasticity*, vol. 122, p. 27-39, **DOI:10.1007/s10659-015-9531-8**.

[48] Aguiar, A. R., Fosdick, R. L. (2014). A constitutive model for a linearly elastic peridynamic body. *Mathematics and Mechanics of Solids*, vol. 19, p. 502-523, **DOI:10.1177/1081286512472092**.

[49] Madenci, E., Oterkus, E. (2014). *Peridynamic Theory and Its Applications*, Springer Science+Business Media New, New York, **DOI:10.1007/978-1-4614-8465-3**.

[50] Madenci, E., Oterkus, S. (2016). Ordinary state-based peridynamics for plastic deformation according to vonMises yield criteria with isotropic hardening. *Journal of the Mechanics and Physics of Solids*, vol. 86, p. 192-219, **DOI:10.1016/j.jmps.2015.09.016**.

[51] Van Le, Q., Bobaru, F. (2018). Objectivity of state-based peridynamic models. *Journal of Elasticity*, vol. 131, no. 1, p. 1-17, **DOI:10.1007/s10659-017-9641-6**.

[52] Chowdhury, S. R., Debasish, P. R., Reddy, J. (2019). A modified peridynamics correspondence principle: Removal of zero-energy deformation and other implications. *Computer Methods in Applied Mechanics and Engineering*, vol. 346, p. 530-549, **DOI:10.1016/j.cma.2018.11.025**.

[53] Breitzman, T., Dayal, K. (2018). Bond-level deformation gradients and energy averaging in peridynamics. *Journal of the Mechanics and Physics of Solids*, vol. 110, p. 192-204, **DOI:10.1016/j.jmps.2017.09.015**.

[54] Chen, H. (2018). Bond-associated deformation gradients for peridynamic correspondence model. *Mechanics Research Communications*, vol. 90, p. 34-41, **DOI:10.1016/j.mechrescom.2018.04.004**.

[55] Silling, S. A., Bobaru, F. (2005). Peridynamic modeling of membranes and fibers. *International Journal of Non-Linear Mechanics*, vol. 40, p. 395-409, **DOI:10.1016/j.ijnonlinmec.2004.08.004**.

[56] Kilic, B., Agwai, A., Madenci, E. (2009). Peridynamic theory for progressive damage prediction in center-cracked composite laminates. *Composite Structures*, vol. 90, p. 141-151, **DOI:10.1016/j.compstruct.2009.02.015**.

[57] Diyaroglu, C., Oterkus, E., Madenci, E., Rabczuk, T., Siddiq, A. (2016). Peridynamic modeling of composite laminates under explosive loading. *Composite Structures*, vol. 144, p. 14-23, **DOI:10.1016/j.compstruct.2016.02.018**.

[58] Hu, Y. L., Madenci, E. (2018). Peridynamics for fatigue life and residual strength prediction of composite laminates. *Composite Structures*, vol. 160, p. 169-184, **DOI:10.1016/j.compstruct.2016.10.010**.

[59] Ren, B., Wu, C. T., Seleson, P., Zeng, D., Lyu, D. (2018). A peridynamic failure analysis of fiber-reinforced composite laminates using finite element discontinuous Galerkin approximations. I*nternational Journal of Fracture*, vol. 214, p. 49-68, **DOI:10.1007/s10704-018-0317-4**.

[60] O'Grady, J., Foster, J. T. (2014). Peridynamic beams: A non-ordinary, state-based model. *International Journal of Solids and Structures*, vol. 51, no. 18, p. 3177-3183, **DOI:10.1016/j.ijsolstr.2014.05.014**.

[61] Yang, Z., Oterkus, E., Oterkus, S. (2021). Analysis of functionally graded Timoshenko beams by using peridynamics. *Journal of Peridynamics and Non-local Modeling*, vol. 3, **DOI:10.1007/s42102-020-00044-9**.

[62] Ladányi, G., Jenei, I. (2008). Analysis of plastic peridynamic material with RBF meshless method. *Periodica Polytechnika*, vol. 3, p. 65-77, **DOI:10.1556/Pollack.3.2008.3.6**.

[63] Lubliner, J. (2008). *Plasiticity Theory*, Dover Publications, New York.

[64] Mitchell, J. A. (2011). *A Non-local, Ordinary, State-Base Plasticity Model for Peridynamics*. Albuquerque, New Mexico and Livermore, **DOI:10.2172/1018475**.

[65] Littlewood, D., Foster, J. T., Boyce, B. (2012). *Peridynamic Modeling of Localization in Ductile Metals. Albuquerque.* New Mexico and Livermore, **DOI:AC04-94AL85000**.

[66] Simo, J. C., Hughes, T. J. R. (1998). *Computational Inelasticity*, Springer, New York.

[67] Kružík, M., Mora-Corral, C., Stefanelli, U. (2018). Quasistatic elastoplasticity via Peridynamics: existence and localization. *Continuum Mechanics and Thermodynamics*, vol. 30, p. 1155-1184, **DOI:10.1007/s00161-018-0671-5**.

[68] Foster, J. T., Silling, S. A., Chen, W. W. (2009). Viscoplasticity using peridynamics. *International Journal for Numerical Methods in Engineering*, p. 115-132, **DOI:10.1002/nme.2725**.

[69] Pack, K., Luo, M., Wierzbicki., T. (2014). Sandia fracture challenge: Blind prediction and full calibration to enhance fracture predictability. *International Journal of Fracture*, vol. 186, **DOI:10.1007/s10704-013-9923-3**.

[70] Boyce, B. L. (2016). The second Sandia Fracture Challenge: predictions of ductile failure under quasi-static and moderate-rate dynamic loading. *International Journal of Fracture*, vol. 198, no. 1-2, **DOI:10.1007/s10704-016-0089-7**.

[71] Kramer, S. L. B. (2019). The third Sandia Fracture Challenge: predictions of ductile fracture in additively manufactured metal. *International Journal of Fracture*, vol. 218, no. 1, p. 1573-2673, **DOI:10.1007/s10704-019-00361-1**.

[72] Hu, W., Ha, Y. D., Bobaru, F., Silling, S. A. (2012). The formulation and computation of the non-local J-integral in bond-based peridynamics. *International Journal of Fracture*, vol. 176, no. 2, p. 195-206, **DOI:10.1007/s10704-012-9745-8**.

[73] Stenström, C., Eriksson, K. (2019). The J-contour integral in peridynamics via displacements. *International Journal of Fracture*, vol. 216, no. 2, p. 173-183, **DOI:10.1007/s10704-019-00351-3**.

[74] Panchadhara, R., Gordon, P. A. (2016). Application of peridynamic stress intensity factors to dynamic fracture initiation and propagation. *International Journal of Fracture*, vol. 201, no. 1, p. 81-96, **DOI:10.1007/s10704-016-0124-8**.

[75] Taylor, M., Steigmann, D. J. (2013). A two-dimensional peridynamic model for thin plates. *Mathematics and Mechanics of Solids*, vol. 20, no. 8, p. 998-1010, **DOI:10.1177/1081286513512925**.

[76] Chowdhury, S. R., Roy, P., Roy, D., Reddy, J. N. (2016). A peridynamic theory for linear elastic shells. *International Journal of Solids and Structures*, vol. 84, **DOI:110-132, 10.1016/j.ijsolstr.2016.01.019**.

[77] Qi, Z., Shaofan, L., Zao., A-M., Yuxiang, P., Jiale, Y. (2021). A peridynamic Reissner-Mindlin shell theory. *Numerical Methods in Engineering*, vol. 122, p. 122-147, **DOI:10.1002/nme.6527**.

[78] Kilic, B., Madenci, E. (2009). Prediction of crack paths in a quenched glass plate by using peridynamic theory. *International Journal of Fracture*, vol. 156, p. 165-177, **DOI:10.1007/s10704-009-9355-2**.

[79] Hu, Y. L., Madenci, E., Phan, N. (2018). Peridynamic Modeling of Cracking in Ceramic Matrix Composites. *Proceedings of the 17th International Conference on New Trends in Fatigue and Fracture*, p. 345-354, **DOI:10.1007/978-3-319-70365-7_40**.

[80] Bobaru, F., Ha, Y., Hu, W. (2012). Damage progression from impact in layered glass. *Central European Journal of Engineering*, vol. 2, p. 551-561, **DOI:10.2478/s13531-012-0020-6**.

[81] Hou, D., Zhang, W., Wang, P., Ma, H. (2019). Microscale peridynamic simulation of damage process of hydrated cement paste subjected to tension. *Construction and Building Materials*, vol. 228, p. 117053, **DOI:10.1016/j.conbuildmat.2019.117053**.

[82] Cheng, Z., Zhang, G., Wang, Y., Bobaru, F. (2015). A peridynamic model for dynamic fracture in functionally graded materials. *Composite Structures*, vol. 133, p. 529-546, **DOI:10.1016/j.compstruct.2015.07.047**.

[83] Bobaru, F., Duangpanya, M. (2012). A peridynamic formulation for transient heat conduction in bodies with evolving discontinuities. *Journal of Computational Physics*, vol. 231, p. 2764-2785, **DOI:10.1016/j.jcp.2011.12.017**.

[84] Oterkus, S., Madenci, E., Agwai, A. (2014). Fully coupled peridynamic thermomechanics. *Journal of the Mechanics and Physics of Solids*, vol. 64, p. 1-23, **DOI:10.1016/j.jmps.2013.10.011**.

[85] Madenci, E., Oterkus, S. (2017). Ordinary state-based peridynamics for thermoviscoelastic deformation. *Engineering Fracture Mechanics*, vol. 175, p. 31-45, **DOI:10.1016/j.engfracmech.2017.02.011**.

[86] Amani, J. Oterkus, E., Areias, P., Zi, P., Nguyen-Thoi, T., Rabczuk, T. (2016). A non-ordinary state-based peridynamics formulation for thermoplastic fracture. *International Journal of Impact Engineering*, vol. 87, p. 83-94, **DOI:10.1016/j.ijimpeng.2015.06.019**.

[87] Bazazzadeh, S., Mossaiby, F., Shojaei, A. (2020). An adaptive thermo-mechanical peridynamic model for fracture analysis in ceramics. *Engineering Fracture Mechanics*, vol. 223, p. 106708, **DOI:10.1016/j.engfracmech.2019.106708**.

[88] Liu, W., Hong, J.-W. (2012). A coupling approach of discretized peridynamics with finite element method. *Computer Methods in Applied Mechanics and Engineering*, vol. 245-246, p. 163-175, **DOI:10.1016/j.cma.2012.07.006**.

[89] Wildman, R. A., O'Grady, J. T., Gazonas, G. A. (2017). A hybrid multiscale finite element/peridynamics method. *International Journal of Fracture*, vol. 207, p. 41-53, **DOI:10.1007/s10704-017-0218-y**.

[90] Giannakeas, I. N., Papathanasiou, T. K., Fallah, A. S., Bahai, H. (2020). Coupling XFEM and Peridynamics for brittle fracture simulation. *Computational Mechanics*, vol. 66, no. 3, p. 683-705, **DOI:10.1007/s00466-020-01872-8**.

[91] Fan, H., Li, S. (2017). Parallel peridynamics-SPH simulation of explosion induced soil fragmentation by using OpenMP. *Computational Particle Mechanics*, vol. 4, p. 199-211, **DOI:10.1007/s40571-016-0116-5**.

[92] Brothers, M. D., Foster, J. T., Millwater, H. R. (2014). A comparison of different methods for calculating tangent-stiffness matrices in a massively parallel computational peridynamics code. *Computer Methods in Applied Mechanics and Engineering*, vol. 279, p. 247-267, **DOI:10.1016/j.cma.2014.06.034**.

[93] Diehl, P., Schweitzer, M. A. (2015). Efficient neighbor search for particle methods on GPUs. Barth, T. J., Griebel, M., Keyes, D. E., Nieminen, R. M., Roose, D., Schlick, T. (Eds.) *Meshfree Methods for Partial Differential Equations VII. Lecture Notes in Computational Science and Engineering*, Springer, Cham, **DOI:10.1007/978-3-319-06898-5_5**.

[94] Meo, D. D., Oterkus, E. (2017). Finite element implementation of a peridynamic pitting corrosion damage model. *Ocean Engineering*, vol. 135, p. 76-83, **DOI:10.1016/j.oceaneng.2017.03.002**.

Strojniški vestnik - Journal of Mechanical Engineering 67(2021)12, 682-691
DOI:10.5545/sv-jme.2021.7406
Original Scientific Paper
Received for review: 2021-09-15
Received revised form: 2021-11-23
Accepted for publication: 2021-11-24

Extremal-Micro Genetic Algorithm Model for Time-Cost Optimization with Optimal Labour Productivity

Sivakumar A.[1] – Bagath Singh N.[2,*] – Sathiamurthi P.[1] – Karthi Vinith K.S.[3]

[1] Kongu Engineering College, Department of Mechanical Engineering, India
[2] Kurinji College of Engineering and Technology, Department of Mechanical Engineering, India
[3] Kongu Engineering College, Department of Automobile Engineering, India

In a highly competitive manufacturing environment, it is critical to balance production time and cost simultaneously. Numerous attempts have been made to provide various solutions to strike a balance between these factors. However, more effort is still required to address these challenges in terms of labour productivity. This study proposes an integrated substitution and management improvement technique for enhancing the effectiveness of labour resources and equipment. Furthermore, in the context of time-cost optimization with optimal labour productivity, an extremal-micro genetic algorithm (Ex-μGA) model has been proposed. A real-world case from the labour-intensive medium-scale bus body fabricating industry is used to validate the proposed model performance. According to the results, the proposed model can optimize production time and cost by 34 % and 19 %, respectively, while maintaining optimal labour productivity. In addition, this study provides an alternative method for dealing with production parameter imbalances and assisting production managers in developing labour schedules more effectively.

Key words: labour productivity, equipment effectiveness, time-cost optimization, extremal optimization, micro genetic algorithm

Highlights

- *An integrated substitution and management improvement technique has been proposed for enhancing the effectiveness of labour resources and equipment.*
- *An extremal-micro genetic algorithm model has been proposed to optimize time and cost with optimal labour productivity.*
- *The proposed model provides optimal labour resource allocation for each activity in order to carry out work efficiently.*
- *This facilitates the production managers in developing an effective maintenance plan to enhance equipment effectiveness.*

0 INTRODUCTION

The most significant factors for planning and regulating labour-intensive projects are duration and cost analysis. The production manager is responsible for selecting various resources for the completion of an activity. Uncertainties and vulnerabilities in fabrication processes are taken into account throughout this decision-making process. In this regard, when discussing time-cost optimization, it is essential to review the terms 'crashing', 'fast-tracking', 'substitute', and 'management improvement techniques'. Crashing is a well-known project schedule compression technique that comprises taking action to shorten the overall project timeline after analysing several options. Shrinking schedule activity durations and increasing resource allocation on schedule activities are two popular crashing techniques [1]. However, crashing has negative consequences including congestion, overburdening workers, and fatigue. 'Fast-tracking' is a real-time way of analysing the volume and timeliness of assessments from start to finish [2]. Drawbacks to fast-tracking include defects, rework, and overloading. The third term, substitution, is the process of replacing resources and applying cutting-edge technology to increase a company's production within the time limits and budgets [3]. Its drawbacks such as over-costing, resistance and the time required to improve workforces. The fourth key term in time-cost optimization is management improvement techniques, such as skill enhancement training. The training programme is a strategy for enhancing an individual employee's knowledge and skills to perform given tasks flawlessly [4]. However, there are certain disadvantages to this method, including work interruption, separate improvement costs, and separate trainer employment costs.

The most crucial aspect of the optimization profession is figuring out how to meet deadlines on time and within budget. Numerous approaches are often used to investigate the optimization problem in terms of time and cost, including the fuzzy-based simulation annealing technique [5], critical path method, linear programming [6], non-dominated genetic algorithm [7], fuzzy logic with genetic algorithm [8], and learning curve methods [9]. Likewise, mathematical programming might be the most appropriate option. However, project managers are reluctant to employ it due to the difficulties in establishing projects with complex schedules. In

*Corr. Author's Address: Kurinji College of Engineering and Technology, Department of Mechanical Engineering, India, bagathresearch@gmail.com

addition, Peña-Mora and Li [10] developed a model to use system dynamics to accelerate building projects. They changed the labour productivity assumption, which had been used in earlier analyses as a constant. Productivity is estimated in the dynamic model as a function of schedule pressure and level of experience. Zhang et al. [11] used a heuristic technique to tackle construction projects' time-cost constraints. This method divides a project's activities into groups based on feasible combinations and then schedules all of the activities in the chosen group to reduce the project's time. A heuristic algorithm assesses all possible activity combinations and chooses the best one with the shortest project duration. The shortcoming of this technique is that it did not account for the impact of shorter project length on direct and overall project costs. Gerk and Qassim [12] introduced a mixed-integer non-linear programming model to assist automation enterprises in setting up time reduction projects. The time and cost savings are expected as a result of activity crashing, overlapping, and substitution. Lakshminarayanan et al. [13] considered a risk element to be an important aspect in the optimization of a building project. An ant colony optimization approach was used to handle the time-cost-risk trade off problem in the construction project. Based on the time-cost trade off problem, an objective function associated with each activity was developed using a set of quality indicators. The construction project risk was assessed and divided into several zones based on its importance. Likewise, Shrivastava et al. [14] devised a multi-objective optimization technique for the time-cost-quality-quantity problem in building projects based on the ant colony optimization technique. The objective functions were calculated in regards to the project's duration, overall cost, and quality. The drawback of this method is that the parameter they select is dependent on randomly chosen. Han et al. [15] proposed a system dynamics model to speed up construction projects. They concentrated on schedule delays caused by design flaws. The dynamic approach determines productivity as a function of scheduling pressure. Gracanin et al. [16] proposed value-stream optimization through lean strategies to reduce cost-time investment. This reduces the allocation of non-value-added overhead across the entire production process. Wood [17] used a fuzzy memetic optimization algorithm to investigate the stochastic duration-cost-quality trade off in the oil and gas industry. Taheri Amiri et al. [7] presented a non-dominated sorting genetic algorithm model for analysing concurrent cost and time minimization of projects with resource constraints. Jordan et al.[18] advocated the use of value stream analysis to reduce process waste and improve the economic efficiency of production. Lin and Lai [19] suggested a genetic algorithm model for multi-objective time-cost trade off analysis. Productivity is estimated using this method as a function of the management improvement strategy for labour training and the labour resource congestion factor. These investigations offered several efficient optimization models that may be used in various sectors. Most of these studies argued that shortening project length would invariably result in higher costs in a time-cost trade off context. Some of them also looked into labour productivity.

Furthermore, while heuristic approaches can predict the optimal level of activity acceleration and overlap in schedule compression, they cannot guarantee a global optimum. Dehghan et al. [20] assert that the genetic algorithm (GA) has given much more effective capacity to seek the optimal solution compared to traditional methodologies. Likewise, Trivedi and Namdev [21] investigated the heuristic, mathematical, and GA approaches for time-cost optimization, concluding that the genetic algorithm is the most adaptive meta-heuristic technique. Naseri [22] also compared linear programming to the GA model, concluding that GA can deliver a near-optimal solution. In a further study, Lin andLai [19] corroborate the superiority of GA in time-cost optimization. In contrast, the population size and parameter setting on the real-world problems significantly impact GA sampling capabilities. To address this issue, local search algorithms have been integrated with GA [23] and [24]. The key characteristic of GA is that it may easily be combined with various optimization techniques to enhance their performances.GA hybridized with other techniques has many advantages, including global optimization quality, efficiency, a guarantee of feasible solutions, and optimal control parameters [25].

According to the literature, changing productivities are frequently employed in the time and cost optimization context, mainly focusing on large-scale projects. However, labour-driven medium-scale projects, such as bus bodybuilding, also face uncertainty in the duration and cost of operation due to decreased labour efficiency. Likewise, the impact of long-term viability on equipment and labour productivity has not been studied in terms of time-cost optimization. Therefore, this study provides an interesting perspective on the uncertainties of time and cost along with labour productivity. Furthermore, this study proposes an integrated substitution and management improvement technique for enhancing

the effectiveness of labour resources and equipment. In addition, this study proposes a hybrid extremal-micro genetic algorithm (Ex-μGA) optimization model for determining an optimal solution for labour productivity and work schedules. Consequently, the model could shorten the duration of work and direct labour costs.

1 RESEARCH METHODOLOGY

The simple GA probably produces a global optimal solution. However, this will happen at a relatively slow rate. Hence, this is ineffective in real-world problem solving because it requires rapid convergence. For instance, during online optimization scenarios, the objective function might occur faster than the simple GA can find the best solution. In this sense, a rapid GA is essential for the online optimization process. The structure of the micro genetic algorithm (μGA) is identical to that of simple GA, and it is used to work with small populations. As a result, it necessitates fewer function evaluations than traditional GA [26]. The crossover operation is carried out in μGA. However, the mutation is not required, because sufficient variance had been maintained during micro population convergence. In contrast, the self-organized critical idea is at the heart of the extremal optimization technique. The most unfavourable variables in a suboptimal response are gradually replaced by newly produced random variables in this method. The physical instinct to streamline also can serve as a source of inspiration for extremal optimization. This path is commonly followed by its forerunners, such as simulated annealing and GA [27]. In this study, the μGA is combined with the extremal optimization technique to focus on improving optimization efficiency for small populations. The chromosome symbolizes the improving strategy, and the gene symbolizes the decision variable in this process. The time module reduces the amount of time spent within the original budget, while the cost module reduces the amount of money spent within a set amount of time.

1.1 Model Formulation

Management has provided a realistic and essential strategy for improving efficiency in bus body building operations. Improvement, in contrast, takes time and money. Hence, due to time and cost constraints, all viable improvement actions cannot be carried out. In the context of multi-objective decisions, decision-makers can prioritize the most appropriate alternative solutions while maintaining optimal time cost management. Consequently, the proposed model's goal is to assist decision-makers in recognizing a redesigned primary goal of improving efficiency while reducing time and direct labour expenses. The formulation and objective function of the mathematical model are presented in this section. The following assumptions are employed while developing the Ex-μGA optimization model.

1. The resources considered while optimizing the process is labour and equipment.
2. The external factors are inexact and inconsistent, so the model does not account for it.
3. The proposed model identifies that the original team is adequate and that the additional personnel is unnecessary.
4. The overtime strategy is not employed since it may increase costs and reduce efficiency.

The original project duration (PD) is expressed in Eq. (1),

$$PD = \sum_{i=1}^{j} \left(AD_i^{L_U L_P Q} \right), \tag{1}$$

where, $AD_i^{L_U L_P Q}$ is the actual project duration of activity (i), number of activity (j) mostly on project scheduling using labour productivity (L_P) labour usage (L_U) to complete the quantity of work (Q). The optimal target is to minimize fabrication duration (D_F). The objective function is follows as in Eq. (2):

$$\text{Minimize } D_F = \sum_{i}^{j} \left(AD_i^{L_U^* L_P^* Q} \right), \tag{2}$$

subject to $D_F < PD$.

Post optimization, according to the logical relationships and minimized process time, a new labour schedule composed for j operations could be created. Where $AD_i^{L_U^* L_P^* Q}$ is the new activity duration using optimal labour resource (L_U^*) with optimal productivity (L_P^*) to total the work quantity Q. The diverse elements that influence labour productivity could be classified using the factor model described by [20]. The labour time to complete (L_{TTC}) one quantity of work is computed as Eq. (3), and the labour productivity (L_P) computed as in Eq. (4),

$$L_{TTC} = \frac{mh}{q} = f\left(L_{EA}, E_{EL} \overline{R_S}, \overline{C_W} \right), \tag{3}$$

where mh is the input labour working hours, q is per work quantity, L_{EA} stands for labour environment allowance, which is used to constrain labour usage. E_{EL} is a management-identified equipment effectiveness improvement index as enhancing deliverables to constraint the labour productivity. R_S is the ability needed to perform the job, and C_W is the work content including such job role. R_S and

C_W are constants throughout this experiment since it is assumed that the worker is skilled to perform the job, and the work content is stated as a requirement for work, where *n* represents number of quantities completed with actual equipment effectiveness in a day and *DMH* represents daily man-hours utilized with respect to labour usage (L_U) in the actual scenario of work. In this study, the improvement factor as mentioned as improved equipment effectiveness (E_{EI}) is an index of measuring the improvement effect through management. The number of quantities (*N*) completed is a function of quantity (*n*) completed with actual equipment effectiveness (E_{EA}) versus improved equipment effectiveness (E_{EI}). The optimal labour productivity (L_P^*) after improvement through equipment effectiveness equals to amount of work (*N*) completed divided to daily man-hours with respect to optimal labour usage (L_U^*). The labour usage and improvement index are used as two sets of key decision variables that jointly decide the proposed Ex-μGA optimization model results. The relations among improved equipment effectiveness (E_{EI}), number of quantities (*N*) completed, optimal labour productivity (L_P^*), and *FD* are presented in the following Eqs. (5) to (8).

$$E_{EI} = f\left(E_A, E_P, W_Q\right), \tag{5}$$

$$N = f\left(n / E_{EA}, E_{EI}\right), \tag{6}$$

$$L_P^* = \left(\frac{N}{DMH}\right), \tag{7}$$

$$D_F = Q \times P / DMH, \tag{8}$$

where D_F is fabrication duration, *Q* is the quantity of work to be done, *DMH* is daily man-hours multiplied by daily straight hours (default: 8 hours). When *Q* is constant, fabrication duration is proportional to the labour productivity and inversely proportional to the man-hour. The fabrication cost (*FC*) with optimal duration has been estimated as Eq. (9).

$$FC = \sum_{x=1}^{n}\left[DLC_x^{L_U^* D_F} + C_I\right], \tag{9}$$

subject to $FC < PC$, where, $DLC_x^{L_U^* D_F}$ is direct labour cost with respect to optimal labour usage and optimal fabrication duration, C_I cost of improvement, and *PC* is proposed project cost.

2 CASE VALIDATION

The real-world problem has been utilized to propose an optimal model. This study has investigated uncertainties observed in a medium-scale bus body fabrication project carried out by a specific industry in Karur, Tamil Nadu, India. The chosen industry is recognized for fabricating city, school, tour, coach, and mini buses. It has 175 workers. This study has been done on the fabrication of city buses. A gemba crew of five professionals has been initially organized. The team includes educational specialists as well as production managers. The crew assesses the factors that influence the effectiveness of the equipment and measures the actual progress of the city bus fabrication process. In addition, the crew develops an improvement strategy.

The city bus body fabrication work consists of 11 distinct activities. There is no lag time in any of the relationships, according to the process, because they are determined by the characteristics of each activity. These are unaffected by the optimization process and have no influence on the final result. The suitable amount of available labour is determined based on the normal conditions for each task in terms of environmental allowance. Each activity's normal labour productivity is determined separately. The actual labour utilization is initially lower than the allowances for the working environment, because management strives to avoid workplace crowding. The production manager assigns labour with various skills to carry out the given activity. Furthermore, the labours cannot be swapped between different activities. The fabrication duration and cost are calculated using Eqs. (8) and (9), respectively, to provide the findings of this investigation. Table 1 shows the various activities and the initial progress of the fabrication process. Owing to the confidentiality of case project, the project labour cost was €1686.69. The work done per day with actual equipment effectiveness for all 11 activities was calculated as 879 units with labour usage of 54. The average L_{TTC} is 0.56 with average labour productivity of 1.95 units per man-hour. The total duration required to fabricate the city bus is 40 days.

2.1 Case Improvements

The improvement team thoroughly investigated the substituting and management improvement programme and decided to integrate those two techniques. The improvement index is identified as a means of increasing labour productivity. In general, the production manager may assign additional workers to speed up the schedule and reduce fabrication time if there is sufficient labour available. In contrast, when more employees are assigned, the working environment becomes increasingly crowded. Worker

Table 1. *Initial progress of the city bus fabrication process*

Activity	Activity name	Labour allowance	Labour usage	Labour productivity	Quantity [units]	Duration [days]	Cost [€]
1	Material preparation	5	5	2.38	950	10	380.31
2	Chassis preparation	5	5	1.89	400	5	202.07
3	Sheet metal preparation	7	6	1.89	150	2	88.40
4	Super structure fabrication	5	5	2.08	540	6	247.05
5	Frame assembly	4	4	2.04	190	3	88.73
6	Painting	6	6	2.63	675	5	244.49
7	Interior work	15	12	1.89	475	3	299.94
8	Window &glass fitting	4	4	2.04	124	2	57.92
9	Exterior work	4	4	2.08	120	2	54.90
10	Finishing	2	2	1.25	20	1	15.25
11	Inspection	1	1	1.25	10	1	7.63

productivity may decline as a result. The literature has demonstrated that crashing causes inefficiencies due to high labour density and congestion. Therefore, in this study, the environment labour allowance is taken as constraint to optimize labour usage. In addition, motivational techniques are used as part of an improvement programme. Short-term crew meetings and gemba walks are introduced to motivate workers, and this improves worker accountability and self-discipline. The cost of improvement for these management improvement strategies is low, because the same production manager is in charge of both. Therefore, the usual activities are unaffected by this integrated strategy.

Furthermore, optimal labour productivity (L_P^*) is associated with the improvement of overall equipment effectiveness (*OEE*). The resultant *OEE* is used to measure the effectiveness of the production system. From a wider perspective, total productive maintenance (*TPM*) can be characterized in terms of OEE **[28]** and **[29]**. The detailed list of research parameters, units, notation, and OEE estimation formula is in Table 2. These evaluations are essential to analyse the current situation in order to enforce the appropriate counter-measures. Self-maintenance techniques are the first line of defence. This entails adhering to the 5'S principles in order to maintain the proper equipment. Second, preventive maintenance has indeed been promoted in order to keep the unit up to date on a regular basis. A weekly source of power inspection by circulating air into the device, which lowers overheating and sporadic arc output, is one of the electrical maintenance remedies. Of course, the coolant level is controlled in order to prevent

Table 2. *Improvement parameters estimation*

Serial No	Parameter	Notation	Units	Calculation	Estimates (before TPM)	Estimates (after TPM)
1	Planned production time	T_p	[min]	measurement	395	395
2	Planned production speed	S_p	[weld /min]	measurement	1.2	1.2
3	Planned quantity	P_w	[-]	$T_p \times S_p$	474	474
4	Time per weld	T_w	[s]	measurement	50	50
5	Labour movement time	T_{lm}	[min]	measurement	16	8
6	Unscheduled break down time	T_b	[min]	measurement	48	15
7	Changeover & adjustment time	T_c	[min]	measurement	12	12
8	Scheduled stoppage duration	T_{ss}	[min]	measurement	50	50
9	Realized stoppage duration	T_{Lrs}	[min]	$T_{lm} + T_b + T_c + T_{ss}$	126	85
10	Total operating time	T_o	[min]	$T_p - T_{Lrs}$	269	310
11	Realized production speed	S_r	[weld / min]	measurement	0.5	1
12	Defects and rework	L_r	[-]	measurement	8	4
13	Total acceptable quantity	To_{aq}	[-]	$To_w - \mathrm{Lr}$	127	306
14	Total quantity of work	To_w	[-]	$S_r \times T_o$	135	310
15	Overall equipment effectiveness	OEE	[%]	$T_o \times S_r \times To_{aq} / (T_p \times S_p \times To_w)$	27	65

sludge from developing. There is a focus on generator welding machine maintenance, including changing the oil, filtration, air cleaners, and fuel filters. Finally, a load test is performed to check that weld output is accurate. In addition, for each selected parameter, countermeasures have been estimated and are listed in Table 2. The *OEE* rate has increased significantly (from 27 % to 65 %), since the TPM programme was implemented. Thus, the improvement factor is selected for the welding machine chosen to increase output work in the range of $27 < E_{EI} < 65$. Therefore, the work production quantity should increase as a result of the integrated improvement approach.

3 OPTIMIZATION RESULTS AND DISCUSSION

The parameters used in the proposed optimization method have been fine-tuned to achieve good results. The optimization is done with hybrid Ex-μGA. The optimization results are provided as the average of the ten best experiments with a maximum of 10,000 iterations. The run time for optimization is 7.91 s. The production manager could be able to enhance labour productivity by using the integrated improvement method. The results show that when improvement factor (E_{EI}) performs the maximum output is valued at an average of 86 %. Due to the improvement factor, the average optimal L_{TTC}*is reduced from 0.56 to 0.46 (man-hours required to complete unit quantity of work). The optimal labour productivity (L_P*) increased to 2.84 units per man-hour. The total fabrication duration (D_F) could be reduced from 41 days to 27 days with optimal cost of € 1372.80 and a congestion factor of 1. The congestion factor is computed using L_U / L_{EA}. It is used to assess workplace crowding and to avoid crashing. The fabrication duration, in contrast, will be reduced to 17 days if the production manager mobilizes all available labour to reduce the timeline. However, this mobilization raises the average congestion factor to 1.7, resulting in overcrowding and high labour costs. Furthermore, with improved productivity, actual labour usage could complete the fabrication in 28 days while spending less than the fabrication budget cost. However, compared to the optimal solution, these results in a lower congestion factor of 0.9 and a longer fabrication time. The optimized results are depicted in Table 3.

3.1 Improvement on Time and Cost

This is more beneficial than crashes in terms of reducing fabrication timelines by enhancing labour productivity. Similarly, the fabrication along with improvement costs is less than the actual budgeted direct labour cost. The consistency of maximum achieved effectiveness from the integrated improvement method cannot be achieved at all times. Therefore, the selective improvement index is concluded from the optimization using Ex-μGA. This enables for the most efficient use of labour resources and productivity, as well as providing the shortest bus fabrication duration. The results indicate an improvement of fabrication duration of 34 % and a cost improvement of 19 %with respect to the selected case. Figs. 1 and 2 demonstrate the comparison of time and cost of actual and optimized scenarios. This result acknowledges optimal acceleration as a method for balancing fabrication time and cost.

3.2 Improvement on Labour Productivity

In terms of labour productivity, when labour utilization exceeds the labour environment allowance, productivity diminishes as a result of overcrowding. In

Table 3. *Comparison of fabricating case study bus's basic with optimized information*

Activity	Equipment effectiveness after improvement, E_{EI}	Optimized labour usage	Optimized labour productivity	Quantity of work done [units]	Optimized duration [days]	Optimized fabrication cost [€]
1	0.59	5	5.22	950	5	213.69
2	0.57	5	4.02	400	3	139.66
3	1.00	7	1.62	150	2	88.40
4	0.65	5	4.99	540	3	158.34
5	0.61	4	4.65	190	2	92.58
6	1.00	6	2.63	675	5	244.49
7	1.00	15	1.51	475	3	299.94
8	1.00	4	2.04	124	2	57.92
9	1.00	4	2.08	120	2	54.90
10	1.00	2	1.25	20	1	15.25
11	1.00	1	1.25	10	1	7.63

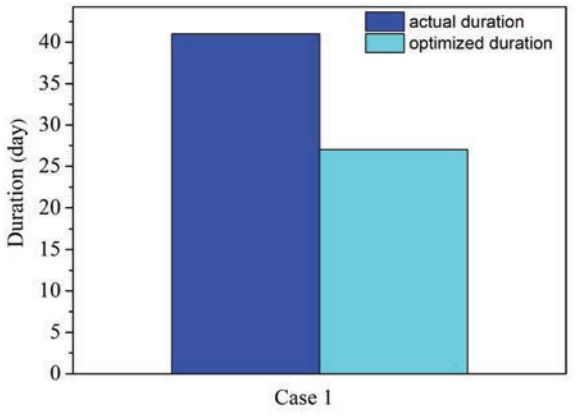

Fig. 1. *City bus body fabricating duration comparison*

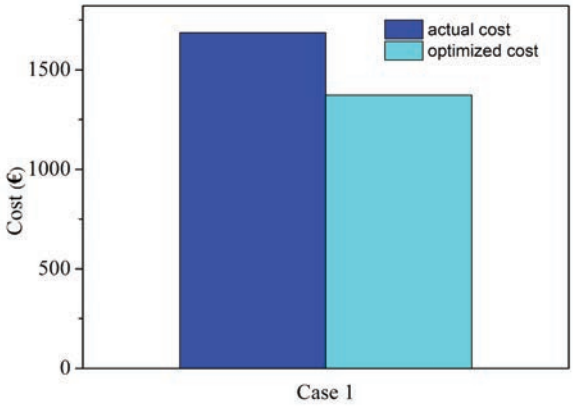

Fig. 2. *City bus body fabricating cost comparison*

the meantime, as labour usage slips below the labour environment allowance, production time increases. Therefore, optimum labour use can enhance labour productivity. Fig. 3 illustrates the growth of labour productivity. Table 4 demonstrates actual labour allocation as well as equipment effectiveness rates and four alternative optimized schedules. Furthermore, the optimal set of four with a 34 % acceleration rate is the best option for fabricating city buses within a fixed budget.

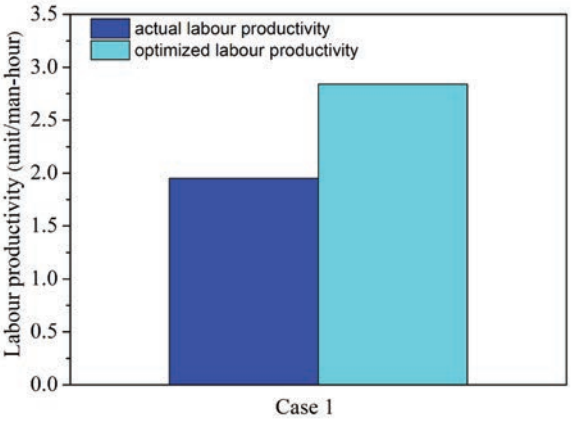

Fig. 3. *City bus body fabricating labour productivity comparison*

3.3 Statistical Hypothesis Test

This statistical test enables quantitative inferences to be drawn about the optimization model's outcomes. The paired *t*-test is employed for hypothesis testing because the mean difference between actual and optimized are paired observations. Table 5 demonstrates the paired *t*-test results. The calculated probability of obtaining the observed sample data is 0.076, 0.118, and 0.058. This confirms accepting the null hypothesis, which means the optimized values are suitable for completing this bus body fabrication work. This determined quantitative statistical evidence provides decisions to accept the hypothesis of the optimization process.

3.4 Comparison with Previous Techniques

The total cost in the preceding time-cost minimization context often consists of direct and indirect expenses that have been adversely and favourably associated with the production duration. The indirect expenses can be reduced when the duration is reduced, but the direct expenses are unavoidably increased due to inefficiency caused by crashing and fast-tracking. The

Table 4. *Paired t-test results*

Particulars	DF - Actual	DF -Optimized	FC - Actual	FC - Optimized	LP - Actual	LP - Optimized
N	11	11	11	11	11	11
Mean	3.636	2.636	13071	10638	1.947	2.842
STDEV	2.693	1.362	10781	8163	0.411	1.566
SE mean	0.812	0.411	3251	2461	0.124	0.472
Difference for 95 CI	(-0.124, 2.124)		(-735, 5599)		(-1.828, 0.039)	
t-value	1.98		1.71		2.14	
p-value	0.076		0.118		0.058	

direct cost, in contrast, has not been necessarily rising as a result of the timeline acceleration if resource usage efficiency is enhanced, as suggested by the proposed model. Table 5 compares the variation rate of time-cost optimization. This comparison demonstrates the significant differences in direct cost estimates between previous studies. This also shows the concept of critical approaches and methodologies. It also highlights how far the proposed model has advanced, which confirms that labour productivity enhancement can reduce time and cost simultaneously.

4 CONCLUSION

Most prior findings of time-cost optimization have been extensively carried out using techniques such as crashing, fast-tracking, costly substitution and management programs for labour improvements. However, simultaneous enhancement of existing resources such as machines and labours has not been encountered among those approaches. This study's primary importance is to apply an integrated improvement technique associated with time-cost optimization for enhancing productivity of machines as well as labours. The fabrication duration is significantly optimized as a result of productivity enhancement of available resources. This study also suggests that production managers could consider the proposed Ex-μGA optimization model initially in order to optimize fabrication process, which is also helpful for minimizing maintenance risk. Finally, the potential benefits of this integrated approach are sustainable for a long time. Hence, the proposed model provides important managerial insights into determining optimal labour resource allocation for each activity in order to carry out work efficiently. In addition, this facilitates the production managers to develop an effective maintenance plan to enhance equipment effectiveness. Furthermore, this facilitates communication between employees and their immediate superiors, resulting in a more harmonious working environment. The proposed time-cost optimization model has the potential to improve task performance significantly. However, future research will concentrate on the additional important factor of organizing flexible labour usage to accelerate schedules in the context of time-cost optimization using various optimization methodologies.

Table 5. *Optimal set for labour scheduling*

Activity	Actual		Optimal Set 1		Optimal Set 2		Optimal Set 3		Optimal Set 4	
	L_U	E_{EA}	L_U*	E_{EI}	L_U*	E_{EI}	L_U*	E_{EI}	L_U*	E_{EI}
1	5	0.27	4	0.37	5	0.45	5	0.59	5	0.59
2	5	0.27	4	0.40	4	0.43	5	0.57	5	0.57
3	6	1.00	5	1.00	7	1.00	6	1.00	7	1.00
4	5	0.27	5	0.38	5	0.47	5	0.65	5	0.65
5	4	0.27	4	0.39	4	0.48	4	0.61	4	0.61
6	6	1.00	6	1.00	5	1.00	6	1.00	6	1.00
7	12	1.00	14	1.00	13	1.00	12	1.00	15	1.00
8	4	1.00	4	1.00	4	1.00	4	1.00	4	1.00
9	4	1.00	4	1.00	4	1.00	4	1.00	4	1.00
10	2	1.00	2	1.00	2	1.00	2	1.00	2	1.00
11	1	1.00	1	1.00	1	1.00	1	1.00	1	1.00
Duration [days]	41		34		31		28		27	
Acceleration rate [%]	0		17		24		32		34	
Cost [€]	1686.68		1955.16		1486.26		1450.72		1372.79	

Table 6. *Comparison of optimization rates for various methodologies*

Reference	Time-cost optimization technique	Methodology	Variation on time optimization [%]	Variation on cost optimization [%]	Side effects
[19]	Management improvement	GAs	–4	–3	Interruption
[30]	Crashing	GAs	–35	+7	Congestion
[31]	Fast-tracking	nonlinear programming	–24	+13	Defects, rework, and overloading
This study case	Integrated substitution and management improvement	Ex-μGA	–34	–19	None

5 REFERENCES

[1] Garg, A. (2016). Project crashing algorithm. *International Conference on Emerging Trends in Civil Engineering*.

[2] O'Regan, N., Ghobadian, A., Sims, M. (2006). Fast tracking innovation in manufacturing SMEs. *Technovation*, vol. 26, no. 2, p. 251-261, **DOI:10.1016/j.technovation.2005.01.003**.

[3] Tsoi, H.-L. (2001). Using analytic hierarchy process (AHP) method to prioritise human resources in substitution problem. *International Journal of Computer, the Internet and Management*, vol. 9, p. 36-45.

[4] Ghodrati, N., Yiu, T.W., Wilkinson, S., Shahbazpour, M. (2018). Role of management strategies in improving labor productivity in general construction projects in New Zealand: Managerial perspective. *Journal of Management in Engineering*, vol. 34, no. 6, **DOI:10.1061/(asce)me.1943-5479.0000641**.

[5] Haque, K.M.A., Hasin, M.A.A. (2014). Fuzzy based project time-cost optimization using simulated annealing search technique. *International Journal of Information Technology Project Management*, vol. 5, no. 1, p. 90-103, **DOI:10.4018/ijitpm.2014010108**.

[6] Veludurthi, M.K., Anup, W.S., Sridevi,H. (2017). Comparative study of time-cost optimization. *International Journal of Civil Engineering and Technology*, vol. 8, no. 4, p. 659-663.

[7] Taheri Amiri, M.J., Haghighi, F.R., Eshtehardian, E., Abessi, O. (2018). Multi-project time-cost optimization in critical chain with resource constraints. *KSCE Journal of Civil Engineering*, vol. 22, p. 3738-3752, **DOI:10.1007/s12205-017-0691-x**.

[8] Yildirim, H.A., Akcay, C. (2019). Time-cost optimization model proposal for construction projects with genetic algorithm and fuzzy logic approach. *Journal of Construction*, vol. 18, no. 3, p. 554-567, **DOI:10.7764/RDLC.18.3.554**.

[9] Abdelkhalek, H.A., Refaie, H.S., Aziz, R.F. (2020). Optimization of time and cost through learning curve analysis. *Ain Shams Engineering Journal*, vol. 11, no. 4, p. 1069-1082, **DOI:10.1016/j.asej.2019.12.007**.

[10] Peña-Mora, F., Li, M. (2001). Dynamic planning and control methodology for design/build fast-track construction projects. *Journal of Construction Engineering and Management*, vol. 127, no. 1, **DOI:10.1061/(ASCE)0733-9364(2001)127:1(1)**.

[11] Zhang, H., Li, H., Tam, C.M. (2006). Heuristic scheduling of resource-constrained, multiple-mode and repetitive projects. *Construction Management and Economics*, vol. 24, no. 2, p. 159-169, **DOI:10.1080/01446190500184311**.

[12] Gerk, J.E.V., Qassim, R.Y. (2008). Project acceleration via activity crashing, overlapping, and substitution. *IEEE Transaction on Engineering Management*, vol. 55, no. 4, p. 590-601, **DOI:10.1109/TEM.2008.927786**.

[13] Lakshminarayanan, S., Gaurav, A., Arun, C. (2010). Multi-objective optimization of time-cost-risk using ant colony optimization. *International Journal of Project Planning and Finance*, vol. 1, no. 1, p. 22-38.

[14] Shrivastava, R., Singh, S., Dubey, G.C. (2012). Multi objective optimization of time cost quality quantity using multi colony ant algorithm. *International Journal of Contemporary Mathematical Sciences*, vol. 7, no. 16, p. 773-784.

[15] Han, S., Love, P., Peña-Mora, F. (2013). A system dynamics model for assessing the impacts of design errors in construction projects. *Mathematical and Computational Modelling*, vol. 57, no. 9-10, p. 2044-2053, **DOI:10.1016/j.mcm.2011.06.039**.

[16] Gracanin, D., Lalic, B., Beker, I., Lalic, D., Buchmeister, B. (2013). Cost-time profile simulation for job shop scheduling decisions. *International Journal of Simulation Modelling*, vol. 12, no. 4, p. 213-224, **DOI:10.2507/IJSIMM12(4)1.237**.

[17] Wood, D.A. (2017). Gas and oil project time-cost-quality trade off: Integrated stochastic and fuzzy multi-objective optimization applying a memetic, nondominated, sorting algorithm. *Journal of Natural Gas Science and Engineering*, vol. 45, p. 143-164, **DOI:10.1016/j.jngse.2017.04.033**.

[18] Jordan, E., Berlec, T., Rihar, L., Kusar, J. (2020). Simulation of cost driven value stream mapping. *International Journal of Simulation Modelling*, vol. 19, no. 3, p. 458-469, **DOI:10.2507/IJSIMM19-3-527**.

[19] Lin, C.L., Lai, Y.C. (2020). An improved time-cost trade-off model with optimal labor productivity. *Journal of Civil Engineering Management*, vol. 26, no. 2, p. 113-130, **DOI:10.3846/jcem.2020.11663**.

[20] Dehghan, R., Hazini, K., Ruwanpura, J. (2015). Optimization of overlapping activities in the design phase of construction projects. *Automationin Construction*, vol. 59, p. 81-95, **DOI:10.1016/j.autcon.2015.08.004**.

[21] Trivedi, D.K., Namdev, S. (2015). Use of optimization techniques in time-cost trade off (TCT) in civil construction: An overview. *International Journal of Civil Engineering and Mechanics*, vol. 2, no. 1, p. 1-13.

[22] Naseri, H. (2018). Time-cost trade off to compensate delay of project using genetic algorithm and linear programming. *International Journal of Innovation, Management and Technology*, vol 9, no. 6, p. 285-290, **DOI:10.18178/ijimt.2018.9.6.826**.

[23] Das, K.N. (2013). Hybrid genetic algorithm: An optimization tool. *Global Trends in Intelligent Computing Research and Development*, p. 268-305, **DOI:10.4018/978-1-4666-4936-1.ch010**.

[24] Singh, A., Deep, K. (2015). Real coded genetic algorithm operators embedded in gravitational search algorithm for continuous optimization. *International Journal of Intelligent Systems and Applications*, vol. 7, no. 12, p. 1-12, **DOI:10.5815/ijisa.2015.12.01**.

[25] Mishra, R., Das, K.N. (2017). A novel hybrid genetic algorithm for unconstrained and constrained function optimization. *Bio-Inspired Computing for Information Retrieval Applications*, p. 230-268, **DOI:10.4018/978-1-5225-2375-8.ch009**.

[26] Anderson, B.R., Price, P., Gunawidjaja, R., Eilers, H. (2015). Microgenetic optimization algorithm for optimal wavefront shaping. *Applied Optics*, vol. 54, no. 6, p. 1485-1491, **DOI:10.1364/ao.54.001485**.

[27] Majumdar, A., Debnath, T., Biswas, A., Sood, S.K., Baishnab, K.L. (2020). An energy efficient e-healthcare framework supported by novel EO-μGA (Extremal Optimization Tuned Micro-Genetic Algorithm). *Information Systems Frontiers*, vol. 23, p. 1039-1056, **DOI:10.1007/s10796-020-10016-5**.

[28] Jauregui Becker, J.M., Borst, J., van der Veen, A. (2015). Improving the overall equipment effectiveness in high-mix-low-

volume manufacturing environments. *CIRP Annals*, vol. 64, no. 1, p. 419-422, **DOI:10.1016/j.cirp.2015.04.126**.

[29] Sonmez, V., Testik, M.C. (2017). Using accurately measured production amounts to obtain calibration curve corrections of production line speed and stoppage duration consisting of measurement errors. *International Journal of Advanced Manufacturing Technology*, vol. 88, p. 3257-3263, **DOI:10.1007/s00170-016-9043-0**.

[30] Hegazy, T. (1999). Optimization of construction time-cost trade-off analysis using genetic algorithms. *Canadian Journal of Civil Engineering*, vol. 26, no. 6, p. 685-697, **DOI:10.1139/cjce-26-6-685**.

[31] Klanšek, U. (2016). Mixed-integer nonlinear programming model for nonlinear discrete optimization of project schedules under restricted costs. *Journal of Construction Engineering and Management*, vol. 142, no. 3, **DOI:10.1061/(asce)co.1943-7862.0001074**.

Vsebina

Strojniški vestnik - Journal of Mechanical Engineering
letnik 67, (2021), številka 12
Ljubljana, december 2021
ISSN 0039-2480

Izhaja mesečno

Razširjeni povzetki (extended abstracts)

Strojniški vestnik - Journal of Mechanical Engineering 67(2021)12, SI 77

Prejeto v recenzijo: 2021-06-30
Prejeto popravljeno: 2021-10-11
Odobreno za objavo: 2021-11-08

Študija sistema ekspanzijskih aksialno-radialnih veznih elementov Bondura®

Muhammad Maaz Akhtar[1] – Øyvind Karlsen[1,2] – Hirpa G. Lemu[1,*]

[1] Univerza v Stavangerju, Norveška
[2] Bondura Technology AS, Norveška

Članek obravnava rezultate preizkusov inovativnega elementa za spajanje vzporednih plošč, ki zavaruje spoj v aksialni in v radialni smeri. Rešitev je primerna kot zamenjava za standardne prednapete vijake, ali za uporabo v kombinaciji z njimi.

Radialni premiki delov vijačene prirobnične zveze zaradi vibracij povzročajo deformacije in zmanjšanje mikrohrapavosti površin, posledično pa samoodvijanje matic in zmanjšanje prednapetosti zveze. Izguba prednapetosti vijakov lahko privede do odpovedi zveze z vsemi posledicami. Zveze z inovativnimi aksialno-radialnimi elementi Bordura še niso bile predmet širših raziskav, zato je obstajala potreba po primerjavi zanesljivosti teh zvez s standardno rešitvijo z vijaki in maticami.

Prednapetost vijakov je ključnega pomena za zmogljivost in delovanje prirobničnih zvez s prednapetimi vijaki, saj preprečuje relativno gibanje med prirobnicama oz. med matico/glavo in prirobnico. Aksialno-radialni vezni element deluje kot mehanska zagozda, ki preprečuje relativna gibanja med matico, glavo in prirobnicami, s tem pa omejuje gibanje med prirobničnima površinama. Opravljeni so bili eksperimenti za določitev največje dosegljive predobremenitve dveh aksialno-radialnih veznih elementov premera Ø50 mm in Ø80 mm. Rezultati so bili nato primerjani z analitično določenimi rezultati za standardne vijake dimenzij M50 in M80. Prednapetost aksialno-radialnih elementov je bila izmerjena z merilnimi lističi. Opravljeni so bili tudi izračuni za različne kombinacije števila in velikosti priteznih vijakov. Podana je primerjava med najboljšo kombinacijo in rezultati za standardne vijake. Za primerjavo zmogljivosti upiranja radialno-aksialnega veznega elementa in standardnega sistema prednapetih vijakov radialnim oz. rotacijskim zdrsom zveze je bil v izračunih upoštevan mehanski aksialno-radialni zagozdni učinek, rezultati pa so bili potrjeni z analizo po metodi končnih elementov.

Standardni vijaki lahko sicer dosežejo večjo prednapetost kot optimizirani aksialno-radialni vezni elementi, slednji pa imajo zagozdni puši, ki preprečujeta relativno radialno gibanje med elementom in opornimi površinami ter med stičnimi ploskvami prirobnic in tako zmanjšajo tveganje odpovedi zveze. Pri radialni obremenitvi prirobnic 50 MPa je prišlo do zdrsov med prirobničnima površinama, med matico in prirobnico ter med glavo vijaka in prirobnico. Matica se lahko zaradi teh gibanj sama od sebe odvije že po nekaj ciklih, stične ploskve pa se poškodujejo z resnimi posledicami za zvezo. Pod enako obremenitvijo pri aksialno-radialnih veznih elementih zaradi zagozdnih puš ne more priti do zdrsov med sestavom elementa in prirobnicama, izguba prednapetosti pa je minimalna. Zvezo take varujeta zagozdni puši in mehanska trdnost osrednjega valjastega elementa in ne strižna nosilnost kontaktnih ploskev zaradi prednapetosti zveze. Strižna nosilnost aksialno-radialnega veznega elementa je za približno 200 % višja od strižne nosilnosti standardnih vijakov.

Članek opisuje le eksperimentalno študijo dveh aksialno-radialnih elementov velikosti Ø50 mm in Ø80 mm. Standardni vijaki in optimizirane različice aksialno-radialnih elementov niso bili preizkušeni. Strižna nosilnost obeh rešitev je bila določena računsko in ni bila izmerjena v fizičnem preizkusu z vsiljenim relativnim zdrsom prirobnic.

V članku so predstavljeni alternativni vezni elementi za spajanje vzporednih plošč in preprečevanje oziroma omejevanje relativnega gibanja med prirobnicama. Nova rešitev se lahko uporablja samostojno ali v kombinaciji s standardnimi prednapetimi vijaki za izboljšanje kakovosti zvez. Novi sistem aksialno-radialnih veznih elementov je patentiran na Norveškem in je primeren za prednapete prirobnične zveze, ki so izpostavljene močnim vibracijam.
Ključne besede: prednapetost, radialno varovanje, aksialno varovanje, ekspanzijski element, prirobnična zveza, strižna nosilnost, hrapavost stičnih ploskev, samoodvijanje

*Naslov avtorja za dopisovanje: Univerza v Stavangerju, N-4036, Stavanger, Norveška, Hirpa.g.lemu@uis.no

Strojniški vestnik - Journal of Mechanical Engineering 67(2021)12, SI 78

Prejeto v recenzijo: 2021-07-13
Prejeto popravljeno: 2021-10-23
Odobreno za objavo: 2021-11-09

Modeliranje in večciljna optimizacija rezanja jekel C45 in 42Cr4 z elastičnim abrazivnim orodjem

Irina Aleksandrova[1,*] – Anna Stoynova[2] – Anatoliy Aleksandrov[1]
[1]Tehniška univerza v Gabrovem, Republika Bolgarija
[2]Tehniška univerza v Sofiji, Republika Bolgarija

Rezanje z elastičnim abrazivnim orodjem je nov visokozmogljiv postopek za rezanje obdelovancev iz različno trdih materialov, ki zagotavlja manjšo obrabo rezalnih plošč in višjo kakovost obdelanih površin. Literature o rezanju z elastičnim abrazivnim orodjem pa je malo in zato so potrebne dodatne raziskave. Načrtovanje tovrstnih rezalnih operacij danes pogosto poteka le na osnovi izkušenj osebja ali podatkov iz priročnikov in trenutno ni matematičnih modelov, ki bi lahko pokrili vse vidike rezanja z elastičnim abrazivnim orodjem in povezali parametre s pogoji pri rezanju. Za izboljšanje učinkovitosti in uporabnosti rezanja z elastičnim abrazivnim orodjem je proces treba preučiti, modelirati in optimizirati tako, da bodo izpolnjeni izbrani ekonomski in tehnološki kriteriji – ob upoštevanju specifične narave in pogojev za izvedbo.

V članku je predstavljen predlog novega pristopa k modeliranju in optimizaciji procesa rezanja z elastičnim abrazivnim orodjem, ki odraža specifike procesa rezanja dveh razširjenih konstrukcijskih jekel za strojegradnjo (srednjeogljičnega jekla C45 in legiranega kromovega jekla 42Cr4). Za optimizacijski parameter je bila izbrana posplošena kriterijska funkcija. Gre za kompleksen indikator, ki karakterizira odvisne spremenljivke procesa rezanja z elastičnim abrazivnim orodjem.

S predlaganim optimizacijskim postopkom so bili določeni optimalni pogoji za rezanje jekel C45 in 42Cr4. Pridobljeni so bili naslednji rezultati:

(1) Za določitev posplošene kriterijske funkcije so bili razviti teoretični in eksperimentalni modeli, ki opisujejo kompleksne vplive kontrolnih spremenljivk procesa (premer rezalnega koluta d_s, pritisna sila F in vrtilna frekvenca obdelovanca n_w). Modeli so bili ustvarjeni na osnovi kompleksnih študij in modeliranja odvisnih spremenljivk v procesu rezanja z elastičnim abrazivnim orodjem (obraba rezalne plošče, čas rezanja, temperatura obdelovanca, temperatura rezalne plošče) glede na delovne pogoje.

(2) Z uporabo posplošene kriterijske funkcije in genetskega algoritma so bili določeni optimalni pogoji za izvajanje procesa: premer rezalnega koluta d_s = 120 mm, pritisna sila F = 1 daN in vrtilna frekvenca obdelovanca n_w = 63,7 min^{-1} oz. n_w = 49,9 min^{-1} za jekli C45 in 42Cr4. Verodostojnost izračunanih optimalnih pogojev je bila preverjena z eksperimentalno študijo odvisnih spremenljivk v procesu rezanja. Potrjeno je bilo, da ti pogoji zagotavljajo najboljšo kombinacijo stopnje obrabe rezalne plošče ($\delta \leq 1{,}58$ mm), temperature rezalnega koluta ($T_s \leq 167$ °C), temperature obdelovanca ($T_w \leq 965$ °C), temperature odrezanega kosa ($T_d \leq 212$ °C) in časa rezanja ($t_c \leq 12{,}95$ s).

Rezultati novega pristopa k optimizaciji omogočajo izboljšanje učinkovitosti in obvladovanje procesa rezanja z elastično abrazivno ploščo z izbiro optimalnih pogojev za specifično implementacijo procesa. Potrdili so tudi ključno vlogo vrtilne frekvence obdelovanca, pritisne sile in premera rezalnega koluta pri življenjski dobi rezalnega koluta, produktivnosti rezanja ter porazdelitvi temperature v orodju, obdelovancu in odrezanem kosu.

Z ozirom na visoko produktivnost in nizke stroške procesa rezanja z elastičnim abrazivnim orodjem bodo predlagani pristop z večciljno optimizacijo in rezultati teoretično-eksperimentalnih raziskav iz članka uporabni za podjetja, ki se ukvarjajo s strojegradnjo.

Ključne besede: rezanje z elastičnim abrazivnim orodjem, rezalni kolut, večciljna optimizacija, posplošena kriterijska funkcija, jekli C45 in 42Cr4, premer rezalnega koluta, pritisna sila, vrtilna frekvenca obdelovanca

*Naslov avtorja za dopisovanje: Tehniška univerza v Gabrovem, 4 H. Dimitar St, Gabrovo, Republika Bolgarija, irina@tugab.bg

Prejeto v recenzijo: 2021-07-12
Prejeto popravljeno: 2021-09-19
Odobreno za objavo: 2021-10-07

Preiskava zmogljivosti rezanja s krožno žago v paketu ANSYS/LS-DYNA

Zhiwen Wang[1] – Qingliang Zeng[1,3*] – Zhenguo Lu[2] – Lirong Wan[1] – Xin Zhang[1] – Zhihai Liu[2]

[1] Znanstveno-tehniška univerza v Shandongu, Kolidž za strojništvo in elektroniko, Kitajska
[2] Znanstveno-tehniška univerza v Shandongu, Kolidž za transport, Kitajska
3 Normalka v Shandongu, Kolidž za informatiko, Kitajska

Krožne žage so običajno orodje za obdelavo kamna in njihova zmogljivost je pomembna. Opredeljena je bila numerična metoda za simulacije rezanja kamna z upogljivim krožnim listom, ki omogoča preučevanje vplivov vrtilne hitrosti in podajanja na poškodbe in napetosti v kamnu in v samem listu. Numerična simulacija je bila verificirana in dopolnjena s preizkusi in simulacijami enoosnih tlačnih obremenitev. Članek obravnava rezanje kamna z upogljivim listom krožne žage pri konstantnih rezalnih parametrih. Ugotovljeno je bilo, da imajo rezalni parametri velik vpliv na zmogljivost rezanja in na poškodbe kamna.

(1) Uporabnost numerične simulacije je bila preverjena z enoosnim tlačnim preizkusom in z numerično simulacijo enoosne tlačne obremenitve za izboljšanje modela rezanja.
(2) Rezultati kažejo, da se območje porazdelitve napetosti v listu povečuje s podajanjem in z vrtilno hitrostjo. Porazdelitev napetosti v segmentih in v telesu krožne žage je značilno korelirana z rezalnimi parametri.
(3) Rezalna sila je tesno povezana z rezalnimi parametri ter se zmanjšuje z rezalno hitrostjo in povečuje s podajanjem.
(4) Rezalna sila, vertikalna sila in horizontalna sila dvojnega žaginega lista je manjša kot pri enojnem listu, medtem ko je aksialna sila znatno večja.
(5) Rezalna sila, horizontalna sila in vertikalna sila dvojnega lista se povečujejo z razmikom listov, aksialna sila pa se zmanjšuje.

Vpliv rezalnih parametrov na list ter napetosti v kamnu in poškodbe kamna med rezanjem je bila preučeno z numeričnimi simulacijami. Napetostno stanje v listu krožne žage je povezano z napetostmi v kamnu in njegovimi poškodbami med rezanjem. Vpliv rezalnih parametrov krožne žage na zmogljivost rezanja je bil natančno analiziran. Rezultate preiskave bo mogoče uporabiti za optimizacijo rezalnih parametrov za boljšo učinkovitost in nižje stroške obdelave. Z numeričnimi simulacijami rezanja kamna se lahko izboljša uspešnost in znižajo stroški raziskav ter točno določijo napetosti v listu krožne žage kot osnova za preučevanje obrabe.

Rezultati raziskave rezanja trdega kamna z upogljivim listom krožne žage bodo lahko izhodišče za optimizacijo rezalnih parametrov in izboljšanje učinkovitosti rezanja. V prihodnjih raziskavah bo obravnavano rezanje različnih vrst trdega kamna in analiziran vpliv parametrov kamnine na zmogljivost rezanja in na lomljenje kamna.

Ključne besede: list krožne žage, poškodbe kamna, rezalna sila, napetost, podajanje, vrtilna hitrost

*Naslov avtorja za dopisovanje: Znanstveno-tehniška univerza v Shandongu, Kolidž za strojništvo in elektroniko, Kitajska, qlzeng@sdust.edu.cn

Strojniški vestnik - Journal of Mechanical Engineering 67(2021)12, SI 80

Prejeto v recenzijo: 2021-06-11
Prejeto popravljeno: 2021-09-18
Odobreno za objavo: 2021-10-29

Pregled peridinamike: teorija, možnosti uporabe in perspektive

Gábor Ladányi[1,*] – Viktor Gonda[2]

[1] Univerza v Dunaújvárosu, Inštitut za tehniške vede, Madžarska
[2] Univerza v Óbudi, Fakulteta za strojništvo in varnostni inženiring Donát Bánki, Madžarska

Modeliranje in simulacija degradacije materialov, zlasti zlomov v trdnih snoveh na različnih dimenzijskih in časovnih skalah, kljub razvoju različnih pristopov še vedno predstavljata velik izziv. Pričujoči pregled zajema rezultate raziskovalnega dela na področju metod nelokalnega peridinamičnega modeliranja. Ta v enotnem okvirju omogoča popis zveznih pojavov in sledenje celotni evoluciji razpok v trdnih snoveh– iniciranju, širjenju, cepitvi in zraščanju razpok. Namen tega pregleda je podati zgoščen povzetek najnovejšega razvoja peridinamične teorije trdne snovi in osvetliti možne smeri razvoja.

Porušitev konstrukcij je kompleksen pojav na več dimenzijskih in časovnih skalah. Numerična metoda za točno modeliranje procesa razvoja razpok mora pokriti iniciranje, širjenje, cepitev, zraščanje in ločevanje razpok. Klasični pristopi linearne elastomehanike in nelinearne lomne mehanike ter razširjena MKE (X-FEM) sicer dajejo delne rešitve, iniciranje in cepitev razpok pa kljub temu ostajata odprt problem. Analize diskretnih mehanskih sistemov, kot je npr. molekularna dinamika, sicer niso obremenjene s temi pomanjkljivostmi, vendar so omejene na manjši volumen oz. časovni segment. Peridinamika kombinira prednosti klasične mehanike kontinuuma in molekularne dinamike ter je primerna za obdelavo singularnosti in separacij med razvojem poškodbe.

Avtorja sta po pregledu večjega števila objav na temo peridinamike pripravila jedrnat pregled ključnih konceptov in možnosti uporabe ter identificirala možne poti razvoja: povezovanje mehanike velikih deformacij z nelinearnostmi v materialu in razvoj visokoučinkovitih peridinamičnih reševalnikov.

Ugotovljeno je bilo, da ima nelokalnost peridinamike pomembno vlogo pri simulacijah širjenja, cepitve in združevanja razpok v krhkih materialih. Peridinamika omenjene pojave opiše brez umetnih pogojev v zvezi s hitrostjo pri vrhu razpok, rezultati modela pa se v mnogih standardiziranih in »realnih« konfiguracijah odlično ujemajo z eksperimentalnimi podatki. Pregled objav nekaj zadnjih desetletij je pokazal štiri možne smeri prihodnjega razvoja:

(1) Peridinamika ima velik potencial v nelinearni in duktilni lomni mehaniki. Kombinacija peridinamike in duktilnosti predstavlja izziv in običajni eksplicitni peridinamični reševalniki niso dovolj učinkoviti. Zato obstaja potreba po razvoju implicitnih in/ali učinkovitejših eksplicitnih reševalnikov.
(2) Pri večjih deformacijah so bile ugotovljene težave z numerično stabilnostjo, ki pa so se jim posvetili le redki avtorji. Določena je bila tudi zveza med brezmrežnimi metodami in peridinamiko. Uvedba peridinamike višjega reda je tako možna rešitev za težave s stabilnostjo.
(3) Možna smer razvoja v prihodnjih letih bo tudi analiza numerične stabilnosti, robustnosti in učinkovitosti peridinamike. Ta je sicer zelo točna, njena hitrost in učinkovitost pri »industrijskih« problemih pa ne dosegata hitrosti sodobnih metod, npr. razširjene MKE in brezmrežnih metod. Kombiniranje peridinamike s temi metodami je zelo učinkovito in vzporedno računanje (npr. na superračunalnikih ali z grafičnimi karticami) se kar samo ponuja kot alternativna rešitev za izboljšanje hitrosti in učinkovitosti.
(4) Vse več je tudi objav o multifizikalnih in multidisciplinarnih raziskavah.

Če bo peridinamika uspešno razrešila problem mehanike velikih deformacij v trdnih snoveh, se bodo odprle nove možnosti za raziskave ločevanja (širjenja razpok) ali spajanja mehkih tkiv v aplikacijah na področju biomehanike in biofizike.

Članek podaja reprezentativen pregled nad evolucijo področja peridinamičnega modeliranja. Razdelana so področja uporabe, kjer je že dosežen konsenz. Na osnovi analize stanja razvoja peridinamičnega modeliranja so podani predlogi možnih smeri prihodnjih raziskav za obravnavo nelinearnosti v materialu in geometriji ter za izboljšanje numerične učinkovitosti pri sklopljenih multifizikalnih problemih.

Ključne besede: peridinamika, lomna mehanika, mehanika poškodb, nelokalna mehanika

*Naslov avtorja za dopisovanje: Univerza v Dunaújvárosu, Inštitut za tehniške vede, Táncsics M. u. 1/a, 2400 Dunaújváros, Madžarska, ladanyi@uniduna.hu

Strojniški vestnik - Journal of Mechanical Engineering 67(2021)12, SI 81

Prejeto v recenzijo: 2021-09-15
Prejeto popravljeno: 2021-11-23
Odobreno za objavo: 2021-11-24

Časovno-stroškovna optimizacija produktivnosti dela z modelom na osnovi ekstremalnega – mikrogenetskega algoritma

Sivakumar A.[1] – Bagath Singh N.[2,*] – Sathiamurthi P.[1] – Karthi Vinith K.S.[3]

[1] Tehniški kolidž Kongu, Oddelek za strojništvo, Indija
[2] Kolidž za inženiring in tehnologijo Kurinji, Oddelek za strojništvo, Indija
[3] Tehniški kolidž Kongu, Oddelek za Avtomobilno strojništvo, India

Usklajevanje časa in stroškov proizvodnje je ključnega pomena v današnjem visokokonkurenčnem proizvodnem okolju. Obstajajo mnogi poskusi za doseganje ravnotežja med omenjenima dejavnikoma, iz katerih izhajajo različne rešitve. Potrebni pa so še dodatni napori za obvladovanje omenjenega izziva na področju produktivnosti dela. Pregled literature je pokazal, da se pri časovni in stroškovni optimizaciji večjih projektov pogosto uporabljajo prilagoditve produktivnosti. Srednje veliki projekti z velikim vložkom dela, kot je denimo gradnja avtomobilskih nadgradenj, so obremenjeni z negotovostmi na področju trajanja in stroškov zaradi zmanjšanja delovne učinkovitosti. Vpliv dolgoročne sposobnosti preživetja na produktivnost opreme in dela prav tako ni bil preučen z vidika časovnih in stroškovnih optimizacij. Pričujoča študija zato predstavlja vpogled v negotovosti na področju časa, stroškov in produktivnosti dela. V članku je podan tudi predlog integrirane tehnike za zamenjavo in izboljšanje upravljanja, ki viša učinkovitost človeških virov in opreme. Podan je tudi predlog hibridnega optimizacijskega modela na osnovi ekstremalnega – mikrogenetskega algoritma (Ex-μGA) za določanje optimalne produktivnosti dela in časovnice izvajanja del. Model omogoča skrajšanje časa izdelave in znižanje neposrednih stroškov dela. Z natančno nastavitvijo parametrov iz predlaganega optimizacijskega modela so bili doseženi dobri rezultati. Optimizacija je bila opravljena s hibridnim algoritmom Ex-μGA. Za rezultat optimizacije je bilo vzeto povprečje najboljših 10 eksperimentov z največ 10.000 iteracijami. Čas izvajanja optimizacije je bil 7,91 sekunde. Vodje proizvodnje lahko izboljšajo produktivnost dela z integrirano metodo izboljšav. Povprečni optimalni delovni čas za dokončanje del se skrajša z 0,56 na 0,46 (število človek-ur, ki je potrebno za dokončanje enote dela). Optimalna produktivnost dela se tako poveča na 2,84 enote na človek-uro. Skupni čas proizvodnje bi bilo mogoče skrajšati z 41 na 27 dni z optimalnimi stroški v višini 101.486 rupij in faktorjem zastojev 1. Rezultati nakazujejo priložnost za 34-odstotno skrajšanje časa izdelave nadgradnje mestnega avtobusa in 19-odstotno znižanje stroškov. To potrjuje optimalno pospešitev kot metodo za uravnoteženje časa in stroškov izdelave. Predlagani model časovno-stroškovne optimizacije lahko občutno izboljša izvajanje dejavnosti. Model Ex-μGA je primeren za vodje proizvodnje, ki ga lahko uporabijo za optimizacijo procesa izdelave. Pomaga lahko tudi pri zmanjševanju tveganj, povezanih z vzdrževanjem. Potencialne koristi integriranega pristopa imajo trajnostni učinek. Predlagani model zagotavlja pomembne vodstvene informacije za optimalno razporejanje človeških virov na posamezne aktivnosti in učinkovito izvajanje del. Vodje proizvodnje lahko z njim razvijejo tudi načrt vzdrževanja, ki izboljša učinkovitost opreme. S tem se izboljša tudi komunikacija med zaposlenimi in njihovimi nadrejenimi za bolj harmonično delovno okolje. Prihodnje raziskave bodo usmerjene v dejavnike prilagodljive organizacije dela za pospešitev izvajanja projektov v kontekstu časovno-stroškovne optimizacije po različnih metodah.

Prispevek, novosti, vrednost:

- Predstavljen je predlog za integrirano zamenjavo in izboljšanje upravljanja, ki dviga učinkovitost človeških virov in opreme.
- Predlagan je ekstremalni – mikrogenetski algoritem za optimizacijo časa in stroškov s ciljem optimalne produktivnosti dela.
- Predlagani model zagotavlja optimalno razporejanje človeških virov na posamezne aktivnosti za učinkovito izvajanje del.
- Vodje proizvodnje lahko z njim razvijejo učinkovit načrt vzdrževanja, ki poveča učinkovitost opreme.

Ključne besede: izdelava nadgradenj za avtobuse, produktivnost dela, učinkovitost opreme, optimizacija časa in stroškov, ekstremalna optimizacija, mikrogenetski algoritem

*Naslov avtorja za dopisovanje: Kolidž za inženiring in tehnologijo Kurinji, Oddelek za strojništvo, Indija, bagathresearch@gmail.com

Guide for Authors

All manuscripts must be in English. Pages should be numbered sequentially. The manuscript should be composed in accordance with the Article Template given above. The maximum length of contributions is 12 pages (approx. 5000 words). Longer contributions will only be accepted if authors provide justification in a cover letter. For full instructions see the Information for Authors section on the journal's website: http://en.sv-jme.eu .

SUBMISSION:

Submission to SV-JME is made with the implicit understanding that neither the manuscript nor the essence of its content has been published previously either in whole or in part and that it is not being considered for publication elsewhere. All the listed authors should have agreed on the content and the corresponding (submitting) author is responsible for having ensured that this agreement has been reached. The acceptance of an article is based entirely on its scientific merit, as judged by peer review. Scientific articles comprising simulations only will not be accepted for publication; simulations must be accompanied by experimental results carried out to confirm or deny the accuracy of the simulation. Every manuscript submitted to the SV-JME undergoes a peer-review process.

The authors are kindly invited to submit the paper through our web site: http://ojs.sv-jme.eu. The Author is able to track the submission through the editorial process - as well as participate in the copyediting and proofreading of submissions accepted for publication - by logging in, and using the username and password provided.

SUBMISSION CONTENT:

The typical submission material consists of:

- A **manuscript** (A PDF file, with title, all authors with affiliations, abstract, keywords, highlights, inserted figures and tables and references),
- Supplementary files:
  - a **manuscript** in a WORD file format
  - a **cover letter** (please see instructions for composing the cover letter)
  - a ZIP file containing **figures** in high resolution in one of the graphical formats (please see instructions for preparing the figure files)
  - possible **appendicies** (optional), cover materials, video materials, etc.

Incomplete or improperly prepared submissions will be rejected with explanatory comments provided. In this case we will kindly ask the authors to carefully read the Information for Authors and to resubmit their manuscripts taking into consideration our comments.

COVER LETTER INSTRUCTIONS:

Please add a **cover letter** stating the following information about the submitted paper:

1. Paper **title**, list of **authors** and their **affiliations**. **One** corresponding author should be provided.
2. **Type of paper**: original scientific paper (1.01), review scientific paper (1.02) or short scientific paper (1.03).
3. A **declaration** that neither the manuscript nor the essence of its content has been published in whole or in part previously and that it is not being considered for publication elsewhere.
4. State the **value of the paper** or its practical, theoretical and scientific implications. What is new in the paper with respect to the state-of-the-art in the published papers? Do not repeat the content of your abstract for this purpose.
5. We kindly ask you to suggest at least two **reviewers** for your paper and give us their names, their full affiliation and contact information, and their scientific research interest. The suggested reviewers should have at least two relevant references (with an impact factor) to the scientific field concerned; they should not be from the same country as the authors and should have no close connection with the authors.

FORMAT OF THE MANUSCRIPT:

The manuscript should be composed in accordance with the Article Template. The manuscript should be written in the following format:

- A **Title** that adequately describes the content of the manuscript.
- A list of **Authors** and their **affiliations**.
- An **Abstract** that should not exceed 250 words. The Abstract should state the principal objectives and the scope of the investigation, as well as the methodology employed. It should summarize the results and state the principal conclusions.
- 4 to 6 significant **key words** should follow the abstract to aid indexing.
- 4 to 6 **highlights;** a short collection of bullet points that convey the core findings and provide readers with a quick textual overview of the article. These four to six bullet points should describe the essence of the research (e.g. results or conclusions) and highlight what is distinctive about it.
- An **Introduction** that should provide a review of recent literature and sufficient background information to allow the results of the article to be understood and evaluated.
- A **Methods** section detailing the theoretical or experimental methods used.
- An **Experimental section** that should provide details of the experimental set-up and the methods used to obtain the results.
- A **Results** section that should clearly and concisely present the data, using figures and tables where appropriate.
- A **Discussion** section that should describe the relationships and generalizations shown by the results and discuss the significance of the results, making comparisons with previously published work. (It may be appropriate to combine the Results and Discussion sections into a single section to improve clarity.)
- A **Conclusions** section that should present one or more conclusions drawn from the results and subsequent discussion and should not duplicate the Abstract.
- **Acknowledgement** (optional) of collaboration or preparation assistance may be included. Please note the source of funding for the research.
- **Nomenclature** (optional). Papers with many symbols should have a nomenclature that defines all symbols with units, inserted above the references. If one is used, it must contain all the symbols used in the manuscript and the definitions should not be repeated in the text. In all cases, identify the symbols used if they are not widely recognized in the profession. Define acronyms in the text, not in the nomenclature.
- **References** must be cited consecutively in the text using square brackets [1] and collected together in a reference list at the end of the manuscript.
- **Appendix(-icies)** if any.

SPECIAL NOTES

Units: The SI system of units for nomenclature, symbols and abbreviations should be followed closely. Symbols for physical quantities in the text should be written in italics (e.g. *v*, *T*, *n*, etc.). Symbols for units that consist of letters should be in plain text (e.g. ms^{-1}, K, min, mm, etc.). Please also see: http://physics.nist.gov/cuu/pdf/sp811.pdf .

Abbreviations should be spelt out in full on first appearance followed by the abbreviation in parentheses, e.g. variable time geometry (VTG). The meaning of symbols and units belonging to symbols should be explained in each case or cited in a **nomenclature** section at the end of the manuscript before the References.

Figures (figures, graphs, illustrations digital images, photographs) must be cited in consecutive numerical order in the text and referred to in both the text and the captions as Fig. 1, Fig. 2, etc. Figures should be prepared without borders and on white grounding and should be sent separately in their original formats. If a figure is composed of several parts, please mark each part with a), b), c), etc. and provide an explanation for each part in Figure caption. The caption should be self-explanatory. Letters and numbers should be readable (Arial or Times New Roman, min 6 pt with equal sizes and fonts in all figures). Graphics (submitted as supplementary files) may be exported in resolution good enough for printing (min. 300 dpi) in any common format, e.g. TIFF, BMP or JPG, PDF and should be named Fig1.jpg, Fig2.tif, etc. However, graphs and line drawings should be prepared as vector images, e.g. CDR, AI. Multi-curve graphs should have individual curves marked with a symbol or otherwise provide distinguishing differences using, for example, different thicknesses or dashing.

Tables should carry separate titles and must be numbered in consecutive numerical order in the text and referred to in both the text and the captions as Table 1, Table 2, etc. In addition to the physical quantities, such as *t* (in italics), the units [s] (normal text) should be added in square brackets. Tables should not duplicate data found elsewhere in the manuscript. Tables should be prepared using a table editor and not inserted as a graphic.

REFERENCES:

A reference list must be included using the following information as a guide. Only cited text references are to be included. Each reference is to be referred to in the text by a number enclosed in a square bracket (i.e. [3] or [2] to [4] for more references; do not combine more than 3 references, explain each). No reference to the author is necessary.

References must be numbered and ordered according to where they are first mentioned in the paper, not alphabetically. All references must be complete and accurate. Please add DOI code when available. Examples follow.

Journal Papers:

Surname 1, Initials, Surname 2, Initials (year). Title. Journal, volume, number, pages, DOI code.

[1] Hackenschmidt, R., Alber-Laukant, B., Rieg, F. (2010). Simulating nonlinear materials under centrifugal forces by using intelligent cross-linked simulations. *Strojniški vestnik - Journal of Mechanical Engineering,* vol. 57, no. 7-8, p. 531-538, DOI:10.5545/sv-jme.2011.013.

Journal titles should not be abbreviated. Note that journal title is set in italics.

Books:

Surname 1, Initials, Surname 2, Initials (year). Title. Publisher, place of publication.

[2] Groover, M.P. (2007). *Fundamentals of Modern Manufacturing*. John Wiley & Sons, Hoboken.

Note that the title of the book is italicized.

Chapters in Books:

Surname 1, Initials, Surname 2, Initials (year). Chapter title. Editor(s) of book, book title. Publisher, place of publication, pages.

[3] Carbone, G., Ceccarelli, M. (2005). Legged robotic systems. Kordić, V., Lazinica, A., Merdan, M. (Eds.), Cutting Edge Robotics. Pro literatur Verlag, Mammendorf, p. 553-576.

Proceedings Papers:

Surname 1, Initials, Surname 2, Initials (year). Paper title. Proceedings title, pages.

[4] Štefanić, N., Martinčević-Mikić, S., Tošanović, N. (2009). Applied lean system in process industry. *MOTSP Conference Proceedings*, p. 422-427.

Standards:

Standard-Code (year). Title. Organisation. Place.

[5] ISO/DIS 16000-6.2:2002. *Indoor Air – Part 6: Determination of Volatile Organic Compounds in Indoor and Chamber Air by Active Sampling on TENAX TA Sorbent, Thermal Desorption and Gas Chromatography using MSD/FID.* International Organization for Standardization. Geneva.

WWW pages:

Surname, Initials or Company name. Title, from http://address, date of access.

[6] Rockwell Automation. Arena, from *http://www.arenasimulation.com,* accessed on 2009-09-07.

EXTENDED ABSTRACT:

When the paper is accepted for publishing, the authors will be requested to send an **extended abstract** (approx. one A4 page or 3500 to 4000 characters or approx. 600 words). The instruction for composing the extended abstract are published on-line: http://www.sv-jme.eu/information-for-authors/ .

COPYRIGHT:

Authors submitting a manuscript do so on the understanding that the work has not been published before, is not being considered for publication elsewhere and has been read and approved by all authors. The submission of the manuscript by the authors means that the authors automatically agree to transfer copyright to SV-JME when the manuscript is accepted for publication. All accepted manuscripts must be accompanied by a Copyright Transfer Agreement, which should be sent to the editor. The work should be original work by the authors and not be published elsewhere in any language without the written consent of the publisher. The proof will be sent to the author showing the final layout of the article. Proof correction must be minimal and executed quickly. Thus it is essential that manuscripts are accurate when submitted. Authors can track the status of their accepted articles on http://en.sv-jme.eu/.

PUBLICATION FEE:

Authors will be asked to pay a publication fee for each article prior to the article appearing in the journal. However, this fee only needs to be paid after the article has been accepted for publishing. The fee is 380 EUR (for articles with maximum of 6 pages), 470 EUR (for articles with maximum of 10 pages), plus 50 EUR for each additional page. The additional cost for a color page is 90.00 EUR (only for a journal hard copy; optional upon author's request). These fees do not include tax.

Strojniški vestnik -Journal of Mechanical Engineering
Aškerčeva 6, 1000 Ljubljana, Slovenia, e-mail: info@sv-jme.eu

9 770039 248001
ISSN 0039-2480

http://www.sv-jme.eu

Contents

Papers